Sustainable Polymer & Energy

SCIEPublish

Review

Highly Efficient Nanocomposites of Silica/Polyacrylamide Hybrids with Silver Nanoparticles for Various Modern Nanotechnologies

Tatyana Zheltonozhskaya [1,*], Nataliya Permyakova [1], Valery Klepko [1], Dmitro Klymchuk [2], Olga Demchenko [3], Tetiana Kondratiuk [4], Tetiana Beregova [4], Olha Kravchenko [5], Larysa Shevchenko [5], Bogdan Melnik [6], Svitlana Zahorodnia [7] and Olga Akopova [1,8]

[1] Institute of Macromolecular Chemistry, NAS of Ukraine, 48 Kharkivske Shosse, 02160 Kyiv, Ukraine; permyakova@ukr.net (N.P.); klepko_vv@ukr.net (V.K.); ov_akopova@ukr.net (O.A.)
[2] M.G. Kholodny Institute of Botany, NAS of Ukraine, 2 Tereshchenkivska Str., 01601 Kyiv, Ukraine; microscopy.botany@gmail.com (D.K.)
[3] Faculty of Chemistry, Taras Shevchenko National University of Kyiv, 64 Volodymirska Str., 01033 Kyiv, Ukraine; odemch@ukr.net (O.D.)
[4] Department of Biochemistry, Institute of Biology and Medicine, Taras Shevchenko National University of Kyiv, 2 Hlushkova Avenue, 03127 Kyiv, Ukraine; takbiofak@ukr.net (T.K.); tetyana.beregova@knu.ua (T.B.)
[5] Department of Animal and Food Hygiene, National University of Life and Environmental Sciences of Ukraine, 17 Heroyiv Oborony Str., 03041 Kyiv, Ukraine; olha_kravchenko@nubip.edu.ua (O.K.); shevchenko_laris@ukr.net (L.S.)
[6] Scientific-Research Center of "Kernel", 3 Taras Shevchenko Lane, 01001 Kyiv, Ukraine; bsmelnik@ukr.net (B.M.)
[7] D.K. Zabolotny Institute of Microbiology and Virology, NAS of Ukraine, 154 Acad. Zabolotny Str., 03143 Kyiv, Ukraine; svetazagorodnya@ukr.net (S.Z.)
[8] Bogomoletz Institute of Physiology, NAS of Ukraine, 4 Bogomoletz Str., 01601 Kiev, Ukraine

* Corresponding author. E-mail: zheltonozhskaya@ukr.net (T.Z.)

Received: 16 December 2025; Revised: 5 February 2026; Accepted: 12 June 2026; Available online: 24 July 2026

ABSTRACT: This paper presents a review of studies devoted to the synthesis, characterization, structure, properties, and functionality of grafted silica/polyacrylamide "core-corona" hybrids as effective nanoreactors and silver nanoparticle (AgNP) carriers for modern nanotechnologies. The evidence and features of direct low-temperature radical polymerization of acrylamide from the unmodified surface of SiO_2 nanoparticles are considered in the context of the manifestation of dynamic matrix effects. A simple and reliable method for determining the number and length of grafted PAAm chains is indicated. Using a number of hybrid samples, the effect of these parameters on the particle size, surface charge, height, and permeability of the PAAm "corona" is demonstrated. A two-level fractal structure of hybrids in the bulk state and two morphological forms of their particles in aqueous solutions are established. Based on the proposed approach, the kinetics, mechanism of *in situ* synthesis, and the yield of AgNPs in hybrid solutions are characterized depending on the concentration of reagents and the "corona" structure. Considerable attention is paid to the possible application of AgNP/hybrid nanocomposites in promising nanotechnologies: in the production of biocidal hygienic materials and textiles, in wound healing, agriculture, fish farming and poultry farming, as well as anti-cancer agents.

© 2026 The authors. This is an open access article under the Creative Commons Attribution 4.0 International License (https://creativecommons.org/licenses/by/4.0/).

Keywords: Silica/polyacrylamide hybrid carriers; Silver nanoparticles; Nanocomposites; Structure; Stability; Biocidal and anticancer properties; Nanotechnologies

1. Introduction

The unique antimicrobial and disinfectant properties of silver have been known for many centuries [1]. However, only in recent years has the use of the biocidal properties of silver in the form of ions or especially nanoparticles (AgNPs) received fantastic development [2–5]. Today's consumer products containing AgNPs include medical devices and cosmetics, electronics, building materials and textiles, food packaging materials and food additives, and finally, home appliances, water disinfectants, and room sprays. This line can be complemented by various modern nanotechnologies that involve AgNPs in biomedicine [2,6]. It is therefore not surprising that AgNPs are the most widely used nanoparticles in consumer applications, accounting for approximately 24% of commercial products [5]. In fact, antimicrobial properties have become the basis for most applications of AgNPs.

Silver ions exhibit high biocidal activity against more than 650 bacteria, viruses, and fungi [7]. The biocidal properties of Ag^+ ions are determined by their strong complexation with thiol, amine, and phosphate residues of enzymes and proteins in the membranes and cytoplasm of microbial cells. This disrupts protein structure, enzymatic activity, and lipid-protein interactions in the microbial cell membrane,leadings to deterioration of cellular metabolis and, DNA replication, slowing of enzymatic function, and decreased cell viability [8,9]. In cells, silver ions can generate reactive oxygen species (ROS), causing oxidative stress that impairs the chemical structure and function of lipids, proteins, and DNA [10].

The development of a bottom-up methodology for the synthesis of metal nanoparticles in solution [11,12] based on the original research of M.K. Lee (1889) and J. Turkevich (1951) opened a new era in the use of the antimicrobial properties of silver and stimulated the creation of numerous composite materials with their participation [13–15]. The biocidal action of AgNPs is not limited to the release of Ag^+ ions. Small AgNPs are capable of attaching themselves to cell membranes, causing an increase in their permeability and leading to the death of microorganisms [16,17]. Due to this, they effectively act against numerous pathogens, including gram-positive and gram-negative bacteria, viruses, and fungi [2,18,19]. The properties of silver nanoparticles, such as size, shape, surface charge, and stabilizing coating ("corona"), have a significant impact on their antimicrobial activity. In particular, the destructive effect of AgNPs increased significantly with decreasing nanoparticle size [20,21]. It was also higher for sharp triangular nanoparticles compared to smoothed spherical ones [2,22] and in the case of positively charged particles [23]. In contrast to the similar mechanism of destructive action of AgNPs and Ag^+ ions, these antimicrobial agents differed in the effective concentration required to exhibit a bactericidal effect. Thus, for nanoparticles, this concentration, as a rule, corresponds to the nanomolar level, whereas for ions it increases to the micromolar level [8].

Important advantages of AgNPs as biocidal agents are lower toxicity to the human body [8] and lower resistance of microbial cells to them compared to silver ions [24]. The toxicity of AgNPs to human cells has been shown to depend on many factors: cell type, size and dose of nanoparticles, nature and size of the particle "corona", and temperature [25,26]. Therefore, today all these aspects are actively studied and taken into account when developing new nanotechnologies that use silver nanoparticles.

A significant range of biocidal preparations for household, medical, and industrial purposes is based on organic substances that are toxic to humans and the environment due to various allergic reactions, side effects, and resistance [27–29]. The surface of the body and wounds of various natures are a breeding ground for numerous bacteria, in particular gram-positive *Staphylococcus* spp. and gram-negative *Pseudomonas aeruginosa*. They can also be additionally infected with yeasts, filamentous fungi, and microbial associations [30]. Pathogens causing hospital infections exhibit significant virulence and

resistance to antibacterial drugs. This is why new generation biocidal agents such as metal nanoparticles with broad antimicrobial activity [31–33], lower bacterial resistance [24], and higher tolerance to human cells [8] have been required. They can be used as active disinfectant components of various hygienic materials, bandages, and plasters.

Due to the broad antimicrobial activity of AgNPs and their high adaptability to various biological systems, they have been actively tested in animal husbandry [34–38], particularly in poultry farming [36,38–41]. The aim of these studies was to replace organic antibiotics used in this area, which have been banned in the European Union since 2006. This was associated with the emergence of bacterial strains that were resistant to one or more antibiotics. Resistant bacteria cause great economic losses to livestock and poultry farming [36]. In addition, they can accumulate in animal products and pose a danger to humans. Therefore, the use of AgNPs instead of antibiotics can solve the problem of bacterial resistance [36]. There are numerous studies aimed at the application of AgNPs in poultry farming. They analyze the effect of AgNP administration on the development of broiler chickens [39–48], chicken embryos [39,49–51], and the condition of laying hens [52,53] and quails [54–56].

A promising application of the antimicrobial properties of AgNPs is aquaculture, primarily fish farming [57–59]. Bacterial diseases of fish are considered one of the most serious problems in the fishing industry, as their outbreaks lead to high losses for fish and the economy [57,60]. Bacterial diseases on fish farms are usually treated with antibiotics. However, antibiotic therapy may be accompanied by such undesirable consequences as overdose, ineffective metabolism of drugs, return of their unused parts into the environment, and especially resistance of microorganisms to the antibiotics used. Many aquatic bacteria have developed the ability to adapt and overcome the effects of antibiotics in the environment. Therefore, the idea of using new methods to combat these bacteria in the form of silver nanoparticles has generated great interest. Although AgNPs can be used in a variety of aquaculture applications, three main areas where their application has been beneficial have been identified: nutrition, filters to improve aquatic culture habitat, wastewater, and infectious disease control [59].

In recent years, metal nanoparticles, including AgNPs, have been used in the practice of growing agricultural plants to stimulate their growth and combat diseases [61,62]. Biogenic metal ions in small doses can improve plant growth and development [63]. As a result, attempts have emerged to use aqueous dispersions of stabilized metal nanoparticles instead of metal salts or chelates to treat seeds or leaves of growing plants [64,65]. MeNPs have lower toxicity and demonstrate complex action, namely, as small particles that interact with plant cells and components, as sources of metal ions with controlled release, and as biocidal agents that protect plants and soil from pathogenic bacteria, viruses, and fungi. The effects of AgNPs on crop plants such as rice, corn, beans, pumpkin, spring wheat, pea, and radish have been described in [65] as well as in [62] under real atmospheric conditions. They found significant effects of AgNPs on plant physiology, morphology, biochemistry, and yield, which were determined by the nature of the plants, the concentration, size, and properties of the nanoparticles, and the method of their introduction: by treating plant seeds or leaves or through the soil [65].

Cancer is one of the leading causes of death, and the risk of cancer is gradually increasing worldwide [66]. Growing multidrug resistance of tumor cells, serious side effects of chemotherapy and radiotherapy, as well as the slow development and high cost of modern therapeutic strategies, aggravate the situation. This requires the development of new promising approaches to the treatment of malignant tumors, one of which is silver-based nanomedicine. Due to their physicochemical properties and cost-effective synthesis, silver-based nanosystems are at the forefront of nanomedicine, especially anti-cancer research [66–68]. Over the past decade, the number of published papers devoted to the use of AgNPs has increased dramatically, and this trend continues in oncologic medicine [68]. The anticancer efficacy of AgNPs largely depends on the ability of Ag^+ ions to stimulate the production of free radicals [69–72], which can destroy key cell membrane channels and cellular metabolic enzymes, damage DNA, and affect mitochondria,

ultimately leading to cell death. By acting on mitochondria and causing increased production of reactive oxygen species (ROS) and nucleic acids (RAN), AgNPs are able to induce various cell death pathways (apoptosis, necrosis, and autophagy) [73–76]. In addition to non-specific mechanisms, several targets of nanosilver action in cancer cells have been identified. Thus, AgNPs may influence the immune system and the production of proinflammatory cytokines such as TNF-α and interleukins, leading to apoptosis [71,72]. AgNPs can affect the antioxidant system (SOD, CAT, GPX, Nrf2 pathway) and decrease glutathione levels [77,78], affect glycolytic pathways critical for cancer cells [66], increase the level of pro-apoptotic proteins (caspases 3, 7, 9, and Bax), and decrease the level of anti-apoptotic proteins (Bcl-2 [79,80]).

Currently, there are many modern methods for obtaining AgNPs, including physical, chemical, and plant or bacterial methods, which have been described and discussed in a number of publications [2–4,6,81,82]. Among them, *in situ* chemical reduction of silver salts or oxides in aqueous solutions of various polymer and hybrid matrices under mild conditions remains one of the most popular methods, since it allows the stabilization of nanoparticles with a "corona" of controlled nature, structure, and size [83–87]. In this way, practically important properties of AgNPs can be easily controlled in the desired direction. For the synthesis and stabilization of AgNPs in aqueous solutions by the indicated method, various synthetic homopolymers were primarily used: poly(ethylene glycol), poly(vinylpyrrolidone), poly(vinyl alcohol), polyacrylamide, poly(acrylic acid)/polyacrylate, poly(vinyltriazole), poly(N-isopropylacrylamide), and others [88–93]. In addition, various hydrophilic hybrid block and graft copolymers [94–96], dendrimers [97,98], block ionomer complexes [99], and natural hydrophilic polymers, in particular cellulose, chitosan, dextran, starch, gelatin, gum arabic, sodium alginate, *etc*. [100–104] have also been used as nanoreactors and matrices. The reduction of silver ions in their solutions occurred either due to active polymer groups, or photochemical, microwave and γ-irradiation processes, or by using various reducing agents, in particular, sodium borohydride, formaldehyde, hydrazine, hydroxylamine, sodium citrate, ascorbic acid, glucose, ethylene glycol, dimethyl sulfoxide and others.

There is a general mechanism for the reduction of Ag-salt in solutions of hydrophilic polymers of both synthetic and natural origin, which was discussed in detail in our previous study [105]. In short, it consists of preliminary interaction of Ag^+ ions with hydroxyl, carbonyl, amide, carboxylate, ester, amine or other active polymer groups to form weaker or stronger complexes. This complexation is a competitive reaction for the subsequent reduction of Ag^+ ions by the reducing agent. This means that by using a polymer matrix with different strengths of active groups, it is possible to regulate to a greater or lesser extent the rate of reduction of Ag^+ ions. When the reduction rate is lower, the possibilities for controlling the nucleation and growth of nanoclusters and nanoparticles to obtain AgNPs of the required size and shape are significantly expanded [90]. An important factor is the length of the polymer chains. Thus, the stability of Ag^+/polymer complexes to reduction and growing AgNPs to aggregation increases with the elongation of polymer chains [89]. This factor becomes especially important when the rate of the reduction reaction is high. The strength of the reducing agent, which depends on its RedOx potential, also influences the rate of reduction, as well as the size, morphology, and especially the yield of nanoparticles [105].

The use of various heteropolymers, such as micelle-forming block and graft copolymers, as hydrophilic matrices has opened a new page in the *in situ* synthesis of AgNPs [94–96,105]. Due to the micellar structures, it was possible to create a high local concentration of active polymer groups in the "coronas" for effective complex formation with metal ions. The size of the reaction "cavities" in the micellar matrices for growing AgNPs could also be easily varied. These factors make it possible to regulate the reduction process and the parameters of the resulting AgNPs [105]. As matrices for the *in situ* synthesis of AgNPs, our research group used double hydrophilic diblock and triblock copolymers based on asymmetric chemically complementary (methoxy)poly(ethylene oxide)/polyacrylamide blocks: MOPEO-*b*-PAAm (M_n = 34.8 kDa) and PAAm-*b*-PEO-*b*-PAAm (M_n = 240.0 kDa) [106]. They formed a special type of micelles in aqueous solutions with a "core" of interacting (MO)PEO and PAAm segments and demonstrated a strong stabilizing

effect for the resulting AgNPs upon rapid reduction of Ag^+ ions with $NaBH_4$. The small average size of the obtained spherical nanoparticles (d_{av} = 5 and 6 nm in the case of diblock and triblock copolymers, respectively) and the two-level fractal structure of the final composites in the bulk state were established.

In contrast to polymolecular micelles of block copolymers and interpolymer complexes, which in principle could be destroyed during the synthesis of AgNPs *in situ*, micelle-like structures of graft copolymers (monomolecular micelles) turned out to be more stable in solution from this point of view [107]. In this context, double hydrophilic graft copolymers containing interacting polyvinyl alcohol backbones and grafted polyacrylamide chains (PVA-*g*-PAAm) were of particular interest. Due to the presence of an additional system of hydrogen bonds between the main and grafted chains, the possibilities of changing the sizes of reaction "cavities" in the matrices increased significantly. Thus, the use of a copolymer sample with M_{vPVA} = 90 kDa, M_{vPAAm} = 147 kDa, and the number of grafts N = 10 as a matrix in the sodium borohydride reduction of Ag-salt at low temperatures led to the rapid formation of very small (d_{av} = 3.5 nm) spherical crystalline AgNPs in the grafted layer [107]. The resulting nanocomposite was stable in solution over time and had a two-level fractal structure in the bulk state.

Later, the idea emerged to use grafted silica/polyacrylamide hybrids (SPH) with a SiO_2 "core" and a PAAm "corona" as matrices for the synthesis of AgNPs [108]. It was based on: (i) the combination of the high adsorption capacity of the silica surface and the strong binding activity of PAAm chains with respect to metal ions, colloidal particles and organic substances, (ii) the non-toxicity, biocompatibility and biodegradability of SiO_2 and PAAm [109,110], and (iii) the thermodynamic affinity (chemical complementarity) of these components, which was realized through the formation of hydrogen bonds between the amide and silanol groups [111]. We considered the presence of additional non-covalent interactions between PAAm and SiO_2 as an additional factor regulating the size of the cavity in the polymer "corona" where AgNPs grew. A significant positive synergistic effect from the combined properties of these components was observed in our previous studies [112,113], in which SPHs demonstrated high efficiency as flocculants in drinking water production processes at waterworks. The successful application of SiO_2 particles and PAAm chains individually as matrices for *in situ* synthesis of AgNPs has also been well documented [90,114,115].

The literature of the last two decades contains many studies devoted to polymer/inorganic hybrids containing silica nanoparticles and various hydrophilic polymers, including PAAm[85,116–125]. They discussed the classification of different types of hybrid materials, methods of production, properties, and areas of their possible application. At the same time, studies testing SPHs as matrices for *in situ* synthesis of AgNPs in solutions were virtually absent. We found only a few related studies that used SiO_2 hybrids with other hydrophilic polymers such as polyvinylpyrrolidone [126], sodium polyacrylate [127], and hydroxypropyl cellulose [128] for this purpose. These studies were devoted to obtaining corresponding hybrid materials (films) of silica/polymer with embedded silver nanoparticles. In contrast, the main goal of our research was to create highly dispersed and solution-stable hybrid nanoparticles filled with small AgNPs to solve many problems of modern nanobiomedicine.

The subject of this review article is a summary of all our studies devoted to the creation and use of SPH as interesting and promising nanomaterials. The developed simple methods for the synthesis and characterization of SPH, as well as the production of highly dispersed and stable in time and light nanocomposites with small AgNPs, are considered. Finally, the areas of their possible successful application in the production of hygienic materials and textiles, in wound healing, agriculture, fish farming and poultry farming, as well as effective carriers for the delivery of AgNPs as anticancer agents are revealed.

2. Features of "Grafting from" Polymerization of Acrylamide on the Surface of Silica Particles

The development of increasingly advanced methods for creating polymer/inorganic hybrids has received considerable attention in the scientific literature [85,116,117,119,123,124]. The processes of

"grafting from" and "grafting to" are currently the key methods for covalent grafting of polymers to inorganic nanoparticles. The first of these involves the polymerization of monomers from a functionalized surface, while the second involves the chemical reaction of functionalized polymers with the surface of nanoparticles that is modified with the necessary chemical groups. The main advantage of the "grafting-to" method is its simplicity and the use of well-characterized polymer chains. At the same time, this method does not allow achieving a large number (density) of grafts, since the reaction process is limited by the rate of diffusion of polymer chains with functionalized ends through the brush layer. In contrast, the "grafting from" method allows for the production of dense polymer layers, since the active centers on the surface of the nanoparticles and the growing polymer chains are easily accessible to the monomer molecules during the polymerization process. A wide range of polymerization mechanisms has been used to create various grafted polymer layers on inorganic surfaces: free radical polymerization and controlled radical methods such as nitroxide-mediated polymerization, atom transfer radical polymerization, and reversible addition-fragmentation chain transfer polymerization (NMRP, ATRP, and RAFT), living anionic and cationic polymerization, ring-opening polymerization, and hyperbranching [119,129,130].

There are many studies devoted to the grafting of various polymer chains onto SiO_2 nanoparticles using most of the mentioned polymerization mechanisms [116–119,123,129,131]. Preliminary chemical modification of the silica surface to create the necessary functional groups has long been considered as the main method for graft polymerization of monomers from the resulting active centers [117,118]. At the same time, radical polymerization of monomers on the surface of solid particles differs from liquid-phase polymerization by a number of features that complicate the kinetic control of the process and do not allow obtaining polymer/inorganic hybrids with given parameters of the grafted polymer layer, such as the density and length of polymer chains. In addition, it is necessary to account for the significant influence of surface chemistry and porosity on adsorption interactions with monomers and oligomers. Therefore, the mechanism of these processes remains little studied. One of the reasons for this is the different structure and texture of silica samples, the presence of uncontrolled impurities in them, which change the acidic properties of the surface. In addition, the content of water and surface groups was often not taken into account or controlled.

Based on the preliminary successful experience of radical block and graft copolymerization of polyacrylamide (PAAm) with polyethylene glycol and polyvinyl alcohol [132,133], we have developed a similar version of direct grafting of PAAm from the surface of a monodisperse silica sol using a Ce^{IV} (cerium ammonium nitrate) complex salt as a Red/Ox initiator [134]. In contrast to the similar graft polymerization of PAAm from SiO_2 nanoparticles, first carried out in [135], the silica nanoparticles were not pre-modified to obtain surface –C-OH groups. Thus, graft polymerization was initiated by the reaction of the Ce^{IV} salt with the ≡Si–OH groups containing a mobile proton. This process can be described by the following chemical reactions (Figure 1).

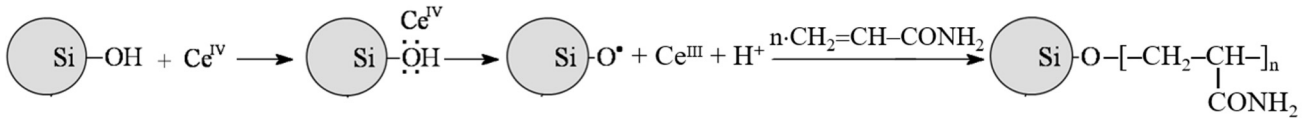

Figure 1. Reaction of graft polymerization of PAAm from the surface of silica sol.

The kinetics of this process were studied depending on two ratios $[Ce^{IV}]/[SiO_2]$ and $[Ce^{IV}]/[AAm]$, which determine the number and length of grafted chains, as well as in comparison with the homopolymerization of AAm initiated by two Red/Ox pairs: Ce^{IV}/EtOH and Ce^{IV}/AAm and carried out under the same experimental conditions [136]. The main focus of these experiments was on possible kinetic matrix effects that often accompany radical template polymerization [137], taking into account the high affinity of PAAm chains for the SiO_2 surface due to the formation of hydrogen bonds between the amide and surface silanol groups [111].

Monodisperse silica sol was prepared by mixing Aerosil with S = 1.85 × 10^5 $m^2 \cdot kg^{-1}$ in deionized water with a concentration of 10 $kg \cdot m^{-3}$ for 24 h and subsequent double centrifugation of the dispersion for 30 min at 6000 rpm. Thus, a stable concentrated silica sol was obtained. Its particle size (7.7 nm) was determined by static light scattering [105]. Syntheses of polymer/inorganic hybrids were carried out in an inert (argon) atmosphere at room temperature, adding the AAm monomer to the reaction mixture only after complexation of Ce^{IV} ions with the ≡Si–OH groups of the nanoparticle surface. The concentration of SiO_2 sol was constant (2.7 $kg \cdot m^{-3}$). The obtained kinetic curves of AAm homopolymerization and its graft polymerization from the SiO_2 surface, measured by the dilatometry method, are presented in Figure 2, and the found kinetic parameters are collected in Table 1.

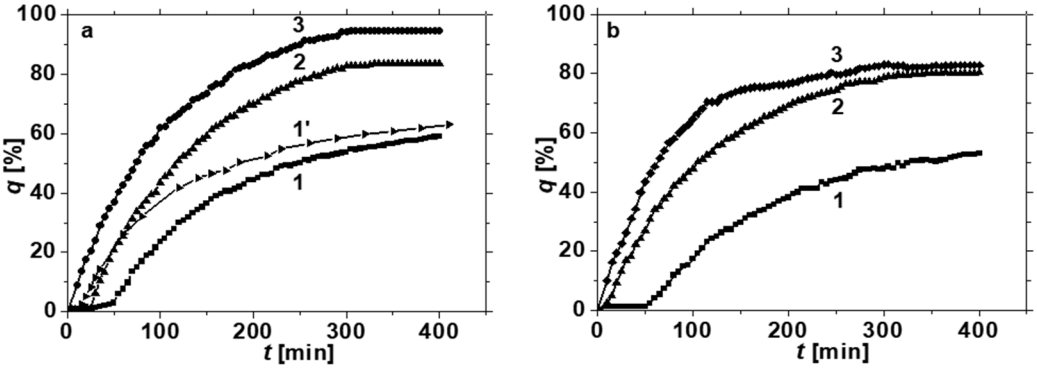

Figure 2. Dependence of monomer conversion on time during (**a**) polymerization of AAm and (**b**) graft polymerization of AAm from the surface of the SiO_2 sol at ratios: $[Ce^{IV}]/[AAm] = 1 \times 10^{-3}$—*1*, *1′*, *2* (**a**,**b**) and 0.5×10^{-3} $mol \cdot mol^{-1}$—*3* (**a**,**b**), as well as $[Ce^{IV}]/[SiO_2]$ = 0.2—*1*, *3* (**b**) and 0.4 $kg \cdot kg^{-1}$—*2* (**b**). Homopolymerization was initiated by Ce^{IV}/AAm—*1*, *2*, *3* (**a**) and Ce^{IV}/EtOH—*1′* (**a**) pairs. *T* = 13 °C.

In the homopolymerization of AAm initiated by the Ce^{IV}/AAm pair (Figure 2a, curves 1–3), an increase in the concentration of Ce^{IV} and AAm or only the monomer (syntheses of PAAm2 and PAAm3) led to a reduction in the induction period, an increase in the initial reaction rate, and monomer conversion in the same time (Table 1). However, the highest process rate was achieved with a simultaneous increase in the concentrations of Ce^{IV} and AAm (synthesis of PAAm2).

Table 1. Kinetic parameters of PAAm grafting from SiO_2 surface and homopolymerization.

Sample	α_w [1]	$\beta_m \cdot 10^3$ [2]	τ_0 [3] [min]	$v_{20} \cdot 10^4$ [4] [mol·dm^{-3}·s^{-1}]	$v_{50} \cdot 10^4$ [4] [mol·dm^{-3}·s^{-1}]	q [5] [%]
SPH1	0.2	1	50	0.56	0.10	53
PAAm1	-	1	50	0.80	0.13	59
PAAm1′	-	1	15	0.82	0.17	62
SPH2	0.4	1	9	1.73	0.93	80
PAAm2	-	1	22	2.77	1.70	95
SPH3	0.2	0.5	0	2.90	1.50	82
PAAm3	-	0.5	0	2.29	1.04	84

[1] Weight ratio $[Ce^{4+}]/[SiO_2]$. [2] Molar ratio $[Ce^{4+}]/[AAm]$. [3] Induction period. [4] The polymerization rate of PAAm at monomer conversion q = 20 and 50 wt %. [5] Monomer conversion 400 min after the start of polymerization.

Ce^{IV} compounds do not oxidize water molecules in the presence of vinyl monomers. They interact with monomers, forming free radicals on carbon atoms. Homopolymerization of vinyl monomers initiated by Ce^{IV} salts occurs with an induction period. The duration of this period depends, first, on the rate of formation/destruction of the CeIV/monomer complex, whose existence has been confirmed by different methods [138,139]. The use of the initiating pair Ce^{IV}/EtOH in one of the syntheses (PAAm1) had little effect on the rate of the process and the conversion q, but significantly, by more than 3 times, reduced the

induction period (Figure 2a, curves 1, 1′; Table 1). Therefore, the stability of Ce^{IV} complexes with hydroxyl groups was lower.

Comparison of the kinetic parameters of graft and homopolymerization of AAm in Table 1 showed the presence of negative dynamic matrix effects in the processes of formation of SPH1 and SPH2, and an insignificant difference in the kinetic parameters of graft and homopolymerization of AAm in the production of SPH3. The significant slowdown in the growth of grafted PAAm chains on the SiO_2 surface compared to the polymerization of AAm in the liquid phase is due to the strong interaction of the polar monomer molecules and the growing "daughter" PAAm chains with the silica surface. As a result, the monomer molecules lost their diffusion mobility, and the resulting dense polymer layer on the SiO_2 surface hindered the transport of reagents into the reaction zone. Therefore, in order to enter into a chain reaction of growth, the AAm molecules, which strongly interacted with the SiO_2 surface, had to overcome an additional activation barrier, namely, weaken or break their bonds with the surface. In this context, the PAAm grafting reaction to obtain hybrid SPH3 was of particular interest, since its parameters were close to the parameters of AAm homopolymerization in solution (Table 1). The absence of a dynamic matrix effect in this case can be explained not only by an increase in the thickness of the monomer adsorption layer with an increase in its concentration. A significant role was also played by a sharp increase in the growth rate of the "daughter" chains, so that it obviously exceeded the rate of interaction of the growing chains with the surface. In this case, the PAAm chains apparently grew from the SiO_2 surface into the solution without matrix control.

Thus, the processes of "grafting from" polymerization involving a hydrophilic, chemically complementary polymer and nanoparticles similar to PAAm and SiO2, carried out in an aqueous medium and accompanied by interactions between monomers and growing polymer chains and the nanoparticle surface, can exhibit matrix character (Figure 3). This can be expressed in a change in the rate of such processes compared to the homopolymerization of the corresponding monomers in the same environment and experimental conditions. The magnitude of the dynamic matrix effect will depend on the relative concentration of the monomer. Thus, in the process of grafting PAAm from the SiO_2 surface, an interesting effect of the disappearance of the dynamic matrix effect with a significant increase in the monomer concentration (with an increase in the growth rate of the "daughter" chains) was established.

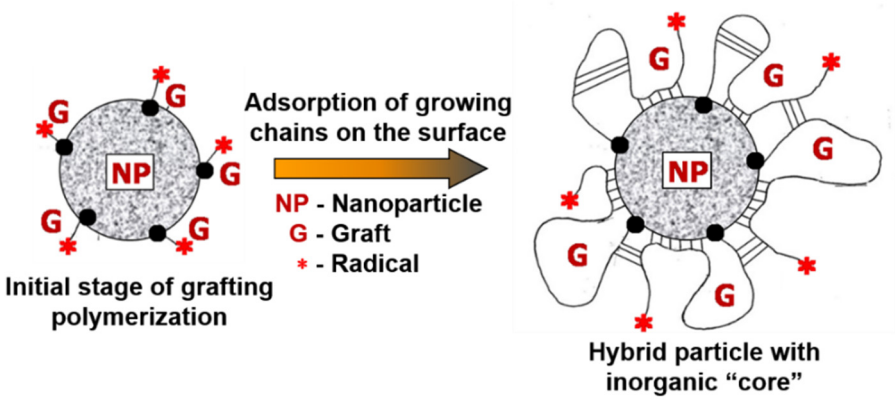

Figure 3. General scheme of matrix graft polymerization from the surface of a chemically complementary inorganic nanoparticle.

3. Molecular Structure of Hybrids: Confirmation and Characterization

The next important tasks after the synthesis of SPH were: (i) confirmation of the fact of grafting and (ii) development of a methodology for detailed characterization of the molecular and structural parameters of hybrids. To prove the fact of direct grafting of PAAm from the SiO_2 surface without its preliminary modification, a homopolymerization reaction of AAm with a special initiator was carried out [136]. In this

case, the Red/Ox system was used as an initiator, including a complex salt of Ce^{IV} and a monofunctional organosilicon compound, trimethylhydroxysilane, which was formed as a result of the hydrolysis of 1,1,1,3,3,3-hexamethyldisilazane. As a result, a homopolymer of PAAm with M_v = 832 kDa and terminal groups $(CH_3)_3$-Si-O-, determined by elemental analysis for silicon, was obtained [136].

The second problem was more complex. The degree of grafting is the most widely used parameter to characterize the polymer content of polymer or polymer/inorganic hybrids, but not their detailed structure [140,141]. This parameter means the increase in weight of the original component in the form of macromolecules or nanoparticles to which another polymer component is grafted. Determination of the degree of grafting is used in cases where experimental determination of the number and length of grafted chains is difficult, since it often requires destruction of the original polymer or particle [142]. We addressed this problem using our experience in characterizing polyvinyl alcohol/polyacrylamide graft copolymers [132] and the known property of silica nanoparticles to dissolve in water at pH > 11 [110]. Thus, the chemical structure and molecular parameters of the synthesized SPHs were characterized by static light scattering (SLS), elemental analysis (EA), dynamic thermogravimetric analysis (DTGA), and viscometry [105]. The SLS method was used to determine the average radius of silica sol nanoparticles (r_{SiO2}). Using the EA data for C and N, the mass fraction of PAAm (w_{PAAm}) in SPH was determined. The weight fraction of water (w_{H2O}) was determined using DTGA data. The weight fraction of SiO_2 (w_{SiO2}) was calculated as the difference: $w_{SiO2} = 1 - w_{PAAm} - w_{H2O}$. To destroy silica nanoparticles, an aqueous solution of SPH was kept for one week at room temperature and pH = 11.5. Thus, complete destruction of silica nanoparticles occurred [110], and only minor hydrolysis of PAAm chains took place [143]. The reaction mixture was reprecipitated with acetone, centrifuged, and redissolved in water. The degradation products were then completely removed by prolonged dialysis of the solution against deionized water. The viscosity-average molecular weight of PAAm was determined by viscometry, and the number of grafts (N) per SiO_2 nanoparticle was calculated using the ratio (1):

$$N = \frac{4\pi \cdot r_{SiO2}^3 \cdot \rho \cdot w_{PAAm} \cdot N_A}{3 \cdot w_{SiO2} \cdot M_{vPAAm}} \quad (1)$$

In this formula, ρ = 2.1 g·cm^{-3} is the density of silica, product $4/3(\pi \cdot r_{SiO2}^3 \cdot \rho)$ is the weight of a silica nanoparticle, N_A is Avogadro's number, M_{vPAAm} is the viscosity-average molecular weight of PAAm.

The following four synthesized SPH samples were characterized using the above scheme (Table 2). They were used in our subsequent physicochemical and biological studies. Samples SPH4-SPH7 contained a relatively small weight fraction of SiO_2 nanoparticles: from 7.2 to 14.5 wt %. However, their presence in hybrids has been reliably confirmed by Fourier transform infrared spectroscopy (FTIR) and small-angle X-ray scattering (SAXS) methods.

An example of the FTIR spectrum for one of the SPH samples is shown in Figure 4a–c in comparison with that of pure PAAm (Figure 4d,e), which was described in detail earlier [144]. The positions of the individual bands together with their interpretation are collected in Table 3. The appearance in the hybrid spectrum of the vibration bands of Amide I_b, Amide II_b, Amide III (Figure 4a,b), and $\nu_{(N-H)}$ (Figure 4c), corresponding to hydrogen-bonded amide groups in the structures of *trans*- and *cis-trans*-multimers [111,144], indicated the presence of PAAm in the hybrid sample. The presence of SiO_2 as a minor component in this hybrid was clearly confirmed by the appearance in the spectrum of an intense band of ν_{Si-O-C} and $\nu_{Si-O-Si}$ vibrations at 1117 cm^{-1} (Figure 4a, Table 3) [145].

Table 2. Main characteristics of the synthesized hybrid samples.

Hybrid	w_{PAAm} [1] [wt %]	w_{H2O} [2] [wt %]	w_{SiO2} [3] [wt %]	r_{avSiO2} [4] [nm]	M_{vPAAm} [5] [kDa]	N [6]
SPH4	85.2	5.3	9.5	7.7	1588	14
SPH5	85.5	11.0	9.5	7.7	822	72
SPH6	72.9	12.6	14.5	7.7	1513	8
SPH7	79.0	13.8	7.2	7.7	5084	5

[1] Weight fraction of PAAm in the sample calculated from elemental analysis data. [2] Total water content in the sample determined from TG curves. [3] Weight fraction of SiO_2 in the hybrid: $w_{SiO2} = 1 - w_{PAAm} - w_{H2O}$. [4] Average radius of silica particles determined by static light scattering. [5] Viscosity-average molecular weight of grafted PAAm chains. [6] Average number of grafted PAAm chains per SiO_2 particle.

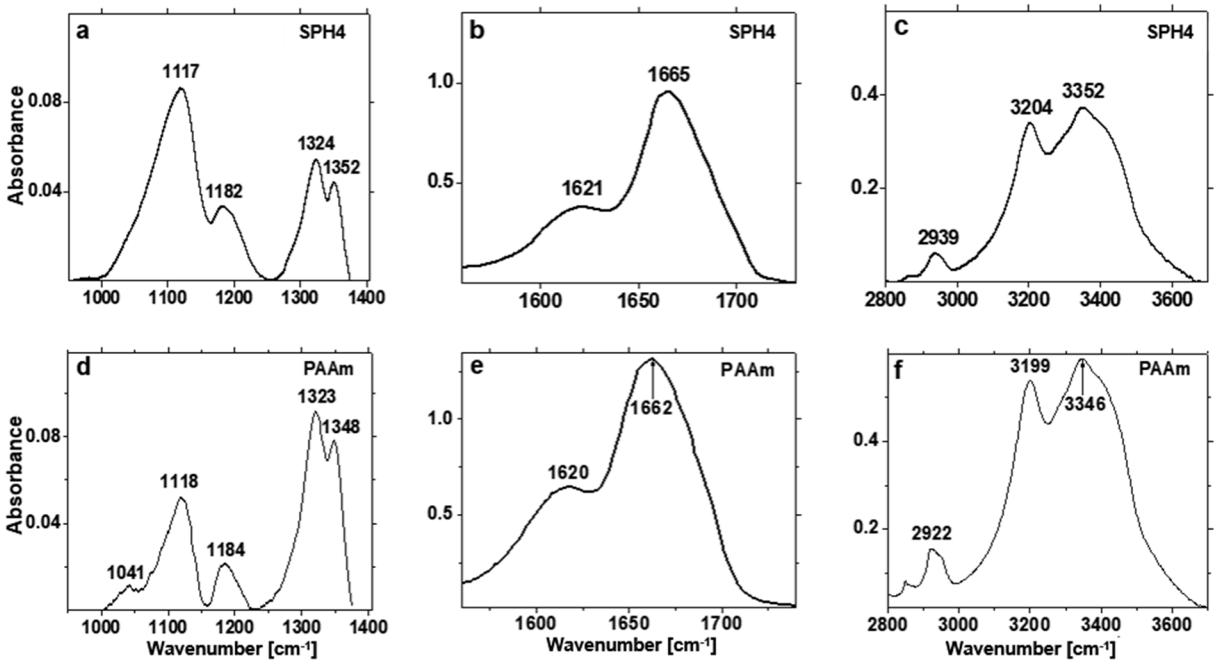

Figure 4. FTIR spectra of thin films of (**a**–**c**) SPH4 and (**d**–**f**) pure PAAm cast on fluorite glasses in the regions of (**a**,**d**) $\delta_{N\text{-}H}$, $\delta_{C\text{-}H}$, $\nu_{Si\text{-}O\text{-}Si}$, $\nu_{Si\text{-}O\text{-}C}$ and Amide III vibrations, (**b**,**e**) Amide I_b and Amide II_b vibrations, and (**c**,**f**) $\nu_{C\text{-}H}$, $\nu_{N\text{-}H}$, $\nu_{O\text{-}H}$ vibrations. T = 25 °C.

Table 3. Vibration bands in the FTIR spectra of polyacrylamide and one of the hybrids.

Hybrid Component	Band Position [cm^{-1}] PAAm	Band Position [cm^{-1}] SPH4	Type of Vibrations [1] (Group or H-Bond Structure)
PAAm	~3400–3450	~3400–3450	$\nu_{(N\text{-}H)f}$
	3346	3352	$\nu_{(N\text{-}H)b}$ (*trans*-multimers)
	3199	3204	$\nu_{(N\text{-}H)b}$ (*cis*-*trans*-multimers)
	2922	2939	$\nu_{(C\text{-}H)as}$ (CH_2)
	2850	2862	$\nu_{(C\text{-}H)s}$ (CH_2)
	1662	1665	Amide I_b ($\nu_{(C=O)}$)
	1620	1621	Amide II_b ($\delta_{(N\text{-}H)trans} + \nu_{(C\text{-}N)}$)
	1348	1352	$\delta_{(C\text{-}H)as}$ (CH_2)
	1323	1324	Amide III ($\nu_{(C\text{-}N)}$)
	1184	1182	$\delta_{(N\text{-}H)ip}$
	1118	1117	$\delta_{(N\text{-}H)oop}$
	1041	-	-
SiO_2	-	1117	$\nu_{(Si\text{-}O\text{-}Si)as}$, $\nu_{(Si\text{-}O\text{-}C)as}$

[1] Designations: *f*—vibrations of free groups, *b*—vibrations of H-bonded groups, *s*—symmetric vibrations, *as*—antisymmetric vibrations, *ip*—in-plane vibrations, *oop*—out-of-plane vibrations.

In addition, under the influence of SiO_2 nanoparticles, changes occurred in the structure of the hydrogen bonds of the amide groups of PAAm. So, in the SPH4 sample, the length of the *cis-trans*- and *trans*-multimers of the amide groups decreased. The observed high-frequency shifts of the Amide I_b band by 3 cm^{-1} and two $\nu_{(N-H)b}$ vibration bands by 5 cm^{-1} and 6 cm^{-1} in the spectrum of SPH4 compared to the spectrum of PAAm confirmed this conclusion (Table 3). We also note the absence in the spectrum of SPH4 of the ν_{O-H} vibration band of free silanol groups at ~3700 cm^{-1} (Figure 4c), which is observed in the spectrum of silica sol [146]. This fact indicates the existence of hydrogen bonds between the grafted PAAm and SiO_2 particles, as discussed earlier [111].

The small-angle X-ray scattering (SAXS) results for the same SPH4 sample obtained in the study [146] and compared with similar data for pure PAAm [111] are shown in Figure 5.

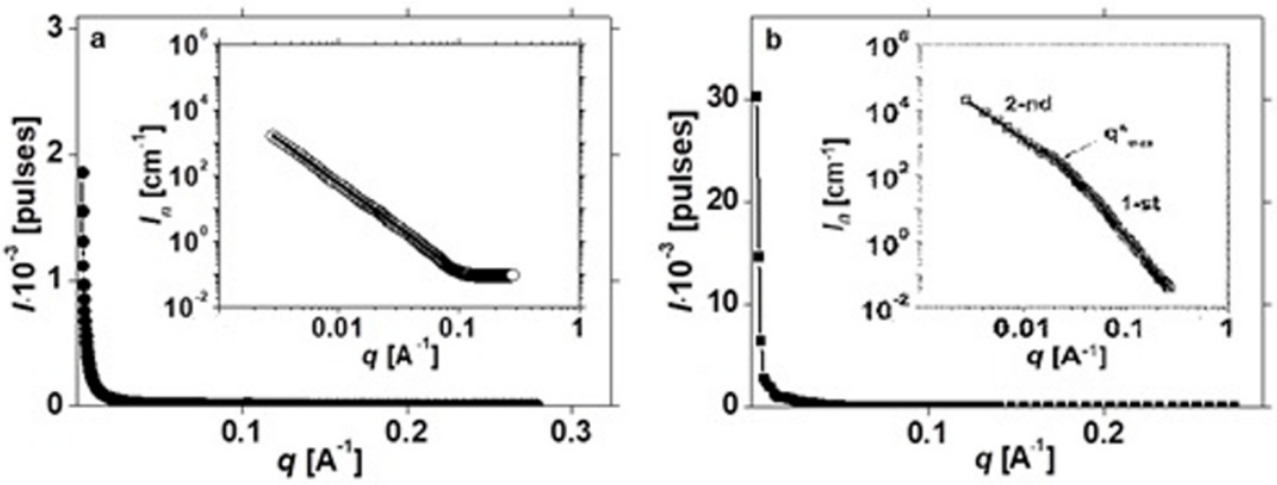

Figure 5. Small-angle X-ray scattering intensity as a function of wave vector q for (**a**) PAAm and (**b**) SPH4. Log-scale SAXS profiles are shown as insets. T= 20 °C. Log-scale SAXS profiles are shown as insets. In the inset of panel (**b**), the breakpoint q^* indicates the crossover between the low-q and high-q structural regimes.

For both samples, a sharp monotonic drop in scattering intensity with increasing wave vector (q) was found, which indicates the absence of any periodicity in the arrangement of individual structural elements of PAAm and SPH4 at the supramolecular level. These profiles were then normalized to the thickness of the samples and the scattering intensity of the standard and were presented in two logarithmic coordinates (two inserts in Figure 5) for their analysis in terms of known concepts of the fractal organization of the polymer structure [146,147]. For pure PAAm, the linear decrease of log I_n from log q with a single slope ratio was maintained in almost the entire studied region of q (Figure 5a). This fact reflected the existence in the SAXS profile of the homopolymer of a single power scattering regime by Porod ($I \approx q^{-Df}$), which corresponded to the scattering pattern in a system where single-level fractal clusters existed [147]. The type of these clusters: mass-fractal or surface-fractal could be determined by analyzing the modulus of the slope ratio $|D_f|$. In addition, their maximum diameter could be estimated by the relatio $d_{max} \sim 2\pi/q^*$, but only in the case when the straight line of the Porod's power scattering regime ended (or was "cut off") at small q by the exponential Gineau scattering regime. The exponential scattering regime by Gineau and the corresponding power regime by Porod (at larger q) characterized one structural level. However, the SAXS profile in Figure 5a for PAAm had no "the cutting border" at small q, so determining d_{max} in this case was impossible.

The found value of D_f for PAAm was <3 (Table 4). This meant that the amorphous structure of this polymer had a porous nature and consisted of mass-fractal clusters with a fractal size of D_f = 2.7 [146]. Individual "building blocks" of such clusters were fragments of polymer chains [146,147]. These clusters appeared due to the high hydrophilicity of this polymer. Indeed, the equilibrium moisture content of the

PAAm film was significant, ~10 wt %. Therefore, even long-term drying of polymers in a vacuum oven and vacuum desiccator did not ensure complete removal of adsorbed water from them.

Table 4. Parameters of individual elements of the fractal structure of PAAm and hybrid.

Value \ Sample	PAAm	SPH4	
		1st Level	2nd Level
D_f	2.7	3.8	2.1
$q^* \cdot 10^{2}$ (1) [A^{-1}]	-	2.7	-
d_{max} (2) [nm]	-	23.3	-
$R_{g(exp)}$ [nm]	-	9.0	-
$R_{g(calc)}$ [nm]	-	8.0	-

(1) "Cutting border" for the power scattering regime. (2) Maximum diameter of hybrid surface-fractal clusters.

In contrast, the SAXS profile for the SPH4 sample in double logarithmic coordinates (insert in Figure 5b) revealed two linear dependences with different slopes, corresponding to two power scattering regimes by Porod. These linear relationships were connected by a curve corresponding to the exponential scattering regime described by Gineau [148]. This SAXS profile shape indicated a two-level fractal organization of the SPH structure [147]. The types of individual elements at each level were determined based on the Df values (Table 4). The remaining two parameters (q^* and d_{max}) could be determined only for the 1st lower level of the SPH4 structure. For the 2nd structural level (at lower q), these parameters could not be found, since the corresponding straight line of Porod scattering in Figure 5b was not limited at the top by the Gineau scattering curve. The value $D_f = 3.8$, determined for the 1st linear part of the SPH4 SAXS profile (Table 4), indicated the existence of surface-fractal clusters with a denser "core" and a fractal size $D_s = 6 - D_f = 2.2$ [147], which constitute the 1st fractal-organized structural level of the polymer/inorganic hybrid. This was direct evidence of the presence of SiO_2 nanoparticles with grafted PAAm chains in the structure of this nanomaterial. It is important to note that the average radius of gyration for these clusters (9.0 nm in Table 4) obtained from the SAXS data correlates with the average radius of the SiO_2 sol nanoparticles found before PAAm grafting (Table 2).

The 2nd, higher level of structural organization of the hybrid is formed by mass-fractal clusters consisting of fragments of PAAm chains. This conclusion was made on the basis of the value $D_f < 3$ determined for this level from Figure 5b (Table 4) [147]. The obtained value $D_f = 2.1$ was in good agreement with $D_f = 2.7$ for mass-fractal clusters of pure PAAm and $D_f = 2.2$–2.4 for those in the structure of triblock copolymers PAAm-*b*-PEO-*b*-PAAm [147].

In the reference study [147], computer modeling of SAXS profiles was also carried out using the method of global unified exponential-power functions developed by Beaucage et al. [148], which was actively used in the study of fractal-organized polymers and composite materials.These authors showed that log I_n versus log q dependences for fractal materials can contain two or more Porod's power scattering regimes. Their approach consisted of separating several structural levels using a number of power scattering regimes, which were limited by the exponential Gineau scattering curves, and considering the contributions of each structural level to the overall scattering function $I(q)$ [148]. Using the Beaucage approach and formula, we modeled the SAXS profile of SPH4, accounting for two levels of its structural organization. The corresponding smooth curve is shown in the inset of Figure 5b. The $R_{g(calc)}$ value for surface-fractal clusters in the SPH4 structure (Table 4) was consistent with that found from the experimental SAXS profile.

Thus, using the described experiments, the fact of grafting of PAAm chains from the surface of SiO_2 nanoparticles without its preliminary modification was completely proven.

4. Morphology, Size, and Surface Charge of Hybrid Particles in Aqueous Solutions

Aqueous solutions of SPH contained two types of structures: individual hybrid particles and their fractal aggregates of different sizes and shapes. This fact was established by TEM in a number of our previous works [105,149]. The corresponding TEM images for one of the first synthesized SPH4 samples are shown in Figure 6.

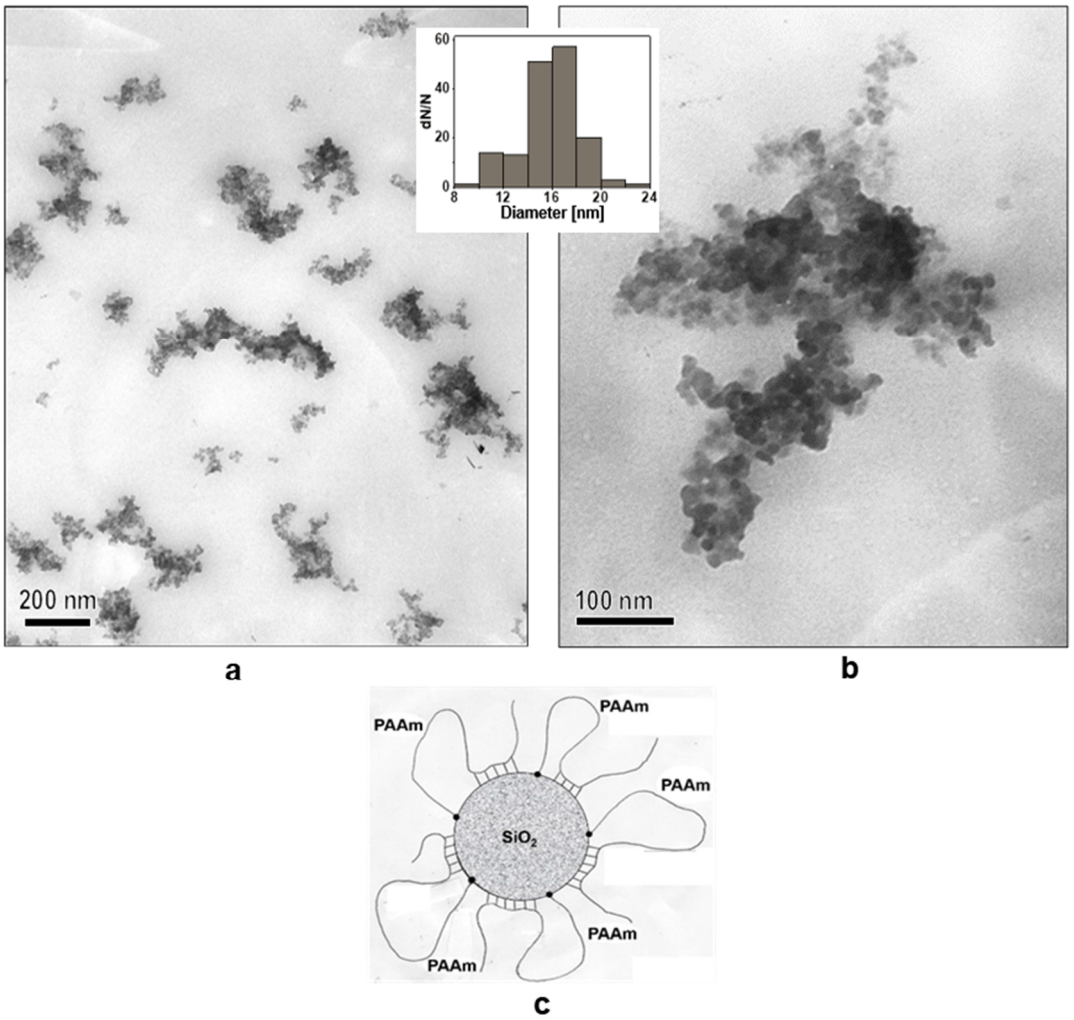

Figure 6. TEM micrographs at (**a**) lower and (**b**) higher magnifications obtained using an aqueous solution of SPH4. (**c**) Structural model of a single hybrid particle. The particle size distribution calculated using ImageJ program is shown in the inset. C_{SPH} = 1.0 kg·m^{-3}, T = 20 °C.

Individual hybrid particles were compact, had a nearly spherical shape, and had a smooth surface, confirming the strong interaction of the grafted PAAm with the SiO_2 surface. This structural feature was reflected in the hybrid model proposed below (Figure 6c). There was also an interaction between the surface layers of the PAAm hybrid particles, leading to the appearance of fractal clusters. Apparently, the driving force of such interaction was the formation of hydrogen bonds between the PAAm segments included in the "coronas" of different hybrid particles [105].

Separate TEM studies were performed for a series of SPH5–SPH7 samples (Figure 7), in which the number of grafted PAAm chains decreased, and their length increased (Table 2). Based on the TEM images, the size distributions and average diameter of individual hybrid particles (d_{avSPH}), as well as the average height (thickness) of their PAAm "corona" (h_{avPAAm}) were determined (Table 5). The size of individual hybrid particles and the thickness of the PAAm "corona" increased when moving from the 5th to the 7th

sample. As a result, in this hybrid series, the thickest polymer "corona" was found in SPH7 particles with the smallest number of PAAm grafts, but their greatest length.

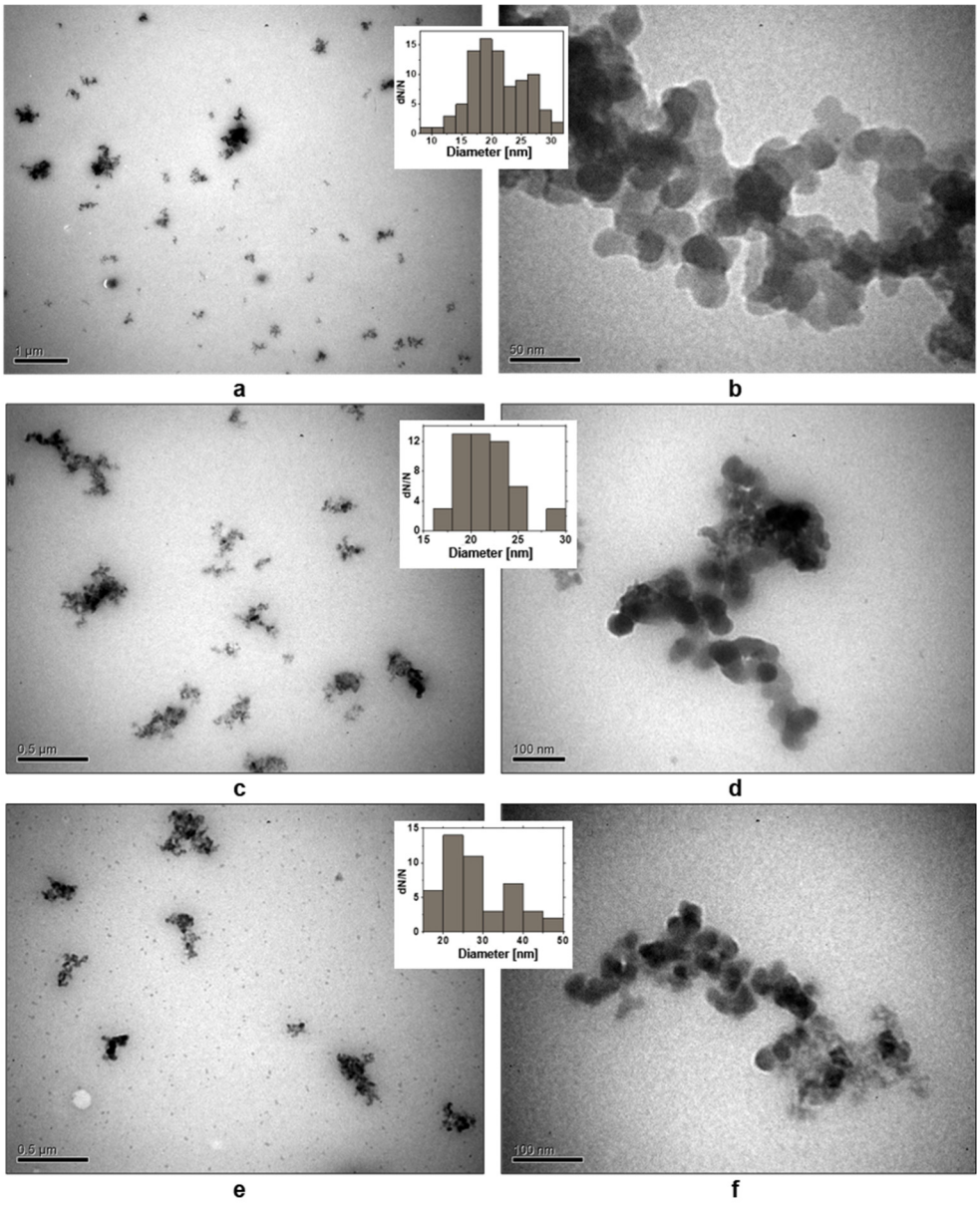

Figure 7. TEM images at different magnifications obtained using aqueous solutions of (**a**,**b**) SPH5, (**c**,**d**) SPH6 and (**e**,**f**) SPH7. The corresponding particle size distributions calculated by ImageJ program are shown as insets. C_{SPH} = 1.0 kg·m^{-3}, T = 20 °C.

Table 5. Structural and hydrodynamic parameters of hybrids.

Hybrid	d_{avSPH} [1] [nm]	h_{avPAAm} [2] [nm]	σ_{lim} [3] [mol·kg^{-1}]	$[\eta]$ [4] [m^3·kg^{-1}]	k [5]
SPH4	17.8 ± 2.4	2.4	-	-	-
SPH5	21.0 ± 4.7	2.8	1.10	0.39	0.11
SPH6	21.6 ± 2.8	3.1	1.86	-	-
SPH7	30.1 ± 9.0	7.3	2.29	0.89	0.25

[1] Average diameter of hybrid particles. [2] Average height (thickness) of the PAAm "corona": $h_{avPAAm} = d_{avSPH}/2 - r_{avSiO2}$. [3] Limiting value of hydroxyl ion absorption. [4] Intrinsic viscosity of solution. [5] Huggin's constant.

Determination of the surface charge of SPH nanoparticles in aqueous solutions was of particular interest, given their subsequent use as nanoreactors and carriers of metal nanoparticles. For this purpose,

potentiometric titration of the initial silica sol and aqueous solutions of SPH5–SPH7 samples with different numbers and lengths of PAAm grafts was carried out [150]. The basis for these experiments was the participation of surface ≡Si–OH groups simultaneously in two schematical equilibria: dissociation (2) and formation of hydrogen bonds (3) with the amide groups of PAAm [150]:

(2)

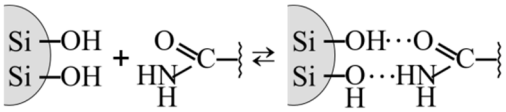

(3)

Therefore, the main task was to determine and compare the total number of ≡Si–OH groups on the surface of the initial SiO_2 sol and the inorganic "core" of hybrids capable of participating in equilibrium (2) and creating a negative surface charge. The results of potentiometric titration of an aqueous dispersion of SiO_2 sol, hybrid solutions and deionized water 0.2 *N* NaOH are presented in Figure 8 in the form of dependences of the absorption value of hydroxyl ions on pH [150]. The value of σ_{OH^-} at a certain pH corresponded to the number of ionized negatively charged silanol groups on the surface of pure silica sol (Figure 8a) and SiO_2 "cores" in the hybrids SPH5 (Figure 8b), SPH6 (Figure 8c), and SPH7 (Figure 8d). In contrast, the limiting value of σ_{lim} was equal to the total number of free silanol groups participating in the dissociation equilibrium (2). In the case of the pure sol, the σ_{lim} value was not reached, *i.e.*, it was higher than 7.33 mol·kg^{-1} (Figure 8a). For all hybrid samples, the σ_{lim} values were successfully determined (Figure 8b–d, Table 5) and showed a sharp decrease in free ≡Si–OH groups on the surface of their silica "cores" compared to the pure SiO_2 sol. The greatest decrease in the σ_{lim} was observed for the SPH5 sample, which contained the largest number of short grafts (Table 2). This indicated the densest structure of the PAAm "corona" in the SPH5 particles.

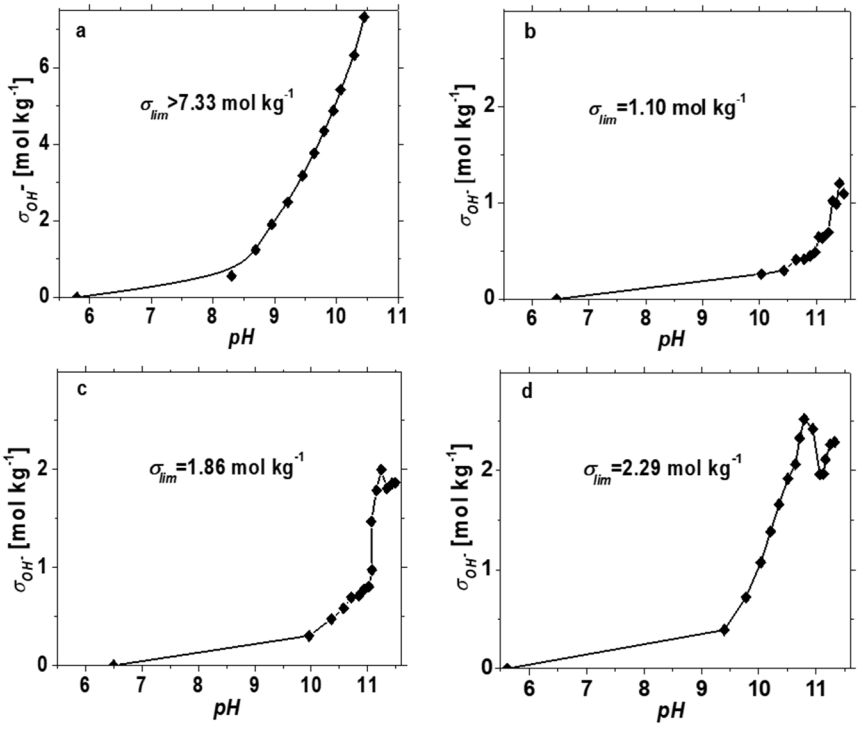

Figure 8. Absorption curves of OH^- ions calculated based on potentiometric titration of (**a**) a dispersion of SiO_2 sol and aqueous solutions of (**b**) SPH5, (**c**) SPH6 and (**d**) SPH7. C_{SiO2} = 0.7 kg·m^{-3}, C_{SPH} = 1 kg·m^{-3}, T = 25 ± 0.1 °C.

The subsequent gradual decrease in the number of grafts in the SPH6 and SPH7 samples, together with the increase in the PAAm chain length, led to an increase in the permeability of the polymer "corona", which was confirmed by a steady increase in the σ_{lim} value in Table 5.

Table 5 also presents the results of the viscometry studies of aqueous solutions of SPH5 and SPH7, carried out in [150]. They are represented by the parameters of the intrinsic viscosity ([η]) and the Huggins constant (k) and demonstrate a significantly higher hydrodynamic volume of SPH7 particles compared to SPH5 and good quality of water as a solvent in relation to both hybrid particles ($k < 0.3$) [151]. These data correlate fully with the changes in the average particle diameter for the two hybrids (Table 5).

Thus, in the SPH5–SPH7 hybrid series, an increase in the size of individual particles, the thickness and permeability of the polymer "corona", as well as the number of free ionic silanol groups on the surface of the inorganic "core" was established.

5. *In Situ* Synthesis of Silver Nanoparticles in Hybrid Matrices

To prepare AgNPs/SPH nanocomposites with small metal nanoparticles in aqueous solutions and under mild conditions, *in situ* reduction of silver nitrate with sodium borohydride as one of the most powerful reducing agents was used. Although this method has been widely used to prepare many nanosilver/polymer composites, its actual mechanism, including nucleation, growth, and crystallization of metal nanoparticles in various polymer matrices and the real role of the latter in these processes, remains poorly understood even today. This aspect was highlighted in our recent publication [152] to stimulate further detailed studies in this direction.

For the *in situ* synthesis of AgNPs in aqueous SPH solutions, an optimal protocol comprising two separate stages was developed [152]. In the 1st stage, after adding the Ag-salt to the SPH solution and keeping the mixture in a dark box for 1 h, the primary amide groups of PAAm could form stable monodentate ion-dipole complexes with Ag^+ ions, as shown in Figure 9 [153]. The high stability of these complexes was confirmed by the high value of $\Delta H° = 176$ kJ·mol^{-1}, which was measured for complexation of Ag^+ ions with low-molecular-weight acetamide in the study [153].

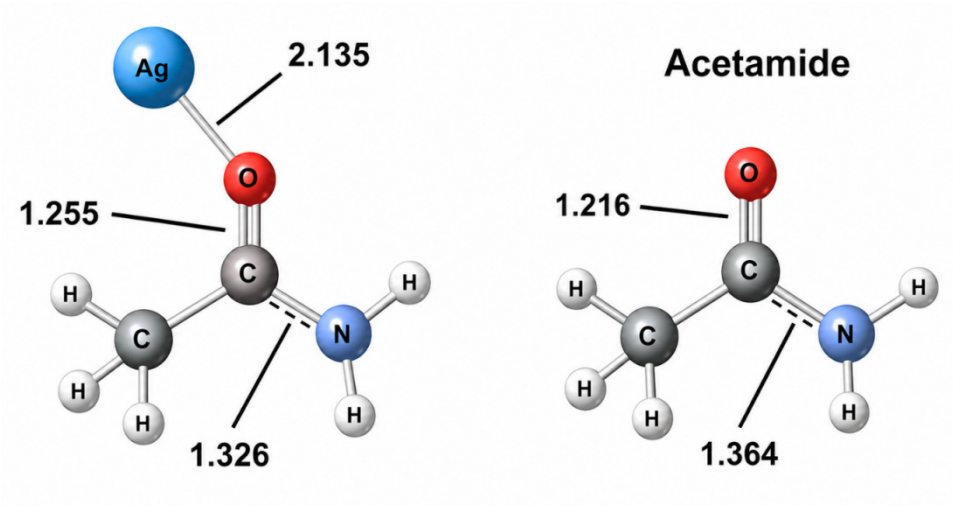

Figure 9. Model of monodentate ion-dipole complexes of Ag^+ ions with primary amides. Changes in the lengths of covalent bonds C=O and C–N in the acetamide molecule under the influence of complex formation are shown.

Moreover, at this time, Ag^+ ions could actively bind to the weakly negatively charged surface of SiO_2 particles via electrostatic interactions. Thus, a high degree of binding of Ag^+ ions by SPH matrices could be expected at the 1st stage of AgNP synthesis. To test this assumption, the degree of binding of silver ions to SPH5 and SPH7 samples at the 1st stage of *in situ* synthesis was experimentally determined [152]. For

this purpose, a potentiometric method was chosen using an Ag^+-selective electrode and separation of hybrid particles with bound Ag^+ ions by reprecipitation with ethanol and subsequent centrifugation. In the range of studied concentrations of matrices and Ag-salt (C_{SPH} = 0.5, 1.0, and 2.0 kg·m^{-3}; C_{AgNO3} = 1.82 × 10^{-2} kg·m^{-3}), a very high, close to 100% degree of binding of Ag^+ ions was found [150].

The addition of $NaBH_4$ in the 2nd stage initiated a reduction process that occurred within the "coronas" of the hybrid particles and on their surfaces. The latter interesting fact was discovered thanks to our recent studies [152]. The process of reduction of Ag-salt with $NaBH_4$ in an aqueous medium can be schematically represented by the following main (4) and side (5)–(7) chemical reactions [154]:

$$2AgNO_3 + 2NaBH_4 = 2Ag + H_2 + B_2H_6 + NaNO_3 \quad (4)$$

$$B_2H_6 + H_2O = 6H_2 + 2H_3BO_3 \quad (5)$$

$$NaBH_4 + 2H_2O = NaBO_2 + 4H_2 \quad (6)$$

$$BH_4^- + H_3O^+ + 2H_2O = H_3BO_3 + 4H_2 \quad (7)$$

The synthesis of AgNPs was carried out in hybrid aqueous solutions with pH = 5.7–6.4. Due to side reactions, in particular, active hydrolysis of $NaBH_4$ in the acidic pH region with a high exothermic effect [155], an eight-fold molar excess of $NaBH_4$ in relation to $AgNO_3$ was used to achieve complete conversion of Ag^+ ions to the zero-valence state.

For many practical applications of silver-containing nanocomposites obtained by chemical reduction of silver salts, it is necessary to purify them from excess reagents and by-products. To solve this problem, a simple, rapid, environmentally friendly, and efficient method for purifying AgNPs/SPH nanocomposites immediately after synthesis was developed [105,152]. The purification procedure consisted of reprecipitation of reaction mixtures with excess ethanol (4:1 v·v^{-1}), their subsequent centrifugation and re-dissolution in deionized water. This opened up the prospect of their successful use in biomedicine, which will be shown below.

6. Control of Kinetics and Yield of Silver Nanoparticles During *In Situ* Synthesis

In some previous studies [105,146], it was shown that the kinetic features of *in situ* AgNP formation in the presence or absence of stabilizing agents can be correctly described by the time variations in the position (λ_{max}) and integrated intensity (S) of the surface plasmon resonance band (SPRB) observed in the UV-Vis spectrum. This approach was based on the well-known optical properties of silver clusters and nanoparticles, as well as on numerous theoretical and experimental studies [152,156–160], which related the position, intensity, and shape of SPRB in extinction spectra to the size, shape, polydispersity, and aggregation of AgNPs in solutions. In particular, according to Mie theory [154], the overall extinction coefficient SPRB depends on both resonance absorption and scattering. However, if the size of spherical silver nanoparticles is too small (<30 nm), resonance absorption makes an overwhelming contribution to the extinction [158]. When the size of AgNPs is much smaller than the wavelength of incident light, the absorption A of a colloidal dispersion containing N particles in an optical cell with path length L can be expressed by Formula (8):

$$A = \frac{(\kappa \cdot L)}{\ln 10} \quad (8)$$

where the extinction coefficient κ for N particles of volume V is determined by Equation (9) [157]:

$$\kappa = \frac{18\pi \cdot N \cdot V \cdot \varepsilon_m^{3/2}}{\lambda} \frac{\varepsilon_2}{[\varepsilon_1 + 2 \cdot \varepsilon_m]^2 + \varepsilon_2^2} \quad (9)$$

In the last formula, λ is the wavelength of the absorbed light, ε_m is the dielectric constant of surrounding medium, which is assumed does not depend on the frequency, ε_1 and ε_2 are the real and imaginary parts of the dielectric function of the material: $\varepsilon(\omega) = \varepsilon_1(\omega) + i \cdot \varepsilon_2(\omega)$, where ω is the angular frequency of the light. The width of the SPRB depends mainly on the imaginary part of the dielectric function, which is responsible for the dissipation of the electric field energy. However, for silver, unlike other metals, $\varepsilon_2(\omega)$ value is insignificant and weakly depends on frequency [157]. Thus, in the specified range of AgNP sizes, the intensity of SPRB depends mainly on the concentration of the particles rather than on their size [156,157,159]. This property of SPRB became the basis for characterizing the kinetic features of the appearance and accumulation of AgNPs under various conditions and time intervals, especially in the first minutes after the onset of the reduction process. With their help, we revealed the kinetic features of AgNP formation in aqueous solutions of poly(vinyl alcohol)/PAAm graft copolymers [161] and later SPH [105,152].

Examples of kinetic studies of AgNP formation in aqueous hybrid solutions with two concentrations of the initial Ag-salt (and $NaBH_4$), carried out by UV-Vis spectroscopy, are presented in Figure 10 [161]. The formation of small spherical AgNPs during *in situ* synthesis results in the appearance of a single narrow SPRB in the UV-Vis spectra with λ_{max} = 380–425 nm [156–161]. These AgNPs were formed in a hybrid solution at a lower Ag-salt concentration of 1.82×10^{-2} kg·m^{-3} (Figure 10a). This was confirmed by the presence of a narrow unimodal SPRB with λ_{max} = 379–400 nm in the spectra. Then, the changes in the position (λ_{max}) and integrated intensity (S) of the SPRB over time were analyzed. The first parameter characterized the size of the AgNPs [105,162], while the second, in the case of very small AgNPs determined the yield of nanoparticles [105]. The overall yield of AgNPs in the reduction reactions was estimated by the S value achieved after a certain time (after 60 min). To determine the integral intensity of SPRB, its graphical integration in the spectrum was performed using the Origin program. The changes in the position and integral intensity of SPRB with time in these examples are shown in Figure 10c,d.

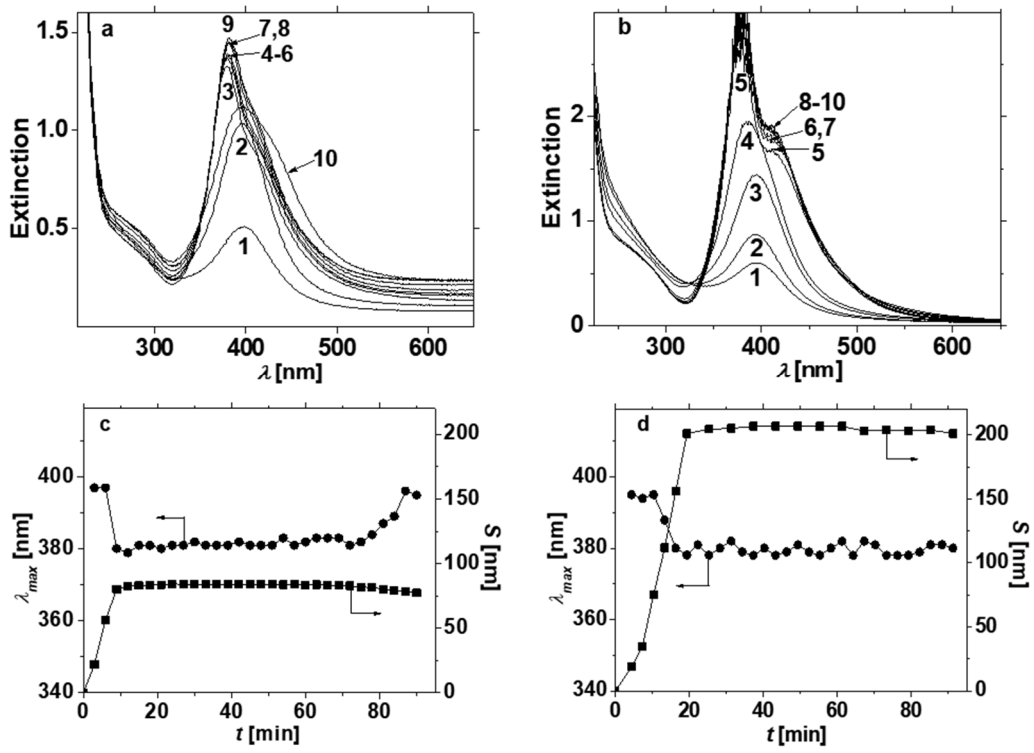

Figure 10. (**a**,**b**) Time evolution of the extinction spectra of the $AgNO_3$/SPH6 mixture through 3—*1*, 6—*2*, 9—*3*, 12—*4*, 15—*5*, 21—*6*, 36—*7*, 60—*8*, 72—*9*, and 90 min—*10* after adding the reducing agent. (**c**,**d**) Time dependences of the position (λ_{max}) and integrated intensity (S) of SPRB of AgNPs formed in SPH6 carriers. C_{SPH} = 1.0 kg·m^{-3}, C_{AgNO3} = 1.82×10^{-2} (**a**,**c**) and 3.64×10^{-2} kg·m^{-3} (**b**,**d**), C_{NaBH4}/C_{AgNO3} = 8 mol·mol^{-1} (**a**–**d**), T = 20 °C.

A sharp decrease in λ_{max} (AgNP size) from 396 to 379 nm between 6 and 9 min of measurement was observed for the lower Ag-salt concentration (Figure 10c). This correlated with a sharp increase in the nanoparticle yield over the same time period (Figure 10c). This effect reflected the ordering or crystallization of the primary AgNPs. The subsequent weak dependence of λ_{max} on time up to 78 min can be explained by the almost constant size of the AgNPs during this time period. A further gradual increase in the AgNP size, which was reflected by a small increase in λ_{max}, continued until 24 h (not shown). After this, a stable AgNPs/SPH4 composite was obtained over time.

The integrated intensity of SPRB, reflecting the yield of metal nanoparticles, increased rapidly with time to some constant value (Figure 10c,d). The value of S_{60} = 207 nm for C_{AgNO3} = 3.64 × 10^{-2} kg·m^{-3} was more than 2 times higher than S_{60} = 83 nm for C_{AgNO3} = 1.82 × 10^{-2} kg·m^{-3}, indicating a significant increase in the yield of AgNPs with increasing salt concentration. In addition, the position of SPRB also decreased sharply in the first 10–15 min, reflecting the process of ordering or crystallization of primary AgNPs [105]. At the same time, the shape of intense SPRBs for AgNPs obtained at a higher concentration of Ag-salt (Figure 10d) differed significantly from those observed at half the concentration of Ag-salt (Figure 10c). Indeed, in the interval from 12 to 15 min, a second SPRB sharply appeared in the UV-Vis spectra with λ_{max} ≈ 412 nm (Figure 10d). Interestingly, the positions of both maxima and their total integrated intensity S remained virtually unchanged over the next 90 min. This unexpected result was explained by drastic structural changes in some hybrid matrices caused by the simultaneous growth of many AgNPs in them. It was assumed that the simultaneous growth of several AgNPs in one hybrid particle can lead to the detachment of grafted PAAm chains from the SiO_2 surface due to the rupture of hydrogen bonds. Our recent study [152] devoted to the creation of AgNPs/SPH nanocomposites with different densities of metal nanoparticles fully confirmed this conclusion.

7. Structure of Silver/Hybrid Nanocomposites Depending on Some Key Factors

Two examples of the real morphology of hybrid structures with AgNPs for SPH4 and SPH6 samples and their schematic representation are shown in Figures 11 and 12. The TEM image in Figure 11a clearly demonstrates the presence of two morphological forms of particles existing in the solution, such as swollen diffuse hybrid nanoparticles with the average size d_{av} = 27.4 ± 5.4 nm and small dense spherical AgNPs with the diameter d_{av} = 3.1 ± 1.5 nm, most of which are incorporated into the hybrid matrices (Figure 11a). The pattern obtained for the purified AgNPs/SPH4 composite with a lower nanosilver concentration (C_{AgNO3} = 1.82 × 10^{-2} kg/m^3) was in complete correlation with the schematic structure shown in Figure 11b. Comparison of the compact, highly aggregated SPH4 particles in Figure 6a,b, with the swollen, predominantly isolated hybrid particles in Figure 11a allowed us to draw an important conclusion about the significant disaggregation of matrix particles during the *in situ* synthesis of AgNPs. It was obvious that such disaggregation was initiated by the intense growth of silver particles in the SPH matrices.

A somewhat different situation was observed in the TEM images in Figure 12a,b, which reflected the morphology of the purified AgNPs/SPH6 composite with a higher (twice) concentration of nanosilver (C_{AgNO3} = 3.64 × 10^{-2} kg·m^{-3}). In these micrographs, only individual isolated swollen particles of the SPH6 matrices could be seen. Most of the matrix particles seemed to "dissolve" in the solution, making it impossible to determine their sizes (Figure 12a,b). As subsequent studies showed [152], the apparent "dissolution" effect was a consequence not only of the disaggregation of matrix particles during AgNP growth, but also of the detachment of the grafted PAAm chains from the SiO_2 "cores" when the AgNP concentration in the nanocomposite became too high. In contrast, the size and size distribution of AgNPs could be easily determined (Figure 12, inset); d_{av} = 2.4 ± 1.0 nm.

In the study [152], a special series of kinetic and structural studies of the two-stage process of AgNPs/SPH composite formation was conducted with the aim of identifying a more detailed mechanism of AgNP formation in hybrid solutions depending on the matrix structure and reagent concentrations. For

this purpose, two hybrid samples were used, in particular SPH5 and SPH7 in Table 5, which have different heights and permeabilities of the PAAm "corona". The significant influence of the initial concentration of Ag-salt (the amount of formed AgNPs) on the final state of the nanocomposites was fully confirmed.

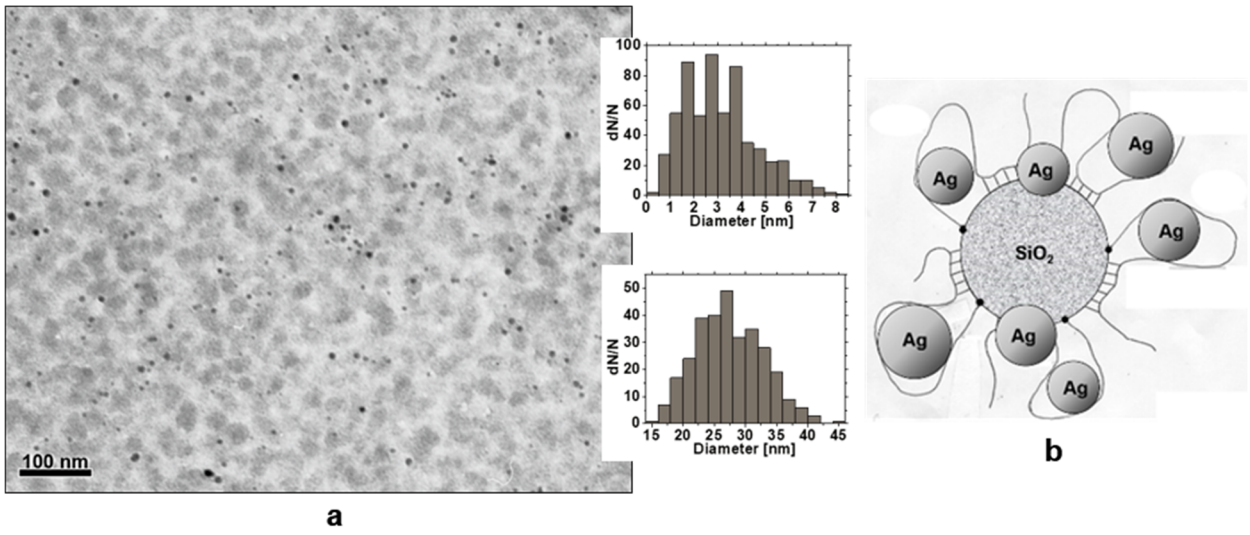

Figure 11. (**a**) TEM image of AgNPs/SPH4 nanocomposite and calculated size distributions for AgNPs (upper inset) and swollen hybrid particles (lower inset). (**b**) Schematic particle structure of AgNPs/SPH composite. C_{SPH} = 1.0 kg·m^{-3}, C_{AgNO3} = 1.82 × 10^{-2} kg·m^{-3}, T = 20 °C.

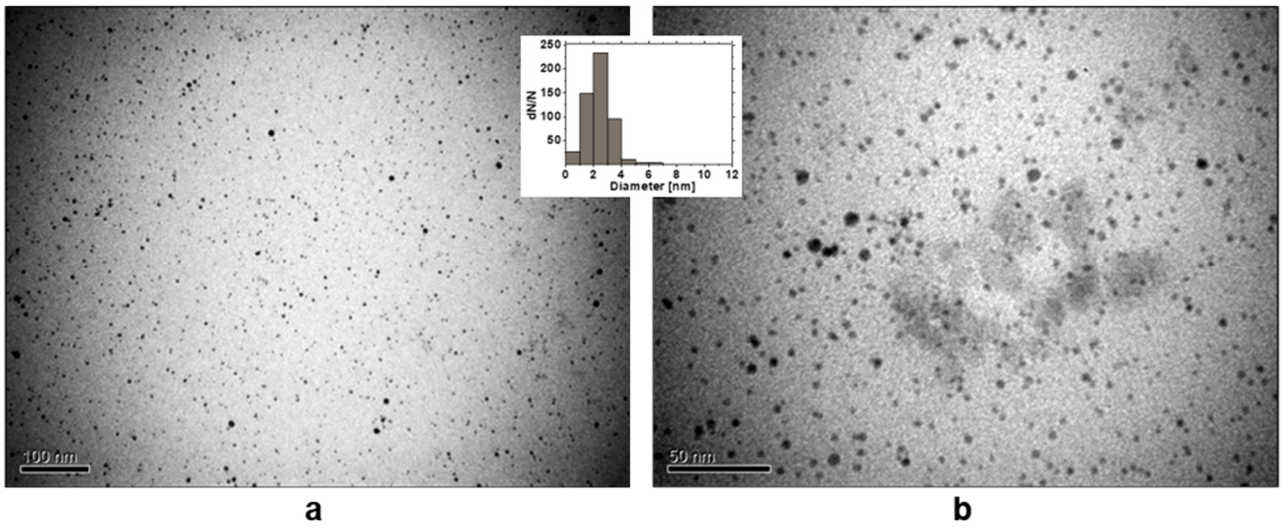

Figure 12. TEM images of the AgNPs/SPH6 nanocomposite obtained at (**a**) lower and (**b**) higher magnifications. The size distribution of AgNPs calculated by ImageJ program is represented in the inset. C_{SPH} = 1.0 kg·m^{-3}, C_{AgNO3} = 3.64 × 10^{-2} kg·m^{-3}, T = 20 °C.

One of the most important results here was also the presence of two types of AgNPs (internal and external) in the final nanocomposites, which arose due to the binding of Ag^+ ions and their subsequent reduction both in the internal space of the hybrid "corona" and on its surface. The structure of the polymer "corona" affected the ratio of both reduction processes. When the "corona" was denser and thinner, the process of Ag^+ ion binding and reduction on its surface was dominant. However, with a thicker and more permeable PAAm layer in SPH particles, there was a predominant formation of many small AgNPs inside the polymer layer at a low concentration of Ag-salt. Their number could also increase with increasing salt concentration even without swelling of the matrix. Purification of the nanocomposites from excess reagents and by-products transformed them into fairly homogeneous systems. They contained highly swollen SPH

particles that formed networks of entanglements in an aqueous medium, thereby stabilizing small AgNPs for a long time.

The crystal structure of AgNPs in SPH composites after drying was confirmed by wide-angle X-ray scattering (WAXS) method. Examples of WAXS and SAXS diffraction patterns for the AgNPs/SPH4 nanocomposite are shown in Figure 13 [147].

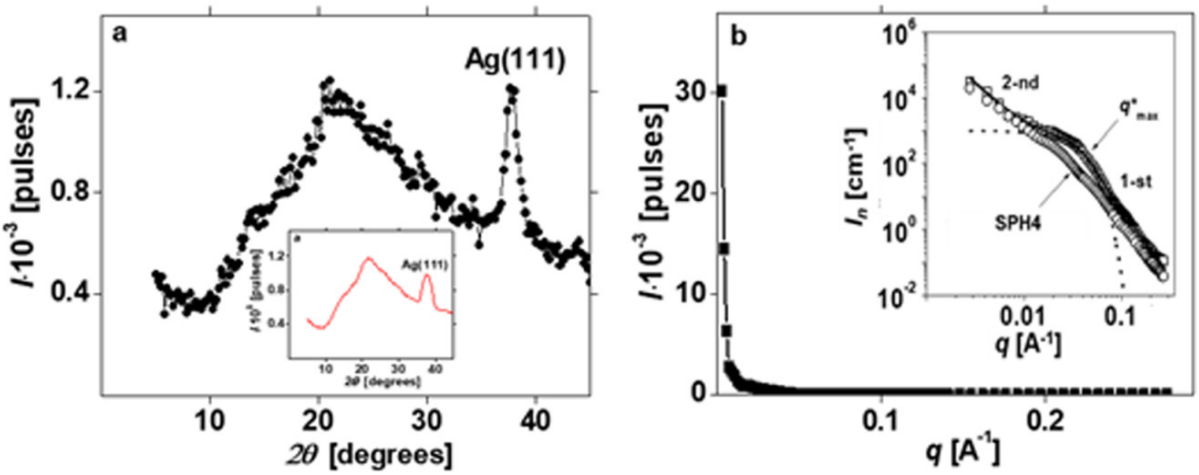

Figure 13. (**a**) Wide-angle and (**b**) small-angle X-ray scattering intensities as a function of scattering angle θ and wavevector q, respectively, for the AgNPs/SPH4 nanocomposite. The smoothed WAXS profile and the log-log SAXS profile are shown as insets. T = 20 °C. In the inset of panel (**b**) the breakpoint q^* indicates the transition between two structural regimes.

The bulk sample of AgNPs/SPH4 composite was prepared after *in situ* synthesis from an aqueous solution (C_{SPH} = 2.0 kg·m^{-3}, C_{AgNO3} = 3.64 kg·m^{-3}) placed in a Teflon mold in a dark box, and dried in air and in a vacuum desiccator. As can be seen from the WAXS profile in Figure 13a, the bulk composite included amorphous regions of the hybrid, manifested by two diffuse overlapping maxima at $2\theta_1 \approx 14.3°$ and $2\theta_2 = 21.2°$, and AgNPs inclusions showing a crystalline peak of silver (111) at $2\theta_3 = 38°$ (Table 6). The latter peak indicated the presence of crystalline AgNPs with a tetragonal fcc lattice [163]. The presence of two overlapping diffusion maxima in this diffraction pattern was explained [146,147] by the existence of two systems of paracrystalline lattice planes in the amorphous regions of the hybrid (consisting mainly of PAAm chains).

Table 6. Parameters of nanocomposite at molecular and supramolecular fractal levels.

Composite	Diffraction Maximums			Interplane Distances			D_f [(1)]		R_{gAgNPs} [(2)] [nm]	
	$2\theta_1$°	$2\theta_2$°	$2\theta_3$°	d_1 [nm]	d_2 [nm]	d_3 [nm]	1st Level	2nd Level	Exp.	Calc.
AgNPs/SPH4	~14.3	21.2	37.8	~0.619	0.419	0.238	4.0	2.5	5.8	5.5

(1) Fractal size. (2) The average radius of gyration for AgNPs, found from SAXS data: $R_g = d_{max}/2(5/3)^{1/2}$ and calculated using the Beaucage approach [148].

The first maximum with less intensity at $2\theta_1 \approx 14.3°$ characterized the lateral periodicity in the arrangement of PAAm chains, and the second, more intense maximum at $2\theta_2 = 21.2°$ reflected the periodic arrangement of planar hydrogen-bonded *cis*-dimers of amide groups in the structures of *cis-trans*-multimers [147]. The average interplane distances in the paracrystalline lattice of amorphous polymer regions (d_1 and d_2) and in the crystal lattice of silver nanoparticles (d_3), calculated using the Bragg ratio, are presented in the central part of Table 6.

In contrast, the SAXS diffraction pattern in Figure 13b demonstrated a sharp drop in scattering intensity with increasing q without any diffraction maxima. This allowed us to conclude that there is no periodicity in the arrangement of the composite structural elements. More interesting was the double logarithmic SAXS profile, shown as an inset in Figure 13b. Here, two linear sections with different slopes D_f, corresponding to two power scattering regimes by Porod, were clearly visible (Table 6). These lines were related by the exponential scattering regime by Gineau and indicated a two-level fractal organization of the AgNPs/SPH4 nanocomposite structure. For the 1st structural level, the fractal size $D_f = 4$ (Table 6), which characterized the power scattering regime by Porod on dense solid particles with a smooth surface [148]. This fact additionally confirmed the formation of dense (crystalline) AgNPs in SPH matrices. The average radius of gyration for these nanoparticles was determined using the value $d_{max} \approx 2\pi/q^*$ (where q^* was determined in Gineau's scattering region) and the ratio $R_g = d_{max}/2(5/3)^{1/2}$ [147,148] (Table 6). Thus, small crystalline AgNPs with $R_g = 5.8$ nm formed the 1st level of the fractal-organized structure of this composite.

Individual elements of the 2nd, higher level in the structural organization of the AgNPs/SPH4 composite were mass-fractal clusters consisting of fragments of polymer chains. This conclusion was based on the fractal size $D_f = 2.5$ (Table 6), which was found for this structural level from Figure 13b [147]. This value was somewhat higher than for mass-fractal clusters in the structure of the individual hybrid (Figure 13b, Table 4). In these works, we also simulated the SAXS profile for the AgNPs/SPH4 composite using the method of global unified exponential-power functions of Beaucage [148] and taking into account two levels of its structural organization. The resulting curve without points is shown in Figure 13b. As a result, the calculated value of $R_{g(calc)}$ for AgNPs in the composite structure was in good agreement with the similar value found from the experimental SAXS profile (Table 6).

8. Stability of Nanocomposites Under Various Conditions

The stability of AgNPs depends on several factors, including pH, concentration, temperature, light exposure, the presence of reactive species, surface chemistry, and storage conditions. As mentioned earlier, stabilizers of various nature, also known as capping agents, play a crucial role in preventing nanoparticle aggregation. Considering the possible application of AgNPs/SPH nanocomposites as disinfectants, components of hygienic materials, and in biomedicine, it was important to monitor the changes in their state under the influence of various extraneous factors. Therefore, their behavior in "salt solutions", over time, at different pH values, upon dilution, and in the light was of particular interest. The data of time monitoring of UV-Vis spectra for one of the purified nanocomposites (AgNPs/SPH6) after adding sodium chloride to $C_{NaCl} = 9.0$ kg·m^{-3}, sodium hydroxide to pH = 9, and hydrochloric acid to pH = 2 are presented in Figure 14.

The first important result here was the absence of any changes in the position and integrated intensity of SPRB of AgNPs in SPH carriers during 90 min upon addition of NaCl and NaOH (Figure 14a,b). This meant that the metal nanoparticles remained completely stable in the composite in the "saline solution" and at pH ≈ 9. A different picture was revealed upon the addition of HCl (Figure 14c). There was a slow decrease in the integrated intensity of SPRB (Figure 14c,d), which was caused by the gradual dissolution of AgNPs in SPH carriers at pH ≈ 2. In contrast, the position of SPRB with $\lambda_{max} = 405$ nm was constant for 45 min and then began to decrease, demonstrating a slow decrease in the size of AgNPs (Figure 14d). Similar dissolution of AgNPs in polyvinylpyrrolidone carriers in the acidic pH region was also found in the study [163,164]. At the same time, the dissolution rate of AgNPs in SPH carriers was relatively low, since it did not end even after 1.5 h (Figure 14d). The chemical stability of the nanocarriers themselves under similar experimental conditions was ensured by the properties of individual components. In particular, the rate of possible hydrolysis of PAAm chains in the acidic and alkaline pH ranges was insignificant at the low temperatures studied [143], whereas the possible slow dissolution of SiO_2 nanoparticles could only occur at higher pH values [110].

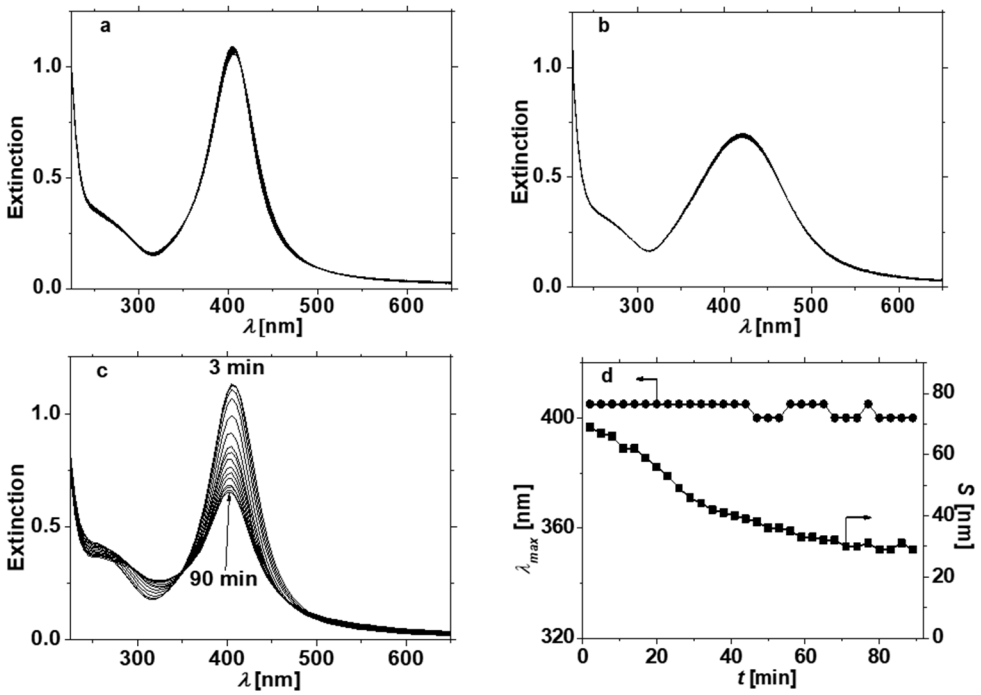

Figure 14. Extinction spectra of the AgNPs/SPH6 nanocomposite recorded for 90 min under following conditions: (**a**) with the addition of NaCl, (**b**) at pH = 9 and (**c**) at pH = 2. (**d**) Time dependences of the position and integrated intensity of SPRB of AgNPs calculated using figure (**c**). C_{SPH} = 1.0 kg·m^{-3}, C_{AgNO3} = 1.82×10^{-2} kg·m^{-3}, C_{NaCl} = 9.0 kg·m^{-3}, T = 22 °C.

The next important test concerned monitoring the long-term stability of the purified AgNPs/SPH6 nanocomposite during storage under various conditions, including light. It turned out that the stability of the nanocomposite to the effects of time and light was determined by the concentration of AgNPs in the hybrid carriers (according to C_{AgNO3} in Figure 15).

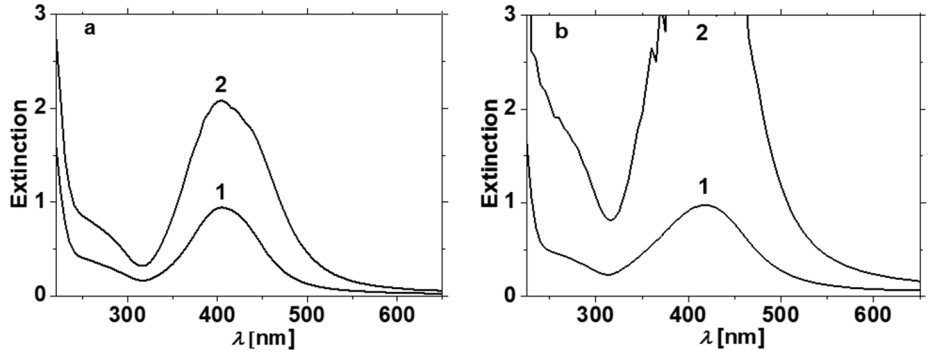

Figure 15. Extinction spectra of the AgNPs/SPH6 nanocomposites obtained at C_{AgNO3} = 1.82 × 10^{-2}—*1* and 3.64 × 10^{-2} kg·m^{-3}—*2* after storage: (**a**) for 3 months in a dark box and (**b**) for the next 4 months in the light. T = 22 °C.

At a lower value of C_{AgNO3} = 1.82 × 10^{-2} kg·m^{-3} (lower amount of AgNPs), the composite retained long-term stability regardless of its storage in a dark box (Figure 15a) or in the light (Figure 15b). Over the studied time, only a slight increase in the λ_{max} value of the corresponding SPRB (from 405 to 416 nm) and its integrated intensity S (from 73 to 83 nm) in the UV-Vis spectrum was observed (Figure 15a,b; spectra 1). The light stability of the composite with a higher value of C_{AgNO3} = 3.64 × 10^{-2} kg·m^{-3} (a larger amount of AgNPs) was significantly lower (Figure 15a,b; spectra 2). Obviously, in this case, SPH6 carriers with extended PAAm chains (see Section 7) provided less protection of AgNPs from their aggregation under the influence of light.

Another experiment was devoted to the stability of this nanocomposite to dilution, which can initiate the release of a part of AgNPs from the carriers under the action of the concentration gradient of particles inside the carriers and in the environment. For this study, the AgNPs/SPH6 nanocomposite with C_{AgNO3} = 3.64 × 10^{-2} kg/m^3 was prepared, purified from by-products, diluted 2-fold, and kept for 24 h. Then it was reprecipitated with ethanol and centrifuged. The absence of SPRB in the UV-Vis spectrum of the supernatant was a criterion for the complete stability of the studied composite to the release of AgNPs due to their strong retention by the hybrid carriers.

9. Antibacterial and Antifungal Activity of Silver Nanoparticles in Hybrid Carriers

Along with fundamental studies of the processes of AgNP formation in hybrid solutions and the structural features of the obtained nanocomposites, their potential as highly dispersed biocidal and disinfectant agents was revealed. First, the biological effects of one of the silver/hybrid composites (AgNPs/SPH4) on several bacterial and fungal cultures, which are traditional pathogens of hospital infections, were assessed [149]. The selected composite consisted of swollen SPH4 nanoparticles (d_{av} = 27.4 ± 5.4 nm) containing dense spherical AgNPs with a diameter of d_{av} = 3.1 ± 1.5 nm (Figure 11). In these experiments, the following test cultures were used: *Staphylococcus aureus* (ATCC 25923) and *Pseudomonas aeruginosa* (ATCC 27853) bacteria, *Candida albicans* yeast, and *Fusarium oxysporum* (150 FCKU) and *Cladosporium shpaerospermum* (312 FCKU) mycelial fungi from the Taras Shevchenko National University of Kyiv collection of microscopic fungi. The effect of AgNPs/PIH4 dispersion with initial concentrations of C_{SPH} = 2 kg·m^{-3} and C_{AgNPs} = 1.2 × 10^{-2} kg·m^{-3} on the test cultures was studied by the agar diffusion method: for bacteria—the disk method, for mycelial fungi—the wells in agar method. The presence or absence of a zone of inhibition of microorganism growth around the disk or well of agar and its diameter were assessed. The cell content in the bacterial suspension was 1.5 × 10^8 colony-forming units (CFU) cm^{-3}, while the number of spores of mycelial fungi in the suspension corresponded to 1 × 10^6 CFU cm^{-3}.

According to microbiological tests, aqueous solutions of the AgNPs/SPH4 composite showed both biocidal and biostatic effects of varying degrees with respect to the gram-positive and gram-negative bacteria used, as well as mycelial fungi. Examples of the effects of the original composition and its dilutions on bacterial cultures of *Staphylococcus aureus* and *Pseudomonas aeruginosa* are shown in Figure 16a–d. The biocidal effect of the original composition and its diluted solutions 1:10 and 1:100 was revealed with respect to both bacterial cultures. Indeed, the growth inhibition zones after 24 h corresponded to 7, 10–12, and 11 mm, respectively, in the case of *Staphylococcus aureus* (Figure 16a) and 9–10, 11–13, and 11–12 mm in the case of *Pseudomonas aeruginosa* (Figure 16c). The biocidal effect persisted for the next 3–5 days (Figure 16b,d), *i.e.*, it was prolonged.

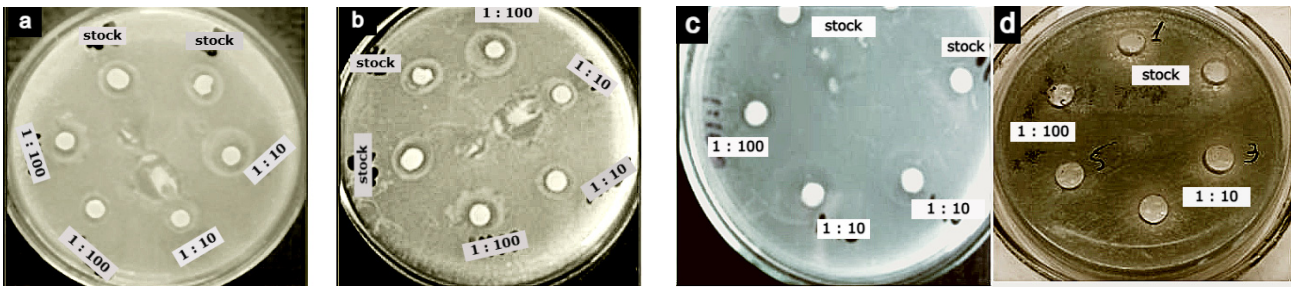

Figure 16. Growth inhibition zones of (**a**,**b**) *Staphylococcus aureus* and (**c**,**d**) *Pseudomonas aeruginosa* bacteria under the influence of the stock and 1:10 and 1:100 diluted AgNPs/SPH4 nanocomposite after (**a**,**c**) 24 h, (**b**,**d**) 4 days. T = 35 °C.

The effect of the AgNPs/SPH4 nanocomposite of different concentrations on the reproduction of two types of mycelial fungi is shown in Figure 17. The composite had a fungicidal effect on the test cultures of

Fusarium oxysporum and *Cladosporium sphaerospermum* during the first 3–5 days of cultivation (Figure 17a–c,e). The growth inhibition zones in these cases were 12–13 and 14–15 mm, respectively. The fungicidal and fungistatic effect of the composition on *Fusarium oxysporum* fungi was stable and prolonged, since it manifested itself in the form of growth inhibition zones and further growth inhibition for 30 days.

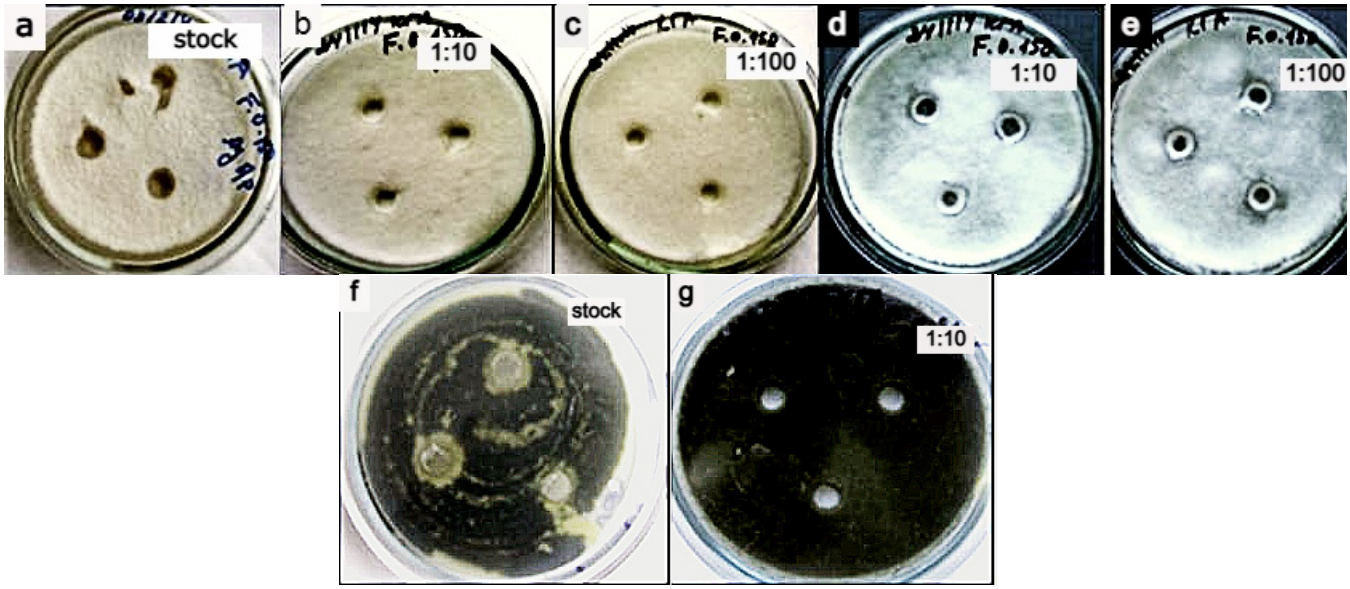

Figure 17. Zones of growth inhibition of filamentous fungi (**a**–**e**) *Fusarium oxysporum* and (**f**,**g**) *Cladosporium sphaerospermum* under the influence of (**a**,**f**) the original AgNPs/SPH4 nanocomposite and diluted (**b**,**d**) 1:10 and (**c**,**e**,**g**) 1:100 times, which were observed after (**a**–**c**,**f**) 5, (**g**) 9 and (**d**,**e**) 18 days. T = 28 °C.

As for the test culture of *Candida albicans* yeast, only the biostatic effect of the AgNPs/SPH4 composite was established (data not shown). Only growth inhibition zones were observed, in which the yeast growth rate decreased. Interestingly, the biocidal and biostatic effect of this composite, diluted 10 and 100 times, was more pronounced in almost all experiments [149].

Recently, new antibacterial tests were carried out with two nanocomposites AgNPs/SPH5 and AgNPs/SPH7, in which the hybrid matrices differed in the number and length of PAAm chains (Table 2), which resulted in different heights and permeabilities of the polymer "corona" (Table 5) [152]. Despite this, the size of AgNPs in both composites was similar (d_{av} = 6.1–6.2 nm). The studies were carried out by diffusion and broth microdilution methods using bacterial strains of gram-positive *Staphylococcus aureus* (ATCC 6538) and gram-negative *Escherichia coli* (ATCC 25922), and *Pseudomonas aeruginosa* (ATCC 27853) [152]. The initial concentrations of the components in both nanocomposites were C_{SPH} = 1 kg·m^{-3} and C_{AgNPs} = 5 × 10^{-2} kg·m^{-3}. Two series of experiments were conducted. First, the cell concentration was varied at a constant metal concentration of each composite. Then, the C_{AgNPs} in the composites were varied, and the bacterial concentration was maintained constant. Because of these experiments, the diameters of the bacterial growth inhibition zones and the minimum inhibitory concentrations (MIC) were found. The obtained MIC values were compared with those for the antibiotics ciprofloxacin, tetracycline, and ceftriaxone, commonly used against the aforementioned bacterial pathogens.

As a result, both studied nanocomposites demonstrated high antibacterial efficiency against *S. aureus*, *E. coli,* and *P. aeruginosa*. The found MIC values were in the range of (1.25–2.5) × 10^{-3} kg·m^{-3}, which are lower than those for ciprofloxacin but comparable to those for ceftriaxone and tetracycline, depending on the bacterial strain. Antibacterial efficiency was highly dependent on the AgNPs concentration. Thus, the growth inhibition zones increased significantly with increasing C_{AgNPs} from 1.25 × 10^{-3} to 5.0 × 10^{-3} kg·m^{-3}. This allowed us to conclude that increasing the AgNPs content in SPH matrices may be a promising way to improve the antibacterial properties of these nanocomposites [152].

10. Silver/Hybrid Nanocomposites for Disinfection of Hygienic Materials and Wound Healing

The incorporation of AgNPs into textiles and various related hygienic materials, such as napkins, bandages, plasters, face masks, *etc*., is one of the important areas of nanoparticle application today. Therefore, methods for creating biocidal textiles are actively discussed in the literature, including introducing AgNPs into various fibers (cotton, sheep wool, polyamide, polyester, *etc.*) or modifying the fabric surface [165–169]. Considerable attention has been paid to the *in situ* reduction of Ag precursors either in textile fibers [165], directly on the original fabric surface [167,168], or on a surface pre-modified with a reactive hyperbranched polymer [166]. At the same time, work [169] showed that coating cotton fabric with a separately formed nanocomposite including AgNPs (based on kappa-carrageenan) is more effective than direct synthesis of AgNPs on fabric, since in this way it is possible to achieve a more than twofold increase in the silver content on the fabric surface. These works also considered the urgent problem of ensuring the safety of embedded metal nanoparticles during washing.

The aim of our research in this direction was to demonstrate the great potential of using AgNPs/SPH nanocomposites for creating biocidal wound dressings, underwear, and other clothing with firmly fixed silver nanoparticles by simply impregnating cotton fabric with nanocomposite solutions or directly treating the fabric or clothing by spraying the nanocomposite, followed by short-term thermal treatment. Therefore, the first task was to study the antimicrobial activity of cotton fabric samples impregnated with one of the AgNPs/SPH composites. In these experiments, fragments of sterile cotton fabric (30 × 30 mm) were treated with the original AgNPs/SPH4 nanocomposite (C_{SPH} = 2 kg·m^{-3}, C_{AgNPs} = 1.2 × 10^{-2} kg·m^{-3}) and its three dilutions: 1:10, 1:100, and 1:1000 [149]. Then, the antimicrobial activity of the cotton pieces was studied using the bacteria *Staphylococcus aureus* (ATCC 25923) and *Pseudomonas aeruginosa* (ATCC 27853), the yeast *Candida albicans,* and filamentous fungi such as *Aspergillus ustus* (165 FCKU), *Cladosporium shpaerospermum* (312 FCKU), *Fusarium oxysporum* (150 FCKU), and the black yeast-like fungus *Exophiala alcalophila* (304 FCKU). In addition, two additional fungi species, *Penicillium variabile* and *Exophiala alcalophila*, were used as test cultures. An aqueous solution of benzalkonium chloride (BC) with C_{BC} = 30 kg·m^{-3} was used as a control biocidal preparation. The microbiological research methodology was the same as described above in Section 9.

Three examples of the biocidal action of the AgNPs/SPH4 composite on *Staphylococcus aureus* and *Pseudomonas aeruginosa* bacteria are shown in Figure 18a–c.

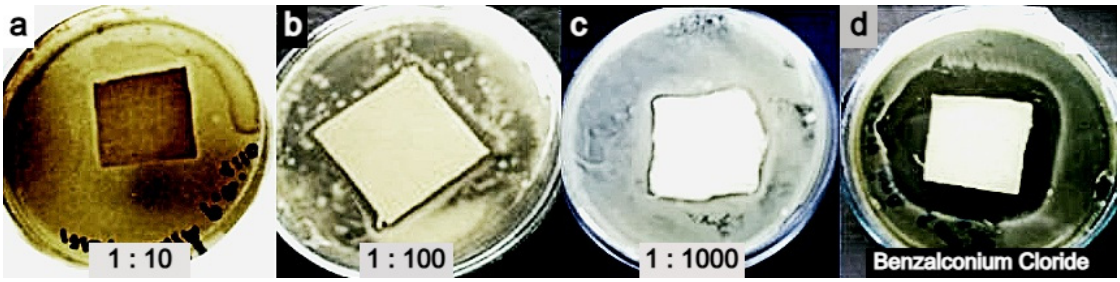

Figure 18. Zones of bacterial growth inhibition of (**a**) *Pseudomonas aeruginosa* and (**b**–**d**) *Staphylococcus aureus* under the action of AgNPs/SPH4 nanocomposite diluted in (**a**) 1:10, (**b**) 1:100, and (**c**) 1:1000 times, and (**d**) benzalkonium chloride (C_{BC} = 30 kg·m^{-3}) after 3 days. T = 35 °C.

Around the fabrics treated with composites, in which C_{AgNPs} varied in a very wide range from 1.2 × 10^{-2} to 1.2 × 10^{-5} kg·m^{-3}, growth inhibition zones of 2.7–3.3 mm remained. For cotton fabric treated with the BS biocidal agent with a significantly higher concentration of the active substance, similar zones were 9–11 mm (Figure 18d). In the control variant, when pieces of fabric were moistened with sterile water, growth inhibition zones of microorganisms were absent. Further examples relate to the effect of the AgNPs/SPH4 composite on various fungi (Figure 19).

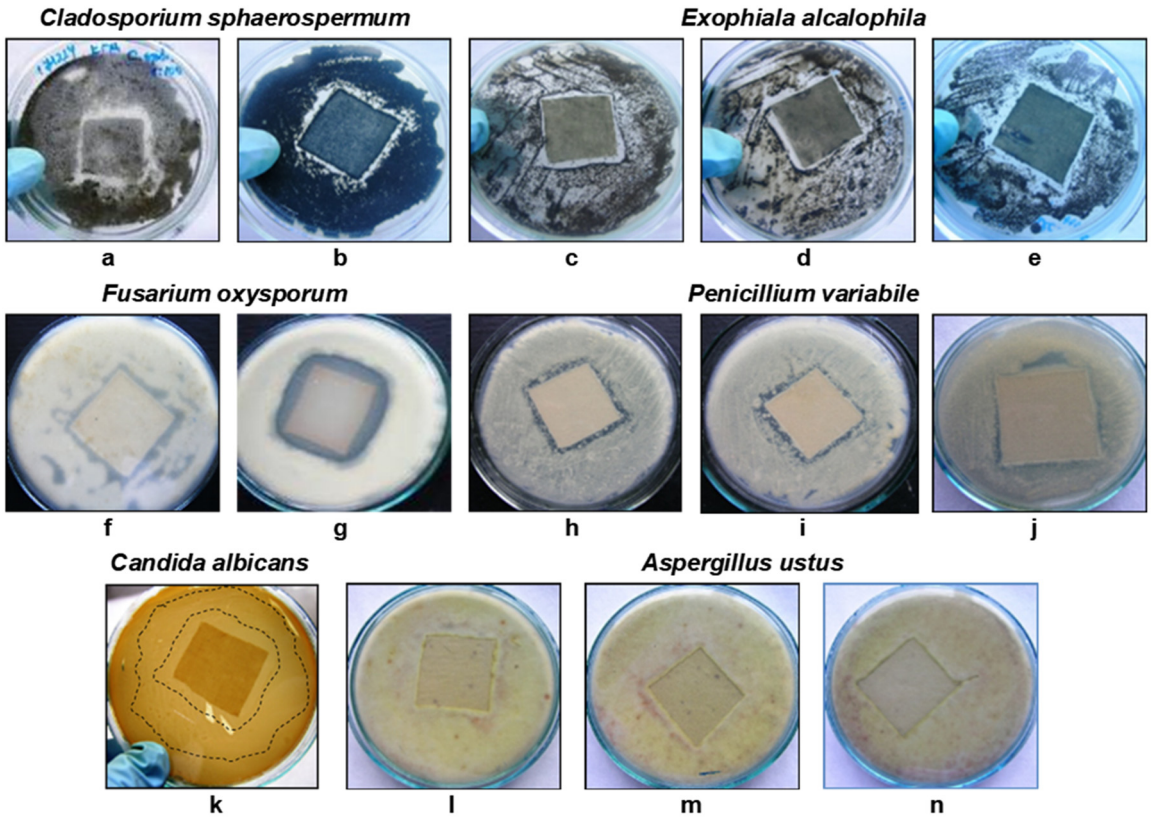

Figure 19. Growth inhibition zones of fungi (**a**,**b**) *Cladosporium sphaerospermum*, (**c**–**e**) *Exophiala alcalophila*, (**f**,**g**) *Fusarium oxysporum*, (**h**–**j**) *Penicillium variabile*, (**k**) *Candida albicans*, and (**l**–**n**) *Aspergillus ustus* under the action of AgNPs/SPH4 nanocomposite diluted in (**c**,**f**,**h**,**k**,**l**) 1:10, (**a**,**d**,**i**,**m**) 1:100, and (**b**,**e**,**j**,**n**) 1:1000 times. (**g**) Benzalkonium chloride (C_{BC} = 30 kg m^{-3}). T = (**a**–**j**,**l**–**n**) 28 °C and (**k**) 35 °C. Dashed line in (**k**) represents impregnation areas; none inhibition for *C. albicans* was observed.

The width of the growth inhibition zones formed around the cotton fragments ranged from 2 to 6.5 mm for dark-pigmented fungi such as *Cladosporium sphaerospermum* (Figure 19a,b) and *Exophiala alcalophila* (Figure 19c–e). The effect of the composition on the yeast-like fungi *Candida albicans* was expressed in the formation of a large growth inhibition zone (14–27 mm) after 2 days (Figure 19k). However, after 3 days, this zone decreased to 2.5–7 mm. The growth inhibition zones of light-pigmented filamentous fungi *Fusarium oxysporum*, *Penicillium variabile,* and *Aspergillus ustus* were 3–6 mm, 2–4 mm, and 1.5–2 mm (Figure 19f,h–j,l–n, respectively). However, when cotton fabric was treated with the control biocidal preparation BC, which had a significantly higher concentration, these same zones were 4–7 mm (Figure 19g).

The described action of the AgNPs/SPH4 nanocomposite, which was applied to pieces of cotton fabric, was assessed as fungistatic. The most sensitive to the treatment was the *Candida albicans* test culture, and the most resistant was the *Aspergillus ustus* culture. It should be emphasized that the fungistatic effect of this nanocomposite, diluted 10 and 100 times, was more pronounced in almost all tests. The results of these experiments confirmed the stable and long-term bactericidal and fungistatic action of the AgNPs/SPH4 composite applied to cotton fabric in a very wide range of concentrations.

An important aspect of using biocidal preparations for impregnating dressings is their interaction with open wounds and the possible impact on the rate of wound healing. To study the ability of the AgNPs/SPH4 composite to heal wounds, 4 groups of rats with 10 individuals in each were used. The skin of 10 × 10 mm in size was removed from the back of each rat, and the resulting wounds were treated with equal volumes of various preparations [149]. The AgNPs/SPH4 composite (C_{AgNPs} = 1.2 × 10^{-2} kg·m^{-3}) was used in the 4th group of rats, and the commercial preparation Carbopol, which promotes wound healing, and an aqueous

solution of eumelanin (C_{EM} = 1 kg·m^{-3}) produced by the black yeast *Pseudonadsoniella brunnea* were used in the 2nd and 3rd groups of animals, respectively. EM preparation increased the body's defenses and accelerated wound healing. The exception was the 1st control group, in which wound healing occurred naturally without any treatment. The wound area in rats was monitored at different time intervals.

The changes in wound area over time are shown in Figure 20. These data were discussed from different points of view. When comparing the total number of days during which complete wound healing occurred, the best result (~19 days) was observed in the 3rd group of rats, which were treated with the EM solution. This time was 4 days shorter compared to the time of complete wound healing in the 1st control group of animals. The time of complete wound healing in the 2nd and 4th groups of rats using the Carbopol preparation and the AgNPs/SPH4 composite was approximately the same (~25 days) and was longer than in the 1st control group (~22 days). However, when comparing the wound healing processes with different preparations, the picture was different. Indeed, the most pronounced effect of EM on open wounds was observed in rats of the 3rd group (Figure 20, curve 3), since this preparation caused the strongest additional inflammation of wounds in rats during the first 3 days.

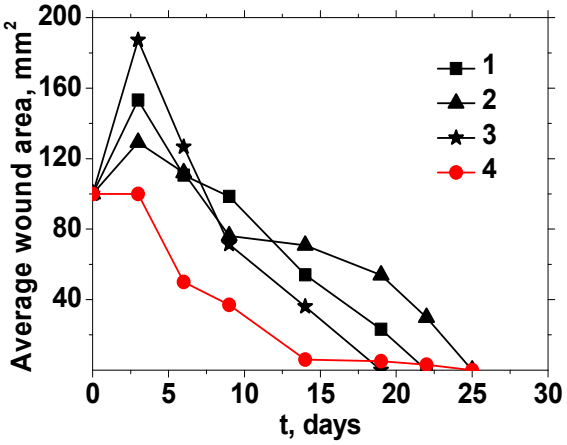

Figure 20. Reduction of the average wound area in rats under the influence of various drugs. Control—*1*, Carbopol—*2*, EM—*3* and AgNPs/SPH4 nanocomposite—*4*. C_{EM} = 1 kg·m^{-3}, C_{AgNPs} = 1.2 × 10^{-2} kg·m^{-3}, T = 22 °C.

This effect led to a 2-fold increase in the wound area, which was even 1.2 times higher than the inflammation of wounds in rats of the 1st control group. The preparation Carbopol caused weak inflammation of wounds in rats of the 2nd group (Figure 20, curve 2), expressed in an increase in the average wound area by 29% during the first 3 days. On the contrary, the AgNPs/SPH4 composite in rats of the 4th group turned out to be the most tolerant to open wounds. The composite did not cause inflammation of the wounds during the first 3 days and promoted their rapid healing during the following 11 days (Figure 20, curve 4). Due to this, the condition of wounds treated with the AgNPs/SPH4 composite on the 14th day was the best (S = 6 ± 1 mm^2) compared to wounds treated with EM and Carbopol (S = 36 ± 3 and 71 ± 3 mm^2, respectively) or not treated at all (S = 54 ± 1 mm^2).

Another important aspect was the effectiveness of the drug, determined by the concentration of the active substance in the solution. In this regard, the AgNPs/SPH4 nanocomposite was more effective in wound healing than the EM solution, since it contained a significantly lower concentration of active AgNPs (more than 83 times) compared to the EM solution. Thus, the developed nanocomposite demonstrated high effectiveness in wound healing. Its advantages over other studied drugs were the absence of additional wound inflammation during the first 3 days, a more rapid and reliable healing effect, and a very low concentration of active silver nanoparticles.

Current results on wound healing by AgNPs are contradictory. Thus, in the study [170], a significant reduction in healing time and an increase in bacterial clearance of infected wounds occurred with the use

of AgNP-impregnated wound dressings compared to silver sulfadiazine solution. At the same time, AgNP-filled wound dressings increased the healing time of superficial burn wounds, but showed no difference in the healing of deep burn wounds compared to silver sulfadiazine [171]. Currently, biological mechanisms of healing of various wounds and the influence of individual AgNPs and nanoparticles introduced into dressings on these processes are actively studied and discussed in the literature [172–175].

As is known, the healing of several wound types is a complex and insufficiently studied phenomenon that includes three main phases: inflammatory, proliferative, and remodeling [172,173]. Inflammation usually begins in the first minutes after skin damage, simultaneously with hemostasis. The first response to inflammation is by white blood cells (neutrophils) that migrate through the endothelium of local blood vessels to the wound. The next response involves monocytes infiltrating the tissue and differentiating into macrophages. These macrophages secrete cytokines that initiate inflammation, leading to an increase in the number of immune cells at the site of infection. The next 4 to 15 days are considered the proliferative stage, during which initial repair of both the epidermis and dermal layers of the skin occurs. The final maturation stage (6 to 12 months), involving further remodeling of granulation tissue and the synthesis of structural proteins such as collagen, occurs when the wound is completely healed.

According to current knowledge, AgNPs can evoke a complex response in skin cells, including the promotion of keratinocyte proliferation and migration, the differentiation of fibroblasts into myofibroblasts, suppression of proinflammatory cytokines (IL-6, IL-12, TNF-α), and a bactericidal effect [176]. Bacteria produce endotoxins that, in turn, promote inflammation; thus, the anti-inflammatory action of silver may partly result from its bactericidal activity. AgNPs can also be used as anti-biofilm and anti-quorum-sensing agents against multidrug-resistant bacteria [177].

It is well known that *S. aureus* and *P. aeruginosa* are the most common antibiotic-resistant pathogens in post-surgical wound infections. As we have shown, Ag/SiO_2-PAAm nanocomposites were highly effective against these bacterial species. Notably, the antibacterial and anti-inflammatory effects of Ag/SiO_2-PAAm are consistent with the observed reduction in wound area compared with the control during the initial inflammatory stage of healing, which distinguishes this AgNP preparation from the other treatments used in this study (Figure 20).

Carbopol is a high-molecular-weight polyacrylic acid preparation used to facilitate wound healing. As our results showed, the Ag/SiO_2-polyacrylamide nanocomposite was more effective than carbopol in reducing wound area and shortening the healing process. Eumelanin is considered a promising wound-healing agent because of its pronounced antioxidant effects [178]. However, in our study, eumelanin markedly increased the wound area during the inflammatory stage (Figure 20), although it shortened the overall duration of wound healing. Thus, the combined antibacterial and anti-inflammatory effects of AgNPs may make this system preferable to treatment with carbopol or eumelanin alone. At the same time, the combined application of AgNPs with these preparations may also be promising and warrants detailed future investigation. Currently, only the main known benefits of using AgNPs in wound healing can be highlighted, such as broad antimicrobial activity, anti-inflammatory effect, least bacterial resistance, stimulation of angiogenesis and tissue regeneration, as well as modulation of signaling pathways associated with wound healing [172–175].

Based on the results obtained, a conclusion was drawn about the high potential of AgNPs/SPH composites for the treatment and long-term disinfection of not only wound dressings and hygienic materials such as bandages, napkins, and plasters, but also cotton fabrics, underwear, and other clothing. In addition, the urgent problem of ensuring the durability of embedded metal nanoparticles can be easily solved by short-term heating of fabrics or finished products treated with nanocomposites. The basis for this is the effect of easy cross-linking of PAAm chains at elevated temperatures during short-term heating (20 min at 95 °C and then 10 min at 135 °C), which was previously revealed in a study of the effect of temperature on thin films of pure PAAm and grafted copolymers of poly(vinyl alcohol)/polyacrylamide [179]. A promising

alternative to the impregnation procedure can also be considered the treatment of fabric or finished products with a nanocomposite spray due to its low viscosity.

11. Silver/Hybrid Nanocomposites in Fish Farming

The prospects of using one of the developed nanocomposites, AgNPs/SPH4, as an antibacterial agent in fish farming were assessed primarily by studying its antibacterial activity against two typical bacterial pathogens of the genera *Aeromonas* and *Pseudomonas* in Ukrainian fish ponds [105]. *Aeromonas hydrophila* is an oxidase-positive, glucose-fermenting, gram-negative aquatic bacterium that inhabits aquatic environments and exhibits resistance to common antibiotics such as penicillin, ampicillin, ticarcillin, and carbenicillin [180]. *Pseudomonas* (sp.) is a nonspore-forming gram-negative bacterium that can cause fish rotting in large quantities and is resistant to streptomycin, ampicillin, penicillin, etracycline, oxytetracycline, and chloramphenicol [181,182]. The antibacterial activity of the composite against the control cultures of *Aeromonas hydrophila* (strain 0433/1) isolated from trout and *Pseudomonas* sp. (strain 0649) isolated from white carp was studied by determining the minimum bactericidal concentration (MBC) and the minimum inhibitory concentration (MIC) using serial dilutions in a liquid nutrient medium (broth). The concentrations of the components in the initial composite were C_{SPH} = 1 kg·m^{-3}, C_{AgNPs} = 1.2 × 10^{-2} kg·m^{-3}. A series of dilutions was prepared in test tubes so that each subsequent C_{AgNPs} was 10 times less than the previous one. Then 0.2 cm^3 of a certain microbial culture was added to each test tube until the density of microorganisms reached 2 × 10^5 CFU cm^{-3}. The tubes were incubated at 37 °C, and changes in solution turbidity were recorded after 24, 48, and 96 h.

According to the obtained data, the AgNPs/SPH4 composite exhibited bactericidal (killing) and bacteriostatic (inhibitory) action against both types of bacteria [105]. At the same time, *Aeromonas hydrophila* bacteria were more sensitive to the composite than *Pseudomonas* sp. bacteria, which was reflected in different values of minimum bactericidal and inhibitory concentrations after 48 h: MBC ≈ 1.2 × 10^{-5} and MIC ≈ 1.2 × 10^{-6} kg·m^{-3} for *Aeromonas hydrophila* and ≈ 1.2 × 10^{-4} and ≈ 1.2 × 10^{-5} kg·m^{-3} for *Pseudomonas* sp. However, after 96 h in solutions with a dilution of 1:1000 (MBC ≈ 1.2 × 10^{-4} and MIC ≈ 1.2 × 10^{-5} kg·m^{-3}), only a bacteriostatic effect of the composition was observed. Thus, the bactericidal and bacteriostatic effects of AgNPs in the composite with SPH4 were preserved to very low concentrations of nanoparticles.

The antibacterial activity of the AgNPs/SPH4 composite was compared with similar results from other studies. As shown in [180], AgNPs with an average size of 21 nm, synthesized in water in the presence of polyvinylpyrrolidone as a stabilizer, completely prevented the growth of *Aeromonas hydrophila* bacteria (with C = 5 × 10^5 CFU cm^{-3}) at a minimum concentration of C_{min} = 1.7 × 10^{-2} kg·m^{-3}. Commercial ZnO nanoparticles with a size of 66 nm prevented the growth of these bacteria under similar conditions at C_{min} = 1.575 × 10^{-2} kg·m^{-3} [183]. In another study [184], the MBC and MIC values for 5–6 nm CuO nanoparticles in experiments with *Aeromonas hydrophila* (at C = 1.5 × 10^8 CFU cm^{-3}) were 3.0 × 10^{-1} and 8.0 × 10^{-2} kg·m^{-3}, respectively. In comparison with these examples, the developed AgNPs/SPH4 nanocomposite showed a very high antibacterial effect against the studied fish pathogens. From this point of view, it can be considered an effective bactericidal/bacteriostatic agent for disinfecting aquariums/fish nurseries.

To characterize further the effect of AgNPs/SPH4 nanocomposite on the growth of *Aeromonas hydrophila*, standard agar nutrient medium and disk method were used [105]. Here, information on the antibacterial activity of the composite was obtained in comparison with metal citrates of Zn, Cu, Ag, Mn, Mg and Fe having the same concentration in aqueous solution, C_{MeCit} = 1 × 10^{-2} kg·m^{-3} (Figure 21).

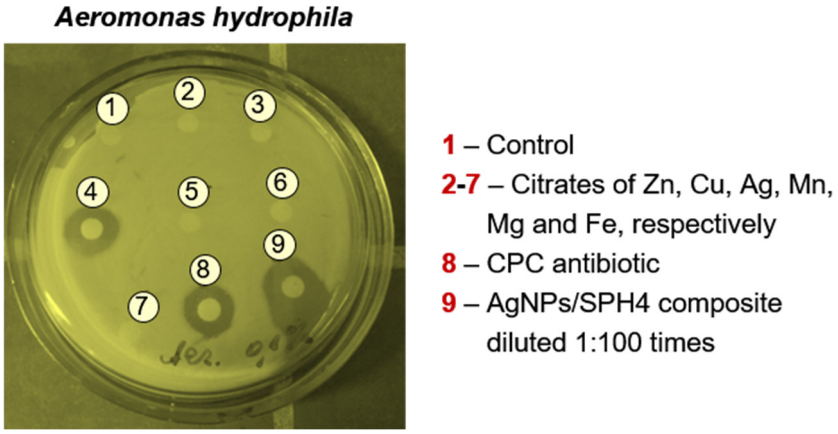

Figure 21. Growth inhibition zones (after 72 h) of *Aeromonas hydrophila* bacteria under the influence of citrates of various metals, the antibiotic CPC, and diluted AgNPs/SPH4 composite. $C_{MeCit} = 1 \times 10^{-2}$ kg·m^{-3}, $C_{CPC} = 8 \times 10^{-3}$ kg·m^{-3}, $C_{AgNPs} = 1.2 \times 10^{-4}$ kg·m^{-3}, $T = 25$ °C.

A clean disk and a disk impregnated with an aqueous solution of the antibiotic chloramphenicol with $C_{CPC} = 8 \times 10^{-3}$ kg·m^{-3} were also used in this experiment. The bacterial density was 2×10^5 CFU cm^{-3}. The most effective, with a growth inhibition zone of 21.3 ± 0.2 mm was the AgNPs/SPH4 composite with $C_{AgNPs} = 1.2 \times 10^{-4}$ kg·m^{-3} (variant 9 in Figure 21). Bactericidal activity of all metal citrates (except silver citrate) was absent in the range of $C_{MeCit} \leq 1 \times 10^{-2}$ kg·m^{-3} (variants 2, 3, 5–7 in Figure 21). Silver citrate with a growth inhibition zone of 16.7 ± 0.2 mm and a significantly higher concentration of silver ions $C_{Ag+} = 6.3 \times 10^{-3}$ kg·m^{-3} showed lower bactericidal activity (variant 4 in Figure 21). However, the least bactericidal effect with a growth inhibition zone of 14.4 ± 0.2 mm was achieved when using the antibiotic CPC (variant 8 in Figure 21). These data once again confirmed the high antibacterial activity of our composite.

The next important part of these studies was to assess the risk of the nanocomposite to non-target species. For this purpose, three separate studies were conducted to determine: (i) the biological risks relative to relevant test organisms such as *Danio rerio*, *Hydra attenuata*, *Daphnia magna,* and *Allium cepa* L., (ii) the toxicity of the composite to *Danio rerio* embryos, and (iii) the genotoxicity of the composite to *Danio rerio* cells [105]. The effect of the composite was assessed mainly by the survival of the test organisms for 96 h.

Test organisms of different trophic levels were used to assess biological risks (Table 7). *Danio rerio* (Hamilton, 1822) was a representative of freshwater fish of the carp family (*Cyprinidae*). *Hydra attenuata* (Pallas, 1766) was a freshwater coelenterate of the class *Hydridae*. *Daphnia magna* (Müller, 1785) was a planktonic crustacean of the class *Franchiopoda* of the daphnia family (*Daphniidae*). *Allium cepa* L. was a perennial plant of the onion family (*Alliaceae*), used as a standard for cytogenetic monitoring of the environment.

Test organisms were maintained in a nutrient medium after adding a composite with concentrations of $C_{AgNPs} = 1.2 \times 10^{-2}$, $2.4 \times 10^{-2,}$ and 6.0×10^{-2} kg·m^{-3}. The results presented in Table 7 revealed different reactions of the animal test organisms to the introduction of the composite. Among them, *Danio rerio* individuals showed the highest survival rates in the used range of C_{AgNPs}. However, based on the entire complex of biological tests, a general range of $C_{AgNPs} < 1.2 \times 10^{-2}$ kg·m^{-3} was determined, in which no lethal consequences for the test organisms were observed. The mass and size parameters of the roots of the plant test organisms also did not decrease in this concentration range. Therefore, this range of AgNPs concentrations in the composite with SPH4 was proposed for disinfection of aquariums/nurseries with fish.

Table 7. State of test organisms under the influence of AgNPs/SPH4 nanocomposite [(1)].

Studied Test Organisms	Survival [% to Control]			
	Control, H_2O	$C_{AgNPs}\cdot10^2$[kg·m^{-3}]		
		1.2	2.4	6.0
Daniorerio	100	100	100	60
Hydraattenuata	100	95	85	40
Daphnia magna	100	100	70	40
	$w_{av}\cdot10^6$ [kg] or $l_{av}\cdot10^3$ [m]/[% to control]			
Alliumcepa L. (av. weight)	3.01/100.0	3.02/100.3	3.19/106.0	2.10/69.8
Alliumcepa L. (av. length)	28.4/100.0	26.7/94.0	24.0/84.5	/78.9

[(1)] $T = 22 \pm 2$ °C.

The toxicity of the composite was characterized using a zebra fish embryo test [105]. It should be noted that both adult and embryonic *Danio rerio* are widely used to study the acute toxicity of various compounds, particularly transition metals, pesticides, and other hazardous environmental pollutants [185–187]. Zebra fish embryos were obtained from adult fish. Fertilized eggs were transferred to 96-well plates and various concentrations of the AgNPs/SPH4 composite were added. The number of embryo deaths within 5, 24, 48, and 72 h assessed the toxic effects. The results of the evaluation of the toxicity of the composition in relation to the embryos are shown in Figure 22. The lowest mortality was observed in the control solution and in the composite with $C_{AgNPs} = 1.2 \times 10^{-2}$ kg·m^{-3}. In the second case, the mortality of the embryos did not exceed 10%, therefore, it was within the normal distribution. Based on these experiments, a conclusion was made about the absence of a toxic effect of the AgNPs/SPH4 composition on the embryogenesis of *Danio rerio* in the range of $C_{AgNPs} < 1.2 \times 10^{-2}$ kg·m^{-3}.

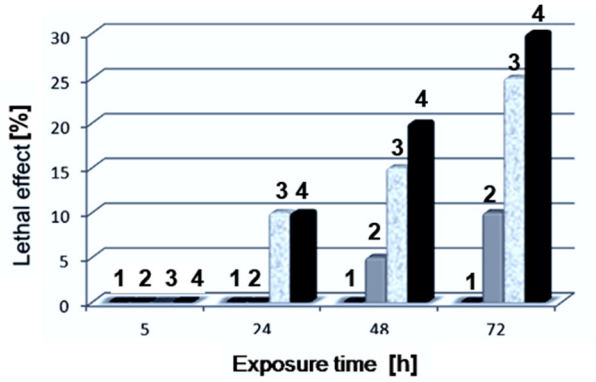

Figure 22. Effect of AgNPs/SPH4 nanocomposite on *Danio rerio* embryos. C_{AgNPs} = 0—*1*, 1.2 × 10^{-2}—*2*, 2.4 × 10^{-2}—*3,* and 6.0 × 10^{-2} kg m^{-3}—*4* ($p < 0.05$).

Considering that the survival of test objects at different C_{AgNP} could not guarantee the absence of sublethal effects and changes at the cellular level, the genotoxicity of the developed composite was also studied based on a micronucleus test on fish blood cells [187,188]. Fish usually respond to toxic substances by forming micronuclei due to chromosome fragmentation induced by viral infections, ionizing radiation, and various mutagens [189]. Therefore, defects in blood nuclei, the percentage of double cells, and apoptosis are recorded [190]. The criteria for the content of micronuclei in cells and the quantitative characteristics of nucleoli are used.

The genotoxicity of the AgNPs/SPH4 nanocomposite was determined using a micronucleus test on *Danio rerio* blood cells [105]. Cells were collected from groups of 10 fish, placed in water with standard hydrochemical parameters (Control group) or in the same water contaminated with various C_{AgNPs}

(Experimental groups), and kept there for 96 h. The results of the analysis of cytological preparations are presented in Figure 23 and Table 8.

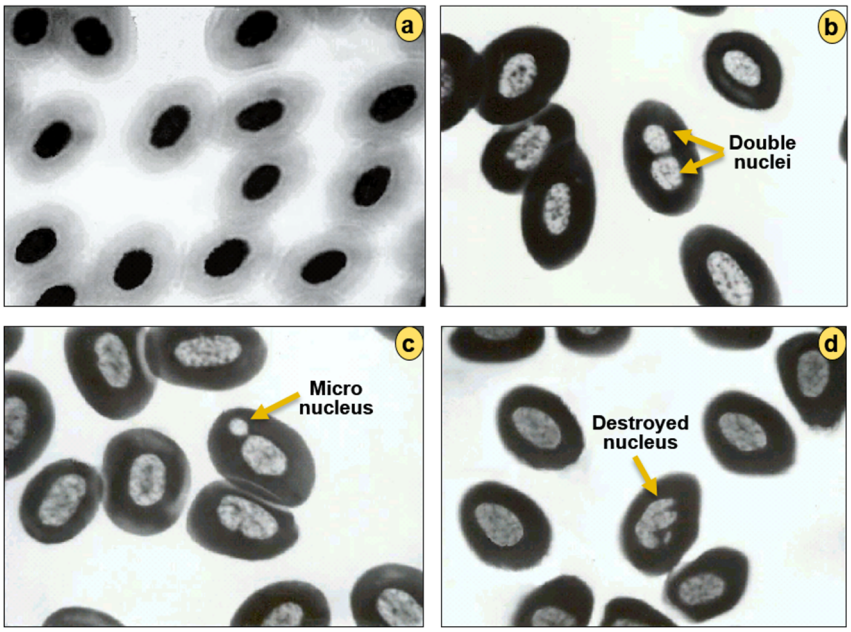

Figure 23. Results of micronuclear tests on *Danio rerio* blood cells. (**a**) The original cells (control) and (**b**–**d**) cells treated with an AgNPs/SPH4 nanocomposite, which contained (**b**) double nuclei, (**c**) micronuclei and (**d**) destroyed nuclei. $C_{AgNPs} = 6 \times 10^{-2}$ kg·m^{-3}.

Table 8. Genotoxicity of AgNPs/SPH4 nanocomposite.

Type of Cell Modification	Number of Modified Cells [% to Control], n = 3000			
	Control, H_2O	$C_{AgNPs}\cdot 10^2$, kg·m^{-3}		
		1.2	2.4	6.0
Micro nuclei	0	0	0.67	1.67
Double nuclei	0	0	0.33	1.33

Significant changes in the blood cells of the experimental fish groups compared to the control were detected only at the maximum value of $C_{AgNPs} = 6 \times 10^{-2}$ kg·m^{-3}. In this case, it was possible to observe the appearance of a large number of double nuclei, micronuclei, and even destroyed nuclei in the blood cells of *Danio rerio* (Figure 23b–d, Table 8). Minor disturbances in the fish cells were also detected at $C_{AgNPs} = 2.4 \times 10^{-2}$ kg·m^{-3}, but in the range of $C_{AgNPs} \leq 1.2 \times 10^{-2}$ kg·m^{-3}, the genotoxicity of the AgNPs/SPH4 composite was completely absent.

Thus, the AgNPs/SPH4 composite demonstrated pronounced bactericidal and bacteriostatic effects against fish pathogenic bacteria *Aeromonas hydrophila* and *Pseudomonas* sp., which were maintained at very low concentrations of metal nanoparticles. Experiments with a series of model animal test organisms allowed us to determine the overall safe range of silver nanoparticle concentrations ($C_{AgNPs} < 1.2 \times 10^{-2}$ kg·m^{-3}), at which virtually no lethal effects were observed for the animal test organisms, and no decrease in the root mass/size in the plant organism was observed. Based on the obtained results and special studies of the composite's toxicity to *Danio rerio* embryos and its genotoxicity to *Danio rerio* cells, the developed composition can be successfully used as an antibacterial agent in fish farming in the found concentration range without any biological risks, even at the cellular level.

12. Biological Impact of Hybrid-Stabilized Silver Nanoparticles in Wheat Cultivation

One of the most interesting but unfortunately unfinished tests of the biological activity of AgNPs/SPH nanocomposites was the study of their effects on the growth and yield of agricultural crops, particularly winter wheat. In this direction, a single experiment was conducted on the treatment of winter wheat seeds with our AgNPs/SPH4 composite and subsequent cultivation of wheat plants in the field from the treated seeds [105]. According to the developed method, winter wheat seeds of the Arctis variety were treated with aqueous dispersions of AgNPs/SPH4 after *in situ* synthesis and purification of the composite and immediately before sowing. For this purpose, two dispersions were prepared: the original composite (1:1) with C_{SPH} = 2 kg·m^{-3} and C_{AgNPs} = 1.2 × 10^{-2} kg·m^{-3} and a 10-fold dilution (1:10). Using 250 cm^3 of each dispersion, two portions of 50 kg of winter wheat seeds were treated. Each batch of treated seeds was planted and grown on 0.4 acres of the Kernel Research Center field, near Kyiv, Ukraine, in 2018. For comparison, two plots of the same field, each 0.4 acre, were sown with untreated winter wheat seeds. The field with all areas marked is shown in Figure 24.

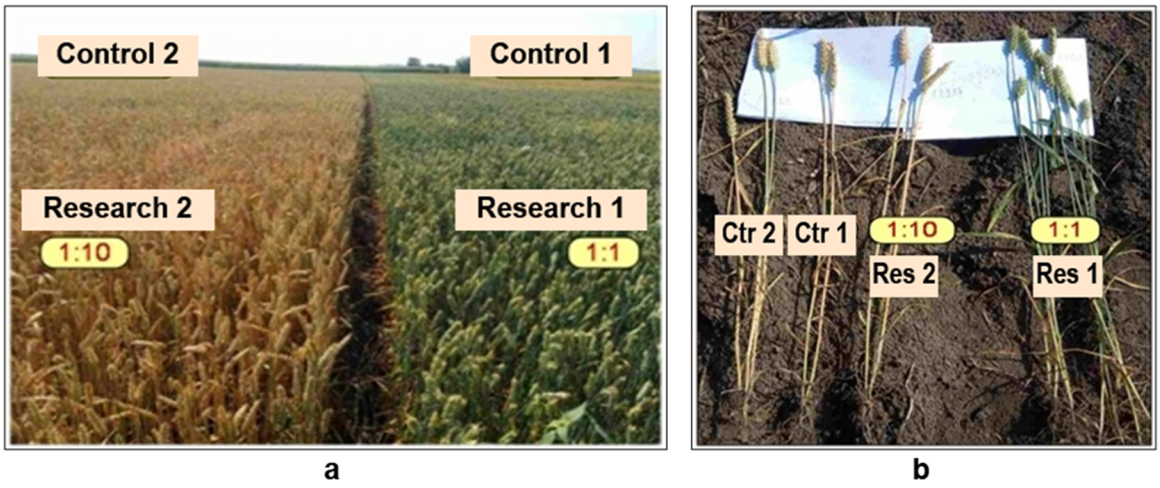

Figure 24. Photographs of (**a**) two experimental (Research 1–2) and comparative (Control 1–2) plots of a winter wheat field and (**b**) several individual plants from these plots.

As a result of the experiments, a significant difference in the color of plants was established: yellow versus green, grown from untreated seeds or treated with a diluted composite 1:10 (areas "Control 1", "Control 2" and the left near area in Figure 24a) and seeds treated with the original nanocomposite 1:1 (the right near area in Figure 24a). At the same time, we did not observe a noticeable effect of the composite on the rate and degree of seed germination, as well as the length of plant stems, while the size of the spikelets in plants grown from seeds treated with an undiluted composite was somewhat smaller (Figure 24b). The observed significant differences indicated an increase in the vegetation period of winter wheat plants under the influence of a composite with a higher concentration of AgNPs. This was especially evident in the very dry summer of 2018. However, further research was required to establish the causes of this phenomenon and its impact on the winter wheat yield.

By now, significant experimental material has already been accumulated in this area, allowing us to understand the main directions of the influence of AgNP on the growth and development of various agricultural plants, including wheat [191–201]. Positive effects include increased seed germination, plant growth, and wheat yield, but only at strictly selected concentrations [191,193,194,199,200]. The use of AgNPs can alleviate stress conditions for crops such as drought [200,201], frost [198,200], salinity [191,194], and the presence of heavy metals in soil [193,197]. They can also control wheat pathogens due

to their bactericidal, antifungal, and antiviral properties [190,191,197] and even promote positive shifts in soil microbiota [192].

The most negative factor when using AgNPs is the high dose of nanoparticles, which initiates the occurrence of various negative consequences, which are additionally size-dependent [194,200]. High doses of AgNPs can reduce seed germination and growth, and affect the length and weight of roots and shoots. These nanoparticles can accumulate in leaves and roots, thereby activating defense mechanisms at the cellular and tissue levels and altering antioxidant activity and metabolism. Under the influence of high concentrations of AgNPs, various botanical changes can be observed in plants, such as the formation of active oxygen species, chlorophyll content, superoxide dismutase activity, an increase in the level of H_2O_2, as well as the content of glutathione, carotenoids, ascorbate, and proline [194]. This leads to suppression of photosynthesis, the appearance of irregular morphological changes, and other consequences.

Using the above information, we can explain the results of our experiments, presented in Figure 24. It is obvious that the treatment of winter wheat seeds before sowing with the AgNPs/SPH4 composite with a concentration of C_{AgNPs} = 1.2 × 10^{-2} kg·m^{-3} had a beneficial protective effect on the growth and development of wheat plants under hot and dry conditions of 2018, although it extended the seed maturation period. This shows the potential for further research in this area, especially since the topic of using polymer and hybrid carriers of silver nanoparticles in crop cultivation technologies remains virtually unexplored.

13. Promising Nanobiotechnology Based on Silver/Hybrid Nanocomposites in Poultry Farming

The objectives of this part of the research were to study the effect of one of our nanocomposites, AgNPs/SPH6 (Tables 2 and 5), containing very small silver nanoparticles (dav = 2.4 ± 1.0 nm; Figure 12), on laying hens and their eggs when administered orally [161,202,203]. The main focus was on the accumulation of AgNPs in different parts of the chicken eggs, due to the lack of such information in the literature. However, an important aspect of the influence of the composite on the morphological and biochemical parameters of the blood and blood serum of laying hens was also monitored. We used the oral method of introducing the nanocomposite to hens (through drinking water) as one of the most effective and acceptable, which involves its passage through the mucous membrane of the digestive system, blood, and liver, and provides a systemic effect on the body. Considering that the toxicity of AgNPs was lower at a lower dose and non-daily introduction of the composite, a special research methodology was developed.

For the experiments, 45 High Line W36 laying hens aged 38 weeks were selected and divided into 3 groups (n = 15)—Control and Research 1–2. The hens in the Research groups additionally received AgNPs/SPH6 dispersion in drinking water 3 times a month, with 10-day intervals. In Research groups 1 and 2, two concentrations of C_{AgNPs}, 1.0 × 10−3 and 2.0 × 10−3 kg·m−3, were used. They were obtained by diluting the initial composite with C_{AgNPs} = 2.4 × 10^{-2} kg·m^{-3} and C_{SPH} = 1 kg·m^{-3} (Figure 12) and corresponded to nanosilver doses of 0.2 and 0.4 mg·m^{-3} per day, respectively. On the 10th, 20th, and 30th days of the experiment, 5 fresh eggs and blood from 5 hens of each group were collected for analysis. The content of various metals (Ag, Cu, Zn, Fe, and Pb) in the shell, protein, and yolk of eggs, as well as the main morphological and biochemical indices of blood and blood serum of hens of the Control and Research 1–2 groups, were determined using plasma-optical emission spectrometry and methods of biochemical analysis [202,203].

Throughout the experiment, the behavior of the hens, their feed, and water consumption did not change. The survival rate of the hens in all groups was 100%, and their egg productivity did not differ between the groups. In addition, feeding them the nanocomposite dispersion three times at both doses did not affect the morphological parameters of the hens' eggs: the weight of the eggs and their components (whites, yolks, and shells) was preserved. With single, double, and triple administration of the AgNPs/SPH6 composite to laying hens at doses of 0.2 and 0.4 mg·hen^{-1} per day, the number of erythrocytes, leukocytes and their subpopulations in the blood of hens did not change. Only a slight decrease in hematocrit was observed with

a single use of the composite compared to the control group [203]. Thus, this drug can be considered biocompatible and safe for blood cells. Obviously, this is due to the good transport properties and small sizes of the hydrophilic SPH carriers used to obtain and deliver AgNPs.

The most striking results were obtained concerning the accumulation of metals, primarily silver, in different parts of chicken eggs [161,202]. So, a single administration of drinking water with AgNPs doses of 0.2 and 0.4 mg·head^{-1} per day to laying hens of groups Research 1 and Research 2 led to a relatively small (by 33.3%) accumulation of silver in the eggshell (Table 9). However, the content of Zn, Fe and Pb did not change within the error limits. An exception is the increase in the Cu content by 80.0%, but only at a higher dose of AgNPs. After the composite solution was administered to laying hens twice, the silver content in the eggshells of both groups, Research 1–2, increased significantly (by 9.0 and 11.4 times on average) compared to the Control group. However, this did not affect the content of Cu, Zn, Fe, and Pb in the shells (Table 9). After the composite was administered to laying hens three times with drinking water, the amount of silver accumulated in the eggshells decreased slightly: the silver content in the Research 1 and 2 groups exceeded that of the Control group by only 6.3 and 10.0 times, respectively.

Table 9. Accumulation of metals in the shell of chicken eggs.

Me	Period	Metal Content [mg·kg^{-1}] ($x \pm SD$, $n = 5$)		
		Groups of Laying Hens		
		Control	Research 1	Research 2
Ag	After 10 days	0.006 ± 0.002	0.008 ± 0.001	0.008 ± 0.001
Cu		0.5 ± 0.1	0.5 ± 0.1	0.9 ± 0.1
Zn		2.0 ± 0.2	1.5 ± 0.6	2.8 ± 0.9
Fe		0.6 ± 0.3	0.5 ± 0.2	0.6 ± 0.2
Pb		0.009 ± 0.004	0.004 ± 0.001	0.008 ± 0.004
Ag	After 20 days	0.007 ± 0.004	0.063 ± 0.020	0.080 ± 0.006
Cu		2.7 ± 0.9	0.8 ± 0.2	1.1 ± 0.4
Zn		3.0 ± 1.0	2.0 ± 0.2	3.0 ± 2.0
Fe		0.5 ± 0.2	0.7 ± 0.1	0.9 ± 0.2
Pb		0.024 ± 0.009	0.007 ± 0.001	0.010 ± 0.002
Ag	After 30 days	0.006 ± 0.006	0.038 ± 0.007	0.060 ± 0.020
Cu		0.7 ± 0.2	0.6 ± 0.2	0.6 ± 0.2
Zn		2.3 ± 0.5	1.1 ± 0.3	2.5 ± 0.9
Fe		0.2 ± 0.1	0.17 ± 0.03	0.1 ± 0.1
Pb		0.006 ± 0.002	0.005 ± 0.001	0.006 ± 0.001

The data in Table 10 reflect the accumulation of silver in egg white. A single feeding of different doses of AgNPs to hens of Research 1–2 groups resulted in only a slight increase in the silver content in egg white (by 33.3 and 16.7%, respectively) compared to the Control group. After two-fold exposure of hens to the AgNPs/SPH6 composite, an increase in the silver content in egg white (by 50%) was observed only in the Research 2 group, where the hens received a higher dose of nanosilver (Table 10). However, the strongest accumulation of silver in the egg white of both Research groups compared to the Control group (on average 2.2 times) occurred 10 days after the third feeding of the hens with the nanosilver composite (Table 10). The amount of the other indicated metals in the protein remained virtually unchanged.

Silver accumulation in egg yolk was different. The greatest increase in silver in the yolk of the Research 1–2 groups compared to the Control group (on average 5.7 times) occurred on the 10th day of the experiment (Table 11).

Table 10. Accumulation of metals in the protein of chicken eggs.

Me	Period	Metal Content [mg·kg^{-1}] ($x \pm SD$, $n = 5$)		
		Groups of Laying Hens		
		Control	Research 1	Research 2
Ag	After 10 days	0.0006 ± 0.0001	0.0008 ± 0.0001	0.0007 ± 0.0001
Cu		0.30 ± 0.10	0.28 ± 0.08	0.30 ± 0.05
Zn		0.0020 ± 0.0010	0.0018 ± 0.0004	0.0020 ± 0.0003
Fe		0.027 ± 0.004	0.030 ± 0.007	0.030 ± 0.008
Pb		0.033 ± 0.003	0.049 ± 0.004	0.061 ± 0.005
Ag	After 20 days	0.0006 ± 0.0001	0.0006 ± 0.0003	0.0009 ± 0.0002
Cu		0.15 ± 0.01	0.21 ± 0.07	0.19 ± 0.02
Zn		0.0020 ± 0.0003	0.0017 ± 0.0004	0.0019 ± 0.0001
Fe		0.010 ± 0.010	0.014 ± 0.009	0.010 ± 0.002
Pb		0.040 ± 0.010	0.039 ± 0.008	0.036 ± 0.003
Ag	After 30 days	0.0005 ± 0.0001	0.0011 ± 0.0001	0.0011 ± 0.0001
Cu		0.30 ± 0.10	0.30 ± 0.10	0.20 ± 0.07
Zn		0.0020 ± 0.0001	0.0017 ± 0.0004	0.0021 ± 0.0002
Fe		0.025 ± 0.002	0.030 ± 0.003	0.030 ± 0.010
Pb		0.088 ± 0.008	0.083 ± 0.004	0.093 ± 0.003

On the 20th day after the second administration, such a level of silver was retained only in the yolk of eggs of group Research 2, whose hens received 0.4 mg of nanosilver per hen per day. In Research 1 group, with a nanosilver dose of 0.2 mg·hen^{-1} per day, the increase in silver content in the yolk was less significant: only 1.4 times compared to the Control group. On the 30th day after the third treatment of laying hens with the composite, the silver content in the yolk of the eggs of the Research 1 group remained virtually unchanged (Table 11), it was 1.8 times higher than in the Control group. However, in the Research 2 group, the silver content decreased compared to the data obtained on the 10th and 20th days of the experiment, exceeding the Control group indicator by only 2.2 times (Table 11). The content of other metals in the yolk of the eggs of the experimental groups remained virtually unchanged.

The accumulation of silver in different parts of eggs after oral administration of the composite to laying hens proved the fact of AgNP penetration into the chicken bloodstream. This occurred by passing the composite through the digestive tract and absorption through the intestinal epithelium, as well as further transport into the chicken tissues, including the oviduct, where the formation of egg white and shell occurred. The latter conclusion was made on the basis of our special studies of the stability of the AgNPs/SPH6 composite under various conditions that exist in living organisms (Section 8) [161].

This composite turned out to be completely stable in "physiological solution" (at $C_{NaCl} = 9.0$ kg·m^{-3}), at pH = 9 and when diluted. At pH = 2, AgNPs began to dissolve gradually, but the rate of this process was relatively low, so that it did not end even after 1.5 h (Figure 14c,d). This meant that the composite could successfully "pass" the stomach (ventricle and stomach) of laying hens without significant damage to the AgNPs. Indeed, the pH in the stomach of hens is ≈3–4, and the evacuation time of the stomach contents is ≈40–45 min [204,205]. The known properties of SiO_2 and PAAm determined the chemical resistance of the SPH carriers themselves to these conditions. In particular, silica nanoparticles could slowly dissolve in water at low temperatures only at high pH values [110]. In addition, PAAm chains could hydrolyze in acidic and alkaline environments, but the rate of this process at low temperatures was insignificant [143].

Table 11. Accumulation of metals in the yolk of chicken eggs.

Me	Period	Metal Content [mg·kg^{-1}] ($x \pm SD$, $n = 5$)		
		Groups of Laying Hens		
		Control	Research 1	Research 2
Ag	After 10 days	0.0007 ± 0.0001	0.0040 ± 0.0020	0.0040 ± 0.0040
Cu		1.4 ± 0.1	0.9 ± 0.4	1.0 ± 0.3
Zn		22 ± 8	20 ± 8	19 ± 5
Fe		27 ± 8	35 ± 10	23 ± 10
Pb		0.035 ± 0.020	0.053 ± 0.030	0.025 ± 0.010
Ag	After 20 days	0.0007 ± 0.0001	0.0010 ± 0.0001	0.0040 ± 0.0001
Cu		1.6 ± 0.1	1.4 ± 0.5	1.2 ± 0.5
Zn		29 ± 3	26 ± 10	26 ± 10
Fe		45 ± 4	39 ± 20	40 ± 20
Pb		0.013 ± 0.004	0.020 ± 0.020	0.017 ± 0.003
Ag	After 30 days	0.0006 ± 0.0001	0.0011 ± 0.0002	0.0013 ± 0.0001
Cu		1.4 ± 0.4	1.6 ± 0.3	1.2 ± 0.5
Zn		26 ± 10	28 ± 5	17 ± 6
Fe		38 ± 20	41 ± 10	29 ± 10
Pb		0.029 ± 0.010	0.047 ± 0.009	0.030 ± 0.002

The second surprising fact was revealed during the analysis of changes in the distribution of silver among different parts of the eggs after single, double, and triple treatments of laying hens with the composite (Table 12).

Table 12. Accumulation of silver in various parts of eggs.

Groups of Hens	Period [Days]	Silver Content [%]		
		Parts of Eggs		
		Eggshell	Protein	Yolk
Control	10	82.2	8.2	9.6
	20	84.3	7.2	8.4
	30	84.5	7.0	8.5
Research 1	10	62.5	6.25	31.25
	20	97.5	0.9	1.5
	30	94.6	2.7	2.7
Research 2	10	63.0	5.5	31.5
	20	94.2	1.1	4.7
	30	96.2	1.7	2.1

It consisted of the predominant accumulation of silver in the eggshell of both Research 1–2 groups, starting with the second dose of the composite (on the 20th day of the experiment) [161]. The effect of silver accumulation mainly in the shell was accompanied by a sharp decrease in the silver content in the protein and yolk, which are in the edible part of the eggs (Table 12). In this regard, the difference in the data on the distribution of silver between different parts of the eggs on the 10th day after the first dose was attributed to the primary reaction of the hens' organisms to the introduction of the new substance. After the second and third doses, the organisms adapted to external influences.

Selective endogenous accumulation of silver in the eggshells of laying hens may be of great practical importance due to its broad antimicrobial activity, which will significantly extend the shelf life of chicken eggs without deteriorating their sanitary and hygienic properties. This assumption is supported by the results of other authors who carried out exogenous treatment of bird eggshells with nanosilver [206–209]. The insignificant total intake of silver into the protein and yolk of eggs after three-fold oral administration

of the composite to hens was 2.2 and 2.6 μg·kg^{-1} (at doses of 0.2 and 0.4 mg·hen^{-1}, respectively). Thus, there was no toxic threat to laying hens and consumers of their eggs. Indeed, the average silver consumption by modern humans is approximately 5–8 μg·day^{-1}, while the recommended essential or vital dose per day is 50–100 μg (World Health Organization, 2008). Therefore, even with daily consumption of 10 eggs from hens treated two or three times according to our method, the human body will receive a significantly smaller dose of silver than recommended per day.

The corresponding results on the effects of AgNPs/SPH6 administration in laying hens on the biochemical parameters of their blood serum were discussed in detail in [161,203]. They are also partially presented in Table 13.

Table 13. Parameters of blood serum of laying hens after 30 days.

Biochemical Parameters	Value (x ± SD, n = 5)		
	Groups of Laying Hens		
	Control	Research 1	Research 2
Total protein [g·dm^{-3}]	44 ± 3	46 ± 4	59 ± 3
Albumin [g·dm^{-3}]	7.2 ± 0.5	7.1 ± 0.4	6.8 ± 0.6
Cholesterol [g·dm^{-3}]	1.9 ± 0.3	2.2 ± 0.1	1.3 ± 0.1
Creatinine [μmol·dm^{-3}]	70 ± 6	76 ± 3	64 ± 4
Glucose [mmol·dm^{-3}]	9.9 ± 1.0	11.9 ± 0.5	8.7 ± 0.7
ALT [U·dm^{-3}]	12 ± 2	14 ± 1	11 ± 1
AST [U·dm^{-3}]	130 ± 20	109 ± 8	140 ± 10
ALP [U·dm^{-3}]	190 ± 20	205 ± 5	190 ± 20
GGT [U·dm^{-3}]	5.8 ± 0.9	6.5 ± 0.5	3.7 ± 0.5
Ca [mmol·dm^{-3}]	2.8 ± 0.5	3.2 ± 0.4	3.0 ± 0.2
P [mmol·dm^{-3}]	1.8 ± 0.5	1.2 ± 0.1	2.3 ± 0.3
K [mmol·dm^{-3}]	4.4 ± 0.3	5.2 ± 0.2	4.3 ± 0.4
Mg [mmol·dm^{-3}]	1.0 ± 0.2	1.0 ± 0.1	1.1 ± 0.2

As can be seen, the content of total protein and albumin in the blood serum of hens of Research 1 group did not change after three-fold administration of the composite to laying hens at a dose of 0.2 mg·hen^{-1}. This indicated the preservation of good liver function in hens. The albumin content did not change in the blood serum of hens of Research 2 group, which were administered the composite three times at a dose of 0.4 mg·hen^{-1}, and the total protein index even increased (Table 13), which was a positive result. The creatinine content in the blood serum of hens in Research 1–2 groups remained at the level of the Control group (Table 13), indicating normal kidney function in hens. However, the potassium content increased slightly (by 18.2%) only in the blood serum of hens in Research 1 group. After three-fold exposure to the composite, no serious and systemic changes in the activity of enzymes such as ALT, AST, ALP, and GGT, characterizing the state of the liver and other vital organs of laying hens, were observed (Table 13). The glucose and cholesterol levels in the blood serum of hens in Research 1–2 groups, which are indicators of carbohydrate and lipid metabolism, also changed little compared to the Control group (Table 13). Mineral metabolism in the blood serum of laying hens was reflected in the content of total calcium, inorganic phosphorus, potassium, and magnesium. For the Research 2 group, whose hens received a higher dose of the composite three times, both indicators remained at the level of the Control group within the error limits. However, in the blood serum of the Research 1 group, a slight increase in calcium (by 14.3%), a decrease in phosphorus (by 33.3%), and an increase in potassium were observed compared to the Control group (Table 13). It should be noted that a lower dose of AgNPs in SPH carriers had a greater effect on mineral metabolism in the body of laying hens.

Our research results indicate a low cumulative capacity of silver nanoparticles in laying hens' products, particularly in eggs. This points to its possible excretion in feces in the first few days after ingestion. This is consistent with the results of a study [209], where an experiment on laboratory mice showed that after taking silver at doses of 0.1, 1.0, and 10 mg/kg body weight, 70.5–98.6% of the administered dose was excreted in feces within the first three days. Meanwhile, <0.5% of the administered dose accumulated in the liver, spleen, and intestines. The results obtained in another experiment on broilers with oral and inhalation administration of nanosilver at doses of 2–4 ppm and 40 ppm also indicate the predominant excretion of nanosilver in feces[210].

Even the intake of nanosilver in 10 chicken eggs does not exceed the daily dose according to the World Health Organization requirements [211]. According to these requirements, a modern person consumes on average 5–8 mcg of silver per day, while the recommended daily intake of silver (essential, or vital dose) is 50–100 mcg.

The data from all studies showed no toxic effect of the composite on the body of laying hens when administered orally three times in doses of AgNPs 0.2 and 0.4 mg·hen^{-1} per day. This is a manifestation of the high adaptive capabilities of laying hens in relation to this drug. The most important result was the selective endogenous accumulation of silver in the shell of chicken eggs compared to their protein and yolk. The reasons for this are not yet clear and require further research. However, this fact opens up the prospect of creating a simple and effective nanobiotechnology based on the developed AgNPs/SPH composite for obtaining chicken eggs with their own long-term protection from endogenous and exogenous pollution.

Currently, environmental risks and safety aspects of nanoparticle applications are attracting increasing interest. We placed greater emphasis on this aspect in our study, and the safety of AgNP application in laying hens was evaluated; the obtained results were promising. As we observed, after 20 days of AgNP application, the content of heavy metals (Cu and Pb) in the eggshell was significantly reduced (Table 9). However, prolonged AgNP application returned these parameters to control values. This finding is important for future research, which needs to consider the duration and dosage of AgNP application in poultry farming in greater detail.

14. Anticancer Properties of Silver/Hybrid Nanocomposites

In general, polymeric carriers significantly improve the stability of AgNPs and facilitate their interaction with cell membranes [66–68]. The biological activity of nanosilver and silver nanocomposites critically depends on the particle size, shape, synthesis method, carrier properties, and cancer cell type [67,68]. Silver nanoparticles obtained *in situ* in SPH matrices have been previously shown to exhibit a wide range of biological activity; their effectiveness against bacterial pathogens and fungi, in wound healing, and their usefulness in poultry and fisheries have been demonstrated. However, the anticancer activity of AgNPs/SPH composites remained unexplored for a long time. Therefore, the aim of our recent studies was to evaluate the anticancer activity of a promising nanocomposite using the SPH5 matrix as an example [212], the molecular and structural parameters of which are given in Tables 2 and 5.

The base AgNPs/SPH5 composite for these studies was prepared (and then purified from by-products) at the highest concentration of initial silver salt: $C_{AgNO3} = 7.1 \times 10^{-2}$ kg·m^{-3} and $C_{SPH} = 1.0$ kg·m^{-3}. In this case, as shown in an earlier study [152], the resulting composite had a fairly uniform structure (Figure 25a,b), in which fully swollen matrix particles with extended PAAm chains formed a network of entanglements in an aqueous medium (Figure 25d), holding numerous small AgNPs with $d_{av} = 6.1 \pm 2.8$ nm (Figure 25, inset).

Because of the highly swollen state, individual matrix particles were poorly visible in TEM micrographs. It is important to note that this structure retained high stability over time and in the light and demonstrated almost the same AgNP size, $d_{av} = 7.7 \pm 2.0$ nm (Figure 25c,d, and inset).

The anticancer activity studies used two different types of cancer cell lines and a viability test. Cell cultures were obtained from the European Collection of Animal Cell Cultures. Two cancer cell lines were used, such as B95-8 (monkey leukocytes transformed with Epstein-Barr virus) and Wish (a derivative of HeLa cell line with HeLa marker chromosomes). The Madin-Darby canine kidney (MDCK) cell line was used as a control. Cell cultures were obtained from the L.V. Gromashevsky Institute of Epidemiology and Infectious Diseases, Academy of Medical Sciences of Ukraine (Kyiv, Ukraine). Cells were cultured in sterile culture flasks in 45% DMEM (Dulbecco's modified Eagle's medium), 45% RPMI 1640 (Roswell Park Memorial Institute medium), and 10% FBS (fetal bovine serum) from Biowest (France). Cytotoxicity analysis was performed on the condition that at least 90% of viable cells were assessed using trypan blue. Cells were incubated in 96-well plates for 24 h at 37 °C.

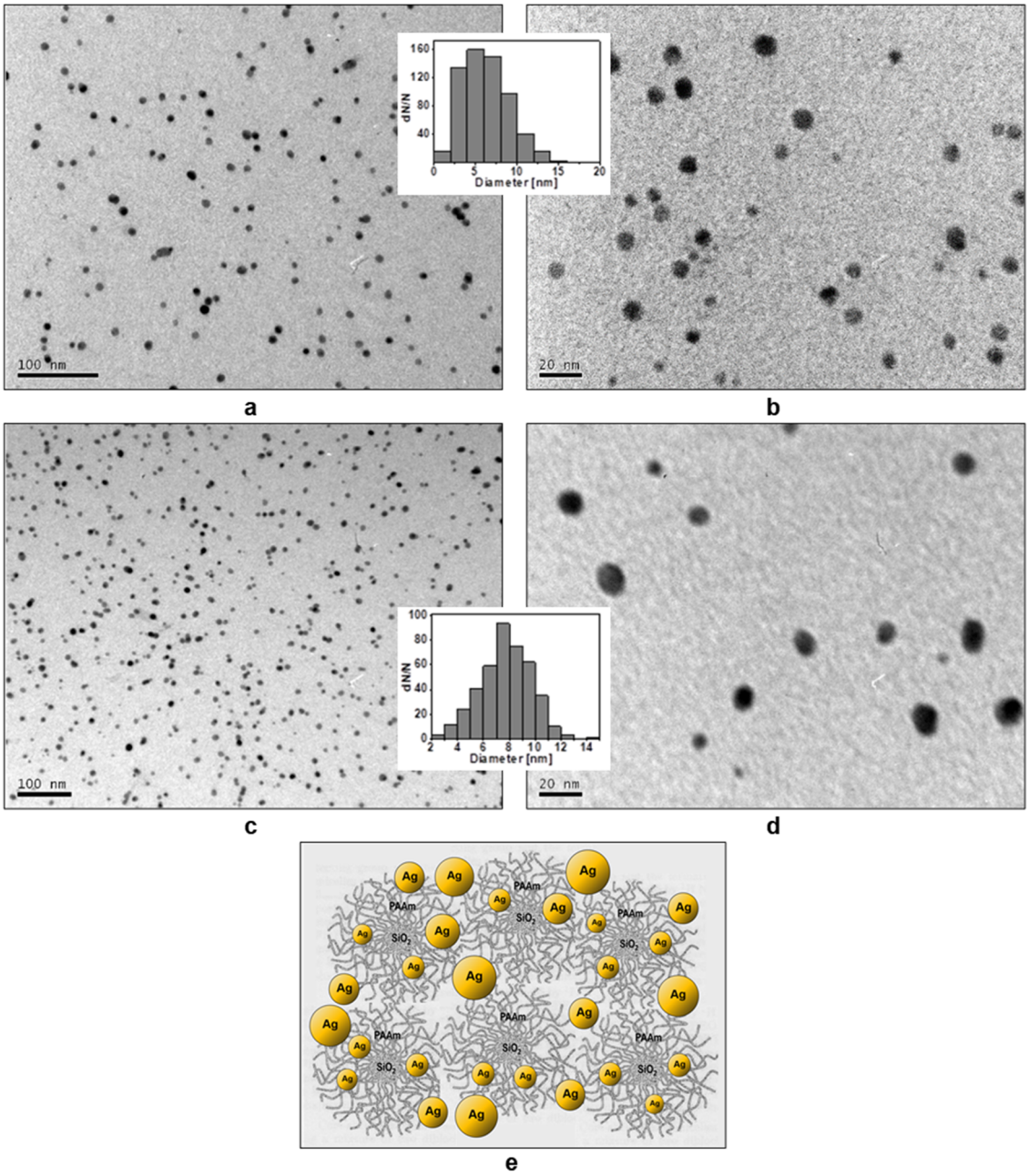

Figure 25. TEM micrographs at (**a**,**c**) lower and (**b**,**d**) higher magnifications of the as-received purified AgNPs/SPH5 nanocomposite and (**c**,**d**) the same nanocomposite after 3 months of storage in the light. (**e**) Schematic network of entanglements arising between swollen hybrid matrices due to the interaction of extended PAAm chains at a high concentration of formed AgNPs. The size distributions of AgNPs are shown in the insets. C_{SPH} = 1.0 kg·m^{-3}, C_{AgNO3} = 7.1 × 10^{-2} kg·m^{-3}, T = 20 °C.

The effect of the AgNPs/SPH5 composite on cell viability was assessed using the MTT test [212], which is based on the reduction of methyl tetrazolium by mitochondrial succinate dehydrogenase, followed by the formation of crystalline formazan, the concentration of which, after dissolution in DMSO, was determined by absorbance at 590 nm. To study the dependence of concentration on cell viability, serial dilutions of the original composite of 1:5, 1:10, 1:20, 1:40, and 1:80 were used. Cytotoxicity was assessed based on half-inhibitory concentrations (IC_{50}) found by fitting sigmoidal dose-response curves using OriginPro 7.0. One-way analysis of variance (ANOVA) was used to check reliability. $p < 0.05$ was taken as the significance level.

The effects of both the SPH5 carrier alone and the AgNPs/SPH5 nanocomposite on the viability of cancer cells and control MDCK cells were studied. The effects were compared at equal dilutions as described above. The SPH5 matrix was highly toxic to B95-8 cells but slightly toxic to Wish cells (Figure 26). In B95-8 cells, weak stimulation of viability by AgNPs/SPH5 was observed at high dilutions, which changed to inhibition with increasing concentration (Figure 26a). However, in the case of B95-8 cells, we could not detect a significant difference in viability inhibition between AgNPs/SPH5 and the pure matrix (Figure 26a). In contrast to B95-8 lymphocytes, the SPH5 carrier showed weak toxicity in Wish cells; the inhibition of viability observed at high dilutions did not exceed 20%. At the same time, the AgNPs/SPH5 composite showed high toxicity, significantly exceeding the toxicity of the pure carrier (Figure 26b). The IC_{50} values for B95-8 and Wish cells were 6.7×10^{-3} and 7.7×10^{-3} kg·m^{-3}, respectively. However, no significant difference was found between the sensitivity of B95-8 and Wish cells to the composite. To evaluate the utility of the AgNPs/SPH5 composite for further development of anticancer drugs, the cytotoxicity of the composite toward MDCK cells selected as a control was studied. As noted, neither SPH5 nor the AgNPs/SPH5 composite could achieve half-inhibition of cell viability. The maximum inhibition of MDCK cell viability by SPH5 did not exceed 10%, while the inhibition by the composite was at the level of ~30–35% (Figure 26c).

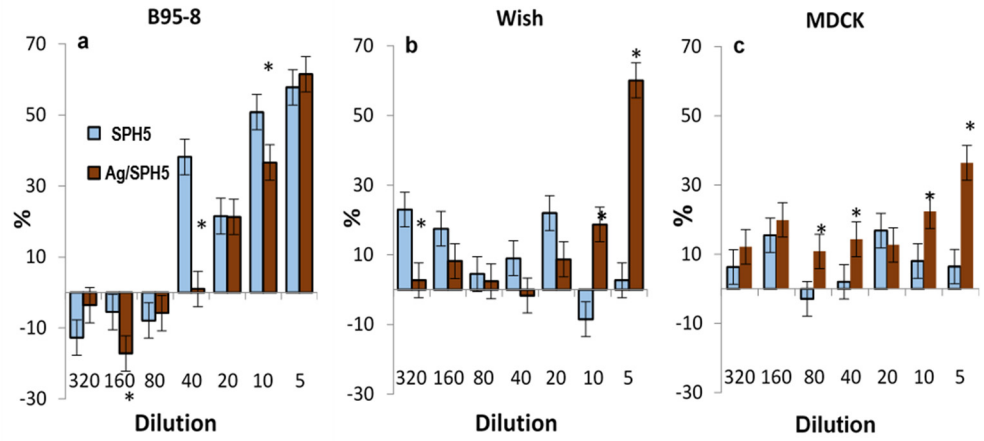

Figure 26. The effects of SPH5 (light bars) and AgNPs(Ag)/SPH5 (dark bars) on the viability of cancer cells: (**a**) B95-8, (**b**) Wish, and (**c**) the control MDCK. $M \pm m$, $n = 3$; * $p < 0.05$ as compared to SPH5.

Thus, low nanosized AgNPs in SPH5 carriers exhibited high anticancer activity. Very low IC_{50} values, compared to numerous published data, were found in B95-8 leukocytes and Wish cells, while the maximal inhibition of control MDCK cell viability did not exceed ≈ 30% (Figure 26c). As mentioned above, particle size is one of the important factors determining the anticancer efficacy of nanosilver [66,69–71]. However, the IC_{50} values obtained for AgNPs in different cancer cell lines varied in a very wide range: from tenths to hundreds of μg·mL^{-1} [66,68]. Based on the literary data, there was a tendency of increasing cytotoxicity with the lessening of the particle size [66–71]. The IC_{50} values determined in our work for the AgNPs/SPH5 composite in both cancer cell lines were close to published data obtained for similarly sized AgNPs and were near the lower end of the IC_{50} range [67,68]. Considering the particle size dependence of cytotoxicity,

obtaining particles with a narrow size distribution is important for data reproducibility. The relatively narrow particle size distribution was one of the advantages of the AgNPs/SPH5 composite compared to many published systems [67,68].

It can be concluded that, compared to published data, the AgNPs/SPH5 composite demonstrated high anticancer efficacy, which distinguishes this system from many others described in the literature, and their IC_{50} for the studied cancer cell lines were at the lower end of the concentration range found for AgNPs [66–68].

Based on the experiments conducted, the following main points can be emphasized. The AgNPs/SPH5 nanocomposite exhibited high anticancer activity and significantly lower toxicity to control MDCK cells, indicating that this system is a good candidate for the development of anticancer drugs. The advantages of the AgNPs/SPH5 composite include its cost-effective synthesis and high antibacterial activity. Low MIC values close to IC_{50} obtained for cancer cells and low toxicity to control MDCK cells make this composite promising for the development of both anticancer and antibacterial drugs, but their specificity to different cancer cell lines and bacterial types requires further evaluation.

The studies reviewed in this work demonstrated a broad range of AgNPs applications, including antibacterial and anticancer research, wound healing, and fish and poultry farming. However, several limitations should be acknowledged. First, the antibacterial activity was strongly dependent on the Ag loading of the nanocomposites, and the inhibition zones were closely related to the AgNPs metal concentration (C_{AgNPs}). Notably, for the two studied systems with different AgNP loadings (1.2×10^{-2} and 5.0×10^{-2} kg/m^3) and different molar ratios of Ag/PAAm, similar inhibition zones were obtained at similar C_{AgNPs} values. Therefore, further detailed studies are needed to clarify how antibacterial properties depend on the chemical and structural characteristics of AgNPs, including Ag loading, the molar ratio of Ag nanoparticles to the polymer carrier, and the molecular weight of PAAm, in order to determine the optimal relationships among these parameters for maximum antibacterial efficiency. Second, because the main focus of this work was the range of potential AgNPs applications, we could not provide a detailed analysis of the biological mechanisms underlying their effects. Extensive future studies are therefore required to elucidate the mechanisms responsible for the antibacterial and anticancer activities, as well as for other applications preliminarily demonstrated in this work. Third, environmental risks and safety aspects of nanoparticle applications are currently attracting considerable attention. Although the safety of AgNPs applications was evaluated in many of our studies, including those involving fish, poultry farming, and anticancer experiments, future research should assess these risks more systematically and on a regular basis.

15. Concluding Remarks

The studied silica/polyacrylamide hybrids combine a special structure, high adsorption properties of the ionic "core" SiO_2, high binding capacity of the non-ionic "corona" PAAm, and additional non-covalent interactions between the "core" and the "corona". This makes them excellent nanoreactors for *in situ* synthesis and retention of various metal nanoparticles. Particularly successful are the obtained hybrid composites with AgNPs, which, during the *in situ* synthesis process using sodium borohydride as a reducing agent, are rapidly transformed in the hybrid matrices from the state of primary particles to an ordered/crystalline state. This ensures the stability of the original and purified AgNP/SPH dispersions for long periods (from several months to at least one year) even in light.

The creation of these highly dispersed and effective biocidal composites has a number of advantages over many others. Both components of the hybrids are biocompatible and biodegradable. Simple and inexpensive "one-pot" synthesis of individual SPHs of various structures is carried out at room temperature and does not require preliminary functionalization of the silica surface. The developed method enables easy determination of the structure of the obtained products, including the number and length of PAAm chains per SiO_2 "core" in hybrid particles. The subsequent *in situ* synthesis of AgNP/SPH composites is also low-temperature and leads to the formation of small (<10 nm) silver nanoparticles with a high yield and a fairly

narrow size distribution. This determines the high biocidal activity of such composites. The proposed simple, cheap, and environmentally friendly method for purifying composites from excess reagents and by-products of synthesis allows them to be used even in the field of biomedicine.

Aqueous solutions of AgNPs/SPH composites showed high and prolonged antibacterial and antifungal effectivity against gram-positive and gram-negative bacteria (*Staphylococcus aureus*, *Escherichia coli*, *Pseudomonas aeruginosa*), yeast (*Candida albicans*), and mycelial fungi (*Fusarium oxysporum* and *Cladosporium shpaerospermum*), which are traditional pathogens of hospital infections. Further, wider microbiological experiments conducted using cotton fabrics impregnated with one of these composites confirmed the stable and long-lasting bactericidal and fungistatic action of the composite over a very wide range of concentrations. The obtained results, together with the established ability of the composite to heal open wounds at a high rate and without additional primary inflammation, allowed us to conclude that AgNPs/SPH composites have high potential for the treatment and long-term disinfection of not only wound dressings and hygienic materials (bandages, napkins, plasters) but also cotton fabrics, underwear, and other clothing.

AgNPs/SPH composites demonstrated significant bactericidal and bacteriostatic activity against fish pathogenic bacteria *Aeromonas hydrophila* and *Pseudomonas* sp., common in fishponds. For one of the composites, a general safe range of AgNPs concentrations ($C_{AgNPs} < 1.2 \times 10^{-2}$ kg·m^{-3}) was determined, at which virtually no lethal effects were observed for the animal test organisms, and no reduction in root mass/size was observed in the plant organism. As special studies of the toxicity and genotoxicity of the composite have shown, in the concentration range found, it can be successfully used as an antibacterial agent in fish farming without any biological risks, even at the cellular level.

In the agricultural sector, the effect of the AgNPs/SPH composite on the growing season of winter wheat plants after pre-sowing treatment of their seeds has been established. These experiments were not completed, but their continuation is promising in terms of further accumulated data on the effect of AgNP on the growth and yield of this crop.

Some of the most interesting studies were the *in vivo* effects of the AgNPs/SPH composite on laying hens and their eggs when administered orally three times a month at 10-day intervals at AgNPs doses of 0.2 and 0.4 mg·hen^{-1} per day. The most striking thing here was the first established effect of selective endogenous accumulation of silver in the shells of chicken eggs, compared with their proteins and yolks. This opened up the prospect of creating a new, simple, and effective nanobiotechnology for producing chicken eggs with their own long-term protection from endogenous and exogenous contaminants. The studies also did not reveal any toxic effects of the composite on the bodies of laying hens, indicating their high adaptive capacity to this preparation.

The AgNP/SPH composite sample also proved to be a good candidate for anticancer drug development. It demonstrated high anticancer activity with low MIC values close to the IC_{50} parameters for the studied B95-8 and Wish cancer cells, and significantly lower toxicity relative to control MDCK cells. Thus, AgNPs/SPH composites can be considered as a promising multifunctional material for modern nanotechnologies.

Acknowledgments

The authors are grateful for the support provided by the Institutes of Macromolecular Chemistry, Kholodny Institute of Botany, Bogomoletz Institute of Physiology, Zabolotny Institute of Microbiology and Virology of the National Academy of Sciences of Ukraine, as well as by Taras Shevchenko National University of Kyiv, the National University of Life and Environmental Sciences of Ukraine, and the Scientific-Research Center of "Kernel". This statement is intended as an acknowledgement of institutional support and does not represent a funding declaration.

Author Contributions

T.Z. contributed to the concept and methodology of synthesis and characterization of hybrids and their composites with AgNPs, prepared a series of starting nanocomposites for biological studies, analyzed the data and wrote the main part of the manuscript. N.P. studied some properties of the hybrids, including their functions as templates in the formation of AgNPs, obtained nanocomposites for biological experiments, and participated in the preparation of the manuscript. V.K. conducted, analyzed and summarized structural studies of hybrids and their nanocomposites using wide-angle and small-angle X-ray scattering methods. D.K. conducted and discussed the morphology studies of hybrids and their nanocomposites using transmission electron microscopy. O.D. obtained silica/polyacrylamide hybrids, studied the kinetic features of their synthesis and a number of properties. T.K. studied and analyzed the antibacterial and antifungal properties of hybrids and nanocomposites with AgNPs. T.B. conducted comparative studies *in vivo* of the wound healing ability of one of the hybrids and its nanocomposite with AgNPs. O.K. has carried out a series of comprehensive studies of the antimicrobial, toxic and genotoxic properties of silver/hybrid nanocomposites in relation to fish bacteria, various aquatic test organisms and fish embryos. L.S. developed and conducted *in vivo* studies and analysis of the complex effects of the silver/hybrid nanocomposite on laying hens and their eggs. B.M. studied the effect of silver/hybrid composite on winter wheat cultivation. S.Z. performed a series of anticancer studies using the pure hybrid and its composite with AgNPs. O.A. designed the microbiological and anticancer experiments, analyzed the data, and wrote the relevant parts of the manuscript.

Ethics Statement

Ethical review and approval were waived for this study because it is a review article based on previously published work, for which all necessary ethics approvals had already been obtained.

Informed Consent Statement

Not applicable.

Data Availability Statement

Data are provided within the manuscript.

Funding

This research received no external funding.

Declaration of Competing Interest

The authors declare that they have no known competing financial interests or personal relationships that could have appeared to influence the work reported in this paper.

References

1. Klasen HJ. A historical review of the use of silver in the treatment of burns. II. Renewed interest for silver. *Burns* **2000**, *26*, 131–138. DOI:10.1016/S0305-4179(99)00116-3
2. Duman H, Eker F, Akda E, Witkowska AM, Bechelany M, Karav S. Silver nanoparticles: A comprehensive review of synthesis methods and chemical and physical properties. *Nanomaterials* **2024**, *14*, 1527. DOI:10.3390/nano14181527
3. Abbas R, Luo J, Qi X, Naz A, Khan IA, Liu H, et al. Silver nanoparticles: Synthesis, structure, properties and applications. *Nanomaterials* **2024**, *14*, 1425. DOI:10.3390/nano14171425

4. Shayo GM, Elimbinzi E, Shao GN. Preparation methods, applications, toxicity and mechanisms of silver nanoparticles as bactericidal agent and superiority of green synthesis method. *Heliyon* **2024**, *10*, e36539. DOI:10.1016/j.heliyon.2024.e36539
5. Chen ZY, Li NJ, Cheng FY, Hsueh JF, Huang CC, Lu FI, et al. The effect of the chorion on size-dependent acute toxicity and underlying mechanisms of amine-modified silver nanoparticles in zebrafish embryos. *Int. J. Mol. Sci.* **2020**, *21*, 2864. DOI:10.3390/ijms21082864
6. Dhir R, Chauhan S, Subham P, Kumar S, Sharma P, Shidiki A, et al. Plant-mediated synthesis of silver nanoparticles: Unlocking their pharmacological potential—A comprehensive review. *Front. Bioeng. Biotechnol.* **2024**, *11*, 1324805. DOI:10.3389/fbioe.2023.1324805
7. Barmatov EV, Medvedev AV, Barmatova MV. Particulate Silver Biocides and Methods for Biocide Use in Fracturing Fluids. U.S. Patent 11/942,839, 22 May 2008.
8. Ravishankar RV, Jamuna BA. Nanoparticles and their potential application as antimicrobials. In *Science Against Microbial Pathogens: Communicating Current Research and Technological Advances*; Méndez-Vilas A, Ed.; Formatex: Badajoz, Spain, 2011; pp. 197–209.
9. Li H, Gao Y, Li C, Ma G, Shang Y, Sun Y. Comparative study of the antibacterial mechanisms of silver ion and silver nanoparticles by Fourier transform infrared spectroscopy. *Vib. Spectrosc.* **2016**, *85*, 112–121. DOI:10.1016/j.vibspec.2016.04.007
10. Park HJ, Kim JY, Kim J, Lee JH, Hahn JS, Gu MB, et al. Silver-ion-mediated reactive oxygen species generation affecting bactericidal activity. *Water Res.* **2009**, *43*, 1027–1032. DOI:10.1016/j.watres.2008.12.002
11. Nowack B, Krug HF, Height M. 120 years of nanosilver history: Implications for policy makers. *Environ. Sci. Technol.* **2011**, *45*, 1177–1183. DOI:10.1021/es103316q
12. Turkevich J, Stevenson P, Hillier J. A study of the nucleation and growth processes in the synthesis of colloidal gold. *Discuss. Faraday Soc.* **1951**, *11*, 55–75. DOI:10.1039/df9511100055
13. Tran QH, Nguyen VQ, Le AT. Silver nanoparticles: Synthesis, properties, toxicology, applications and perspectives. *Adv. Nat. Sci. Nanosci. Nanotechnol.* **2013**, *4*, 033001. DOI:10.1088/2043-6262/4/3/033001
14. Lu K. *Nanoparticulate Materials: Synthesis, Characterization, and Processing*; John Wiley & Sons, Inc.: Hoboken, NJ, USA, 2013.
15. Lal HM, Thomas S, Li T, Maria HJ. (Eds.). *Polymer Nanocomposites Based on Silver Nanoparticles: Synthesis, Characterization and Applications*; Springer Nature: Cham, Switzerland, 2021.
16. Yin IX, Zhang J, Zhao IS, Mei ML, Li Q, Chu CH. The antibacterial mechanism of silver nanoparticles and its application in dentistry. *Int. J. Nanomed.* **2020**, *15*, 2555–2562. DOI:10.2147/IJN.S246764
17. More PR, Pandit S, De Filippis A, Franci G, Mijakovic I, Galdiero M. Silver nanoparticles: Bactericidal and mechanistic approach against drug resistant pathogens. *Microorganisms* **2023**, *11*, 369. DOI:10.3390/microorganisms11020369
18. Lara HH, Garza-Trevino EN, Ixtepan-Turrent L, Singh DK. Silver nanoparticles are broad-spectrum bactericidal and virucidal compounds. *J. Nanobiotechnol.* **2011**, *9*, 30. DOI:10.1186/1477-3155-9-30
19. Maity D, Kanti Bain M, Bhowmick B, Sarkar J, Saha S, Acharya K, et al. *In situ* synthesis, characterization and antimicrobial activity of silver nanoparticles using water soluble polymer. *J. Appl. Polym. Sci.* **2011**, *122*, 2189–2196. DOI:10.1002/app.34266
20. Martinez-Castañón GA, Niño-Martinez N, Martinez-Gutierrez F, Martinez JR, Ruiz F. Synthesis and antibacterial activity of silver nanoparticles with different sizes. *J. Nanopart. Res.* **2008**, *10*, 1343–1348. DOI:10.1007/s11051-008-9428-6
21. Bruna T, Maldonado-Bravo F, Jara P, Caro N. Silver nanoparticles and their antibacterial applications. *Int. J. Mol. Sci.* **2021**, *22*, 7202. DOI:10.3390/ijms22137202
22. Van Dong P, Ha CH, Binh LT, Kasbohm J. Chemical synthesis and antibacterial activity of novel-shaped silver nanoparticles. *Int. Nano Lett.* **2012**, *2*, 9. DOI:10.1186/2228-5326-2-9
23. Romero-Urbina DG, Lara HH, Velázquez-Salazar JJ, Arellano-Jiménez MJ, Larios E, Srinivasan A, et al. Ultrastructural changes in methicillin-resistant *Staphylococcus aureus* induced by positively charged silver nanoparticles. *Beilstein J. Nanotechnol.* **2015**, *6*, 2396–2405. DOI:10.3762/bjnano.6.246
24. Murphy M, Ting K, Zhang X, Soo C, Zheng Z. Current development of silver nanoparticle preparation, investigation, and application in the field of medicine. *J. Nanomater.* **2015**, *2015*, 696918. DOI:10.1155/2015/696918
25. Kim TH, Kim M, Park HS, Shin US, Gong MS, Kim HW. Size-dependent cellular toxicity of silver nanoparticles. *J. Biomed. Mater. Res. Part A* **2012**, *100*, 1033–1043. DOI:10.1002/jbm.a.34053
26. Kennedy DC, Orts-Gil G, Lai CH, Müller L, Haase A, Luch A, et al. Carbohydrate functionalization of silver nanoparticles modulates cytotoxicity and cellular uptake. *J. Nanobiotechnol.* **2014**, *12*, 59. DOI:10.1186/s12951-014-0059-z

27. Gilbert P, McBain AJ. Potential impact of increased use of biocides in consumer products on prevalence of antibiotic resistance. *Clin. Microbiol. Rev.* **2003**, *16*, 189–208. DOI:10.1128/CMR.16.2.189-208.2003
28. European Commission, Health & Consumer Protection DG, SCENIHR. *Assessment of the Antibiotic Resistance Effects of Biocides*; European Commission: Brussels, Belgium, 2009.
29. Bobbarala V. (Ed.). *A Search for Antibacterial Agents*; InTech: Rijeka, Croatia, 2012; p. 344.
30. De Hoog GS, Guarro J. *Atlas of Clinical Fungi; Electronic Version 3.1*; Centraalbureau voor Schimmelcultures: Utrecht, The Netherlands, 2011.
31. Huh AJ, Kwon YJ. Nanoantibiotics: A new paradigm for treating infectious diseases using nanomaterials in the antibiotics resistant era. *J. Control. Release* **2011**, *156*, 128–145. DOI:10.1016/j.jconrel.2011.07.002
32. Ray M, Yadav A, Gade A. Silver nanoparticles as a new generation of antimicrobials. *Biotechnol. Adv.* **2009**, *27*, 76–83. DOI:10.1016/j.biotechadv.2008.09.002
33. Domènech B, Muñoz M, Muraviev DN, Macanás J. Polymer-silver nanocomposites as antibacterial materials. In *Microbial Pathogens and Strategies for Combating Them: Science, Technology and Education*; Méndez-Vilas A, Ed.; Formatex: Badajoz, Spain, 2013; pp. 630–640.
34. Fondevila M. Potential use of silver nanoparticles as an additive in animal feeding. In *Silver Nanoparticles*; Perez DP, Ed.; InTech: Mountain View, CA, USA, 2010; pp. 325–334.
35. Fondevila M, Herrer M, Casallas C, Abecia L, Ducha JJ. Silver nanoparticles as a potential antimicrobial additive for weaned pigs. *Anim. Feed Sci. Technol.* **2009**, *150*, 259–269. DOI:10.1016/j.anifeedsci.2008.09.003
36. Da Costa Junior SD, de Almeida Campos LA, Palácio SB, Ferro Cavalcanti IM. Silver nanoparticles as a promising therapeutic strategy for infections caused by resistant bacteria in cattle and birds. *Approaches Poult. Dairy Vet. Sci.* **2018**, *4*, 348–352. DOI:10.31031/APDV.2018.04.000592
37. Abdelsalam M, Al-Homidan I, Ebeid T, Abou-Emera O, Mostafa M, Abd El-Razik M, et al. Effect of silver nanoparticle administration on productive performance, blood parameters, antioxidative status, and silver residues in growing rabbits under hot climate. *Animals* **2019**, *9*, 845. DOI:10.3390/ani9100845
38. Michalak I, Dziergowska K, Alagawany M, Farag MR, El-Shall NA, Tuli HS, et al. The effect of metal-containing nanoparticles on the health, performance and production of livestock animals and poultry. *Vet. Q.* **2022**, *42*, 68–94. DOI:10.1080/01652176.2022.2073399
39. Patra A, Lalhriatpuii M. Progress and prospect of essential mineral nanoparticles in poultry nutrition and feeding—A review. *Biol. Trace Elem. Res.* **2020**, *197*, 233–253. DOI:10.1007/s12011-019-01959-1
40. Abd El-Ghany WA. Nanotechnology and its considerations in poultry field: An overview. *J. Hell. Vet. Med. Soc.* **2019**, *70*, 1611–1616. DOI:10.12681/jhvms.21783
41. Anwar MI, Awais MM, Akhtar M, Navid MT, Muhammad F. Nutritional and immunological effects of nanoparticles in commercial poultry birds. *World's Poult. Sci. J.* **2019**, *75*, 261–272. DOI:10.1017/S0043933919000199
42. Moustafa KEM, Moustafa MEE, Ghazalah AA, Rehan AAA. Effect of dietary nanosilver on broiler performance. *Int. J. Poult. Sci.* **2015**, *14*, 177–182. DOI:10.3923/ijps.2015.177.182
43. Saleh AA, El-Magd MA. Beneficial effects of dietary silver nanoparticles and silver nitrate on broiler nutrition. *Environ. Sci. Pollut. Res.* **2018**, *25*, 27031–27038. DOI:10.1007/s11356-018-2730-7
44. Ahmadi F, Kurdestany AH. The impact of silver nanoparticles on growth performance, lymphoid organs and oxidative stress indicators in broiler chicks. *Glob. Vet.* **2010**, *5*, 366–370. Available online: https://www.researchgate.net/profile/Farhad-Ahmadi-4/publication/216528277_The_Impact_of_silver_nano_particles_on_growth_performance_lymphoid_organs_and_oxidative_stress_indicators_in_broiler_chicks/links/5bb6a3b292851c7fde2e9028/The-Impact-of-silver-nano-particles-on-growth-performance-lymphoid-organs-and-oxidative-stress-indicators-in-broiler-chicks.pdf (accessed on 14 February 2026).
45. Ognik K, Sembratowicz I, Cholewińska E, Wlazło Ł, Nowakowicz-Dębek B, Szlązak R, et al. The effect of chemically synthesized silver nanoparticles on performance and the histology and microbiological profile of the jejunum in chickens. *Ann. Anim. Sci.* **2016**, *16*, 439–450. DOI:10.1515/aoas-2015-0067
46. Kulak E, Ognik K, Stępniowska A, Sembratowicz I. The effect of administration of silver nanoparticles on silver accumulation in tissues and immune and antioxidant status of chickens. *J. Anim. Feed Sci.* **2018**, *27*, 44–54. DOI:10.22358/jafs/84978/2018
47. Dosoky WM, Fouda MMG, Alwan AB, Abdelsalam NR, Taha AE, Ghareeb RY, et al. Dietary supplementation of silver–silica nanoparticles promotes histological, immunological, ultrastructural, and performance parameters of broiler chickens. *Sci. Rep.* **2021**, *11*, 4166. DOI:10.1038/s41598-021-83753-5

48. Vadalasetty KP, Lauridsen C, Engberg RM, Vadalasetty R, Kutwin M, Chwalibog A, et al. Influence of silver nanoparticles on growth and health of broiler chickens after infection with *Campylobacter jejuni*. *BMC Vet. Res.* **2018**, *14*, 1. DOI:10.1186/s12917-017-1323-x
49. Grodzik M, Sawosz E. The influence of silver nanoparticles on chicken embryo development and bursa of *Fabricius morphology*. *J. Anim. Feed Sci.* **2006**, *15*, 111–114. DOI:10.22358/jafs/70155/2006
50. Sawosz F, Pineda L, Hotowy A, Hyttel P, Sawosz E, Szmidt M, et al. Nanonutrition of chicken embryos. The effect of silver nanoparticles and glutamine on molecular responses and the morphology of pectoral muscle. *Baltic J. Comp. Clin. Syst. Biol.* **2012**, *2*, 29–45. Available online: https://www.academia.edu/download/103435974/Filip_Sawosz_Nanonutrition_of_chicken_embryos_copy_2.pdf (accessed on 27 January 2026).
51. Bhanja S, Hotowy A, Mehra M, Sawosz E, Pineda L, Vadalasetty K, et al. In ovo administration of silver nanoparticles and/or amino acids influence metabolism and immune gene expression in chicken embryos. *Int. J. Mol. Sci.* **2015**, *16*, 9484–9503. DOI:10.3390/ijms16059484
52. Orobchenko OL, Roman'ko MY, Kutsan OT. The impact of potential feed additive nanocomposite (Ag, Cu, Fe, Mn dioxide) on eggs' quality parameters of laying hens compared with metal salts. *J. Vet. Med. Biotechnol. Biosaf.* **2015**, *1*, 10–13. Available online: http://www.irbis-nbuv.gov.ua/cgi-bin/irbis_nbuv/cgiirbis_64.exe?C21COM=2&I21DBN=UJRN&P21DBN=UJRN&IMAGE_FILE_DOWNLOAD=1&Image_file_name=PDF/jvmbb_2015_1_3_4.pdf (accessed on 12 February 2026).
53. Katarzyńska-Banasik D, Grzesiak M, Kowalik K, Sechman A. Administration of silver nanoparticles affects ovarian steroidogenesis and may influence thyroid hormone metabolism in hens (*Gallus domesticus*). *Ecotoxicol. Environ. Saf.* **2021**, *208*, 111427. DOI:10.1016/j.ecoenv.2020.111427
54. Sawosz E, Binek M, Grodzik M, Zielińska M, Sysa P, Szmidt M, et al. Influence of hydrocolloidal silver nanoparticles on gastrointestinal microflora and morphology of enterocytes of quails. *Arch. Anim. Nutr.* **2007**, *61*, 444–451. DOI:10.1080/17450390701664314
55. Rezaei A, Farzinpour A, Vaziry A, Jalili A. Effects of silver nanoparticles on hematological parameters and hepatorenal functions in laying Japanese quails. *Biol. Trace Elem. Res.* **2018**, *185*, 475–485. DOI:10.1007/s12011-018-1267-4
56. Ibrahim FA, Moustafa KEME, El Sabry MI, Badr JM, Hassan ASI. Effect of egg disinfection by silver nanoparticles on eggshell microbial load, hatchability and post-hatch performance of quail chicks. *Int. J. Poult. Sci.* **2018**, *17*, 234–242. DOI:10.3923/ijps.2018.234.242
57. Moustafa EM, Khalil RH, Saad TT, Amer MT, Shukry M, Farrag F, et al. Silver nanoparticles as an antibacterial agent in *Oreochromis niloticus* and *Sparus auratus* fish. *Aquac. Res.* **2021**, *52*, 6218–6234. DOI:10.1111/are.15484
58. Popoola OM, Behera BK, Kumar V. Dietary silver nanoparticles as immunostimulant on rohu (*Labeo rohita*): Effects on growth, cellular ultrastructure, immune-gene expression, and survival against *Aeromonas hydrophila*. *Fish Shellfish Immunol. Rep.* **2023**, *4*, 100080. DOI:10.1016/j.fsirep.2022.100080
59. Márquez JCM, Partida AH, Dosta MdelCM, Mejía JC, Martínez JAB. Silver nanoparticles applications (AgNPs) in aquaculture. *Int. J. Fish. Aquat. Stud.* **2018**, *6*, 5–11. Available online: https://www.academia.edu/download/87514647/6-1-39-560.pdf (accessed on 15 March 2026).
60. EI-Jakee J, Elshamy S, Hassan AW, Abdelsalam M, Younis N, El-Hady MA, et al. Isolation and characterization of mycoplasmas from some moribund Egyptian fishes. *Aquac. Int.* **2020**, *28*, 901–912. DOI:10.1007/s10499-019-00502-2
61. Kole C, Kumar DS, Khodakovskaya MV. (Eds.). *Plant Nanotechnology: Principles and Practices;* Springer: Cham, Switzerland, 2016.
62. Farooqui A, Tabassum H, Ahmad A, Mabood A, Ahmad A, Ahmad IF. Role of nanoparticles in growth and development of plants: A review. *Int. J. Pharma Bio Sci.* **2016**, *7*, 22–37. DOI:10.22376/ijpbs.2016.7.4.p22-37
63. Arif N, Yadav V, Singh S, Singh S, Ahmad P, Mishra RK, et al. Influence of high and low levels of plant-beneficial heavy metal ions on plant growth and development. *Front. Environ. Sci.* **2016**, *4*, 69. DOI:10.3389/fenvs.2016.00069
64. Morales-Díaz AB, Ortega-Ortíz H, Juárez-Maldonado A, Cadenas-Pliego G, González-Morales S, Benavides-Mendoza A. Application of nanoelements in plant nutrition and its impact in ecosystems. *Adv. Nat. Sci. Nanosci. Nanotechnol.* **2017**, *8*, 013001. DOI:10.1088/2043-6254/8/1/013001
65. Rastogi A, Zivcak M, Sytar O, Kalaji HM, He X, Mbarki S, et al. Impact of metal and metal oxide nanoparticles on plant: A critical review. *Front. Chem.* **2017**, *5*, 78. DOI:10.3389/fchem.2017.00078
66. Husain S, Nandi A, Simnani FZ, Saha U, Ghosh A, Sinha A, et al. Emerging trends in advanced translational applications of silver nanoparticles: A progressing dawn of nanotechnology. *J. Funct. Biomater.* **2023**, *14*, 47. DOI:10.3390/jfb14010047

67. Miranda RR, Sampaio I, Zucolotto V. Exploring silver nanoparticles for cancer therapy and diagnosis. *Colloids Surf. B Biointerfaces* **2022**, *210*, 112254. DOI:10.1016/j.colsurfb.2021.112254
68. Huy TQ, Huyen PTM, Le AT, Tonezzer M. Recent advances of silver nanoparticles in cancer diagnosis and treatment. *Anticancer Agents Med. Chem.* **2020**, *20*, 1276–1287. DOI:10.2174/1871520619666190710121727
69. Carlson C, Hussain SM, Schrand AM, K. Braydich-Stolle L, Hess KL, Jones RL, et al. Unique cellular interaction of silver nanoparticles: Size-dependent generation of reactive oxygen species. *J. Phys. Chem. B* **2008**, *112*, 13608–13619. DOI:10.1021/jp712087m
70. Miethling-Graff R, Rumpker R, Richter M, Verano-Braga T, Kjeldsen F, Brewer J, et al. Exposure to silver nanoparticles induces size- and dose-dependent oxidative stress and cytotoxicity in human colon carcinoma cells. *Toxicol. In Vitro* **2014**, *28*, 1280–1289. DOI:10.1016/j.tiv.2014.06.005
71. Avalos A, Haza AI, Mateo D, Morales P. Cytotoxicity and ROS production of manufactured silver nanoparticles of different sizes in hepatoma and leukemia cells. *J. Appl. Toxicol.* **2014**, *34*, 413–423. DOI:10.1002/jat.2957
72. Barcińska E, Wierzbicka J, Zauszkiewicz-Pawlak A, Jacewicz D, Dabrowska A, Inkielewicz-Stepniak I. Role of oxidative and nitro-oxidative damage in silver nanoparticles cytotoxic effect against human pancreatic ductal adenocarcinoma cells. *Oxid. Med. Cell. Longev.* **2018**, *2018*, 251961. DOI:10.1155/2018/8251961
73. Zhang XF, Gurunathan S. Combination of salinomycin and silver nanoparticles enhances apoptosis and autophagy in human ovarian cancer cells: An effective anticancer therapy. *Int. J. Nanomed.* **2016**, *11*, 3655–3675. DOI:10.2147/IJN.S111279
74. Druck T, Cheung DG, Park D, Trapasso F, Pichiorri F, Gaspari M, et al. Fhit–Fdxr interaction in the mitochondria: Modulation of reactive oxygen species generation and apoptosis in cancer cells. *Cell Death Dis.* **2019**, *10*, 147. DOI:10.1038/s41419-019-1414-7
75. Wang H, Gao Z, Liu X, Agarwal P, Zhao S, Conroy DW, et al. Targeted production of reactive oxygen species in mitochondria to overcome cancer drug resistance. *Nat. Commun.* **2018**, *9*, 562. DOI:10.1038/s41467-018-02915-8
76. Xu Z, Feng Q, Wang M, Zhao H, Lin Y, Zhou S. Green biosynthesized silver nanoparticles with aqueous extracts of *Ginkgo biloba* induce apoptosis via mitochondrial pathway in cervical cancer cells. *Front. Oncol.* **2020**, *10*, 575415. DOI:10.3389/fonc.2020.575415
77. Liu W, Worms I, Slaveykova VI. Interaction of silver nanoparticles with antioxidant enzymes. *Environ. Sci. Nano* **2020**, *7*, 1507–1517. DOI:10.1039/C9EN01284B
78. Aueviriyavit S, Phummiratch D, Maniratanachote R. Mechanistic study on the biological effects of silver and gold nanoparticles in Caco-2 cells: Induction of the Nrf2/HO-1 pathway by high concentrations of silver nanoparticles. *Toxicol. Lett.* **2014**, *224*, 73–83. DOI:10.1016/j.toxlet.2013.09.020
79. Sarkar MK, Vadivel V, Charan Raja MR, Mahapatra SK. Potential anti-proliferative activity of AgNPs synthesized using *M. longifolia* in 4T1 cell line through ROS generation and cell membrane damage. *J. Photochem. Photobiol. B* **2018**, *186*, 160–168. DOI:10.1016/j.jphotobiol.2018.07.014
80. Zhang XF, Liu ZG, Shen W, Gurunathan S. Silver nanoparticles: Synthesis, characterization, properties, applications, and therapeutic approaches. *Int. J. Mol. Sci.* **2016**, *17*, 1534. DOI:10.3390/ijms17091534
81. Ahmadi A, Haneef M, Ahmad N, Kamal A, Jaswani S, Khan F. Biological synthesis of silver nanoparticles and their medical applications. *World Acad. Sci. J.* **2024**, *6*, 22. DOI:10.3892/wasj.2024.237
82. Giri AK, Jena B, Biswal B, Pradhan AK, Arakha M, Acharya S, et al. Green synthesis and characterization of silver nanoparticles using *Eugenia roxburghii* DC. extract and activity against biofilm-producing bacteria. *Sci. Rep.* **2022**, *12*, 8383. DOI:10.1038/s41598-022-12484-y
83. Rozenberg BA, Tenne R. Polymer-assisted fabrication of nanoparticles and nanocomposites. *Prog. Polym. Sci.* **2008**, *33*, 40–112. DOI:10.1016/j.progpolymsci.2007.07.004
84. Natsuki J, Natsuki T, Hashimoto Y. A review of silver nanoparticles: Synthesis methods, properties and applications. *Int. J. Mater. Sci. Appl.* **2015**, *4*, 325–332. DOI:10.11648/j.ijmsa.20150405.17
85. Hood MA, Mari M, Muñoz-Espí R. Synthetic strategies in the preparation of polymer/inorganic hybrid nanoparticles. *Materials* **2014**, *7*, 4057–4087. DOI:10.3390/ma7054057
86. Lee SH, Jun B-H. Silver nanoparticles: Synthesis and application for nanomedicine. *Int. J. Mol. Sci.* **2019**, *20*, 865. DOI:10.3390/ijms20040865
87. García-Barrasa J, López-de-Luzuriaga JM, Monge M. Silver nanoparticles: Synthesis through chemical methods in solution and biomedical applications. *Cent. Eur. J. Chem.* **2011**, *9*, 7–19. DOI:10.2478/s11532-010-0124-x
88. Kvítek L, Panáček A, Soukupová J, Kolář M, Večeřová R, Prucek R, et al. Effect of surfactants and polymers on stability and antibacterial activity of silver nanoparticles. *J. Phys. Chem. C* **2008**, *112*, 5825–5834. DOI:10.1021/jp711616v

89. Chou K-S, Lai Y-S. Effect of polyvinyl pyrrolidone molecular weights on the formation of nanosized silver colloids. *Mater. Chem. Phys.* **2004**, *83*, 82–88. DOI:10.1016/j.matchemphys.2003.09.026
90. Xiong Y, Siekkinen AR, Wang J, Yin Y, Kim MJ, Xia Y. Synthesis of silver nanoplates at high yields by slowing down the polyol reduction of silver nitrate with polyacrylamide. *J. Mater. Chem.* **2007**, *17*, 2600–2602. DOI:10.1039/b705253g
91. Falletta E, Bonini M, Fratini E, Lo Nostro A, Pesavento G, Becheri A, et al. Clusters of poly(acrylates) and silver nanoparticles: Structure and applications for antimicrobial fabrics. *J. Phys. Chem. C* **2008**, *112*, 11758–11766. DOI:10.1021/jp8035814
92. Prozorova G, Pozdnyakov A, Kuznetsova N, Korzhova S, Emel'yanov A, Ermakova T, et al. Green synthesis of water-soluble nontoxic polymeric nanocomposites containing silver nanoparticles. *Int. J. Nanomed.* **2014**, *9*, 1883–1889. DOI:10.2147/IJN.S57865
93. Guo L, Nie J, Du B, Peng Z, Tesche B, Kleinermanns K. Thermoresponsive polymer-stabilized silver nanoparticles. *J. Colloid Interface Sci.* **2008**, *319*, 175–181. DOI:10.1016/j.jcis.2007.11.022
94. Kaliammal P, Rosemary MJ, Khadar MAS. Synthesis, characterization and applications of polymer-protected silver and silver iodide nanoparticles. *Indian J. Nanotechnol. Appl.* **2013**, *1*, 49–60. Available online: https://www.academia.edu/download/35489816/jnav1n1_06.pdf (accessed on 4 March 2026).
95. Maidul Islam AKM, Mukherjee M. Effect of temperature in synthesis of silver nanoparticles in triblock copolymer micellar solution. *J. Exp. Nanosci.* **2011**, *6*, 596–611. DOI:10.1080/17458080.2010.506518
96. Abdel-Halima ES, El-Rafie MH, Al-Deyab SS. Polyacrylamide/guar gum graft copolymer for preparation of silver nanoparticles. *Carbohydr. Polym.* **2011**, *85*, 692–697. DOI:10.1016/j.carbpol.2011.03.039
97. Namazi H, Fard AMP, Pooresmaeil M. Peripherally functionalized dendrimers as templates for synthesis of silver nanoparticles and investigation of factors affecting their properties. *Polym. Bull.* **2019**, *76*, 4659–4675. DOI:10.1007/s00289-018-2629-y
98. Franckevičius M, Gustainytė A, Kondrotas R, Juškėnas R, Marcos M, Serrano JL, et al. PPI–SA and PAMAM–SA dendrimer-assisted synthesis of silver nanoparticles: Structure, optical properties and stability. *J. Nanopart. Res.* **2014**, *16*, 2343. DOI:10.1007/s11051-014-2343-0
99. Voets IK, de Keizer A, Frederik PM, Jellema R, Cohen Stuart MA. Environment-sensitive stabilisation of silver nanoparticles in aqueous solutions. *J. Colloid Interface Sci.* **2009**, *339*, 317–324. DOI:10.1016/j.jcis.2009.07.065
100. Aguilar-Méndez MA, Martín-Martínez ES, Ortega-Arroyo L, Cobián-Portillo G, Sánchez-Espíndola E. Synthesis and characterization of silver nanoparticles: Effect on phytopathogen *Colletotrichum gloeosporioides*. *J. Nanopart. Res.* **2011**, *13*, 2525–2532. DOI:10.1007/s11051-010-0145-6
101. Medina-Ramirez I, Bashir S, Luo Z, Liu JL. Green synthesis and characterization of polymer-stabilized silver nanoparticles. *Colloids Surf. B Biointerfaces* **2009**, *73*, 185–191. DOI:10.1016/j.colsurfb.2009.05.015
102. Huang H, Yuan Q, Yang X. Preparation and characterization of metal–chitosan nanocomposites. *Colloids Surf. B Biointerfaces* **2004**, *39*, 31–37. DOI:10.1016/j.colsurfb.2004.08.014
103. Bankura KP, Maity D, Mollick MMR, Mondal D, Bhowmick B, Bain MK, et al. Synthesis, characterization and antimicrobial activity of dextran-stabilized silver nanoparticles in aqueous medium. *Carbohydr. Polym.* **2012**, *89*, 1159–1165. DOI:10.1016/j.carbpol.2012.03.089
104. Liu Y, Chen S, Zhong L, Wu G. Preparation of highly stable silver nanoparticle dispersions using sodium alginate as a stabilizer under gamma radiation. *Radiat. Phys. Chem.* **2009**, *78*, 251–255. DOI:10.1016/j.radphyschem.2009.01.003
105. Zheltonozhskaya TB, Permyakova NM, Kravchenko OO, Maksin VI, Nessin SD, Klepko VV, et al. Polymer/inorganic hybrids containing silver nanoparticles and their activity in the disinfection of fish aquariums and ponds. *Polym.-Plast. Technol. Mater.* **2021**, *60*, 369–391. DOI:10.1080/25740881.2020.1811318
106. Fedorchuk SV, Zheltonozhskaya TB, Gomza YuP, Klymchuk DO, Kunitskaya LR. Morphology of silver nanoparticles in micelle-forming block copolymers. *Mol. Cryst. Liq. Cryst.* **2014**, *590*, 172–178. DOI:10.1080/15421406.2013.874213
107. Fedorchuk SV, Zheltonozhskaya TB, Gomza YP, Nessin SD, Klymchuk DO. Morphology of silver nanoparticles in graft copolymer matrices. In Proceedings of the International Conference "Nanomaterials: Applications and Properties", Crimea, Ukraine, 16–21 September 2013.
108. Zheltonozhska TB, Kravchenko OO, Maksin VI, Fedorchuk SV, Permyakova NM, Demchenko OV. Polymer-Silver Composition for Disinfection of Aquariums and Fish Ponds and the Method of Its Production. Ukrainian Patent UA 112587, 26 September 2016.
109. Nyyssola A, Ahlgren J. Microbial degradation of polyacrylamide and the deamination product polyacrylate. *Int. Biodeterior. Biodegrad.* **2019**, *139*, 24–33. DOI:10.1016/j.ibiod.2019.02.005
110. Scientific Committee on Consumer Safety. *Opinion on Solubility of Synthetic Amorphous Silica (SAS). SCCS/1606/2019*; European Commission: Brussels, Belgium, 2019.

111. Zheltonozhskaya T, Permyakova N, Momot LN, Eremenko BV. *Hydrogen-Bonded Interpolymer Complexes: Formation, Structure and Applications*; Khutoryanskiy VV, Staikos G, Eds.; World Scientific: Hackensack, NJ, USA, 2009; Chapter 5, pp. 85–153; Chapter 8, pp. 201–234.
112. Demchenko OV, Filipchenko SO, Zheltonozhska TB, Kunitska LR, Syromyatnikov VG. Method for Clarification of Colloidal Dispersions. Ukrainian Patent UA 77364, 15 November 2006.
113. Demchenko OV, Novyk AV, Zheltonozhskaya TB, Syromyatnikov VG. Polyacrylamide-grafted silica for environmental protection. *Mol. Cryst. Liq. Cryst.* **2008**, *486*, 306–315. DOI:10.1080/15421400801921934
114. Huang CK, Chen CY, Han JL, Chen CC, Jiang MD, Hsu JS, et al. Immobilization of silver nanoparticles on silica microspheres. *J. Nanopart. Res.* **2010**, *12*, 199–207. DOI:10.1007/s11051-009-9594-1
115. Liong M, France B, Bradley KA, Zink JI. Antimicrobial activity of silver nanocrystals encapsulated in mesoporous silica nanoparticles. *Adv. Mater.* **2009**, *21*, 1684–1689. DOI:10.1002/adma.200802646
116. Sadjadi MS, Farhadyar N, Zare K. Preparation and characterization of inorganic–organic nanocomposite coatings. In *Advances in Nanocomposites: Synthesis, Characterization and Industrial Applications*; Reddy B, Ed.; InTech: Rijeka, Croatia, 2011.
117. Tsubokawa N. Environmentally friendly synthesis of polymer-grafted nanoparticles. In *Applications of Ionic Liquids in Science and Technology*; Handy S, Ed.; InTech: Rijeka, Croatia, 2011; Chapter 9, pp. 174–196.
118. Wu L, Glebe U, Böker A. Surface-initiated controlled radical polymerizations from silica nanoparticles, gold nanocrystals, and bionanoparticles. *Polym. Chem.* **2015**, *6*, 5143–5184. DOI:10.1039/C5PY00525F
119. Bourgeat-Lami E, d'Agosto F, Lansalot M. Synthesis of nanocapsules and polymer/inorganic nanoparticles through controlled radical polymerization at and near interfaces. In *Advances in Polymer Science: Controlled Radical Polymerization at and from Solid Surfaces*; Vana P, Ed.; Springer: Berlin/Heidelberg, Germany, 2016; Volume 270, pp. 123–161.
120. Li H, Chen X, Shen D, Wu F, Pleixats R, Pan J. Functionalized silica nanoparticles: Classification, synthetic approaches and recent advances in adsorption applications. *Nanoscale* **2021**, *13*, 15998–16016. DOI:10.1039/D1NR04048K
121. Liu J, Wang S, He L, Hu P, Gao Y. Preparation and properties of nano-silica hybrid hydrophobic associated polyacrylamide for polymer flooding. *J. Pet. Sci. Eng.* **2022**, *208*, 109434. DOI:10.1016/j.petrol.2021.109434
122. Nemoto H, Shimba D, Kana T. Preparation of monodisperse silica-polyacrylamide hybrid particles with snowman or core-shell morphologies using a microfluidic device. *J. Asian Ceram. Soc.* **2022**, *10*, 378–385. DOI:10.1080/21870764.2022.2055858
123. Grisolia A, Dell'Olio G, Spadafora A, De Santo M, Morelli C, Leggio A, et al. Hybrid Polymer-Silica Nanostructured Materials for Environmental Remediation. *Molecules* **2023**, *28*, 5105. DOI:10.3390/molecules28135105
124. Álvarez-Bermúdez O, Adam-Cervera I, Landfester K, Munoz-Espí R. Morphology control of polymer–inorganic hybrid nanomaterials prepared in miniemulsion: From solid particles to capsules. *Polymers* **2024**, *16*, 2997. DOI:10.3390/polym16212997
125. Massironi A. Hybrid organic polymer/inorganic nano-materials for biomedical applications: Where we are and where to go? *Curr. Nanosci.* **2024**, *20*, 188–205. DOI:10.2174/1573413719666230410113733
126. Sadjadi MS, Farhadyar N, Zare K. Preparation and characterization of the transparent SiO_2-Ag/PVP nanocomposite mirror film for the infrared region by sol-gel method. *Superlattices Microstruct.* **2009**, *46*, 483–489. DOI:10.1016/j.spmi.2009.06.004
127. Rivero PJ, Urrutia A, Goicoechea J, Zamarreño CR, Arregui FJ, Matías IR. An antibacterial coating based on a polymer/sol-gel hybrid matrix loaded with silver nanoparticles. *Nanoscale Res. Lett.* **2011**, *6*, 305. DOI:10.1186/1556-276X-6-305
128. Angelova T, Rangelova N, Yuryev R, Georgieva N, Müller R. Antibacterial activity of SiO_2/hydroxypropyl cellulose hybrid materials containing silver nanoparticles. *Mater. Sci. Eng. C* **2012**, *32*, 1241–1246. DOI:10.1016/j.msec.2012.03.015
129. Motornov M, Roiter Y, Tokarev I, Minko S. Stimuli-responsive nanoparticles, nanogels and capsules for integrated multifunctional intelligent systems. *Prog. Polym. Sci.* **2010**, *35*, 174–211. DOI:10.1016/j.progpolymsci.2009.10.004
130. Moraes J, Ohno K, Maschmeyer T, Perri SS. Synthesis of silica–polymer core–shell nanoparticles by reversible addition–fragmentation chain transfer polymerization. *Chem. Commun.* **2013**, *49*, 9077. DOI:10.1039/c3cc45319g
131. Jadhav SA, Garud HB, Patil AH, Patil GD, Patil CR, Dongale TD, et al. Recent advancements in silica nanoparticles based technologies for removal of dyes from water. *Colloid Interface Sci. Commun.* **2019**, *30*, 100181. DOI:10.1016/j.colcom.2019.100181
132. Zheltonozhskaya TB, Zagdanskaya NE, Demchenko OV, Momot LN, Permyakova NM, Syromyatnikov VG, et al. Graft copolymers with chemically complementary components as a special class of high-molecular-weight compounds. *Russ. Chem. Rev.* **2004**, *73*, 811–829. DOI:10.1070/RC2004v073n08ABEH000901

133. Zheltonozhskaya TB, Fedorchuk SV, Syromyatnikov VG. Processes for obtaining linear block copolymers. *Russ. Chem. Rev.* **2007**, *76*, 731–765. DOI:10.1070/RC2007v076n08ABEH003696
134. Demchenko O, Zheltonozhskaya T, Filipchenko S. Polyacrylamide-grafted silica as special type of polymer-colloid complex. *Macromol. Symp.* **2005**, *222*, 103–108. DOI:10.1002/masy.200550411
135. Tsubokawa N, Maruyama K, Sone Y, Shimomura M. Graft polymerization of acrylamide from ultrafine silica particles by use of a redox system consisting of ceric ion and reducing groups on the surface. *Polym. J.* **1989**, *21*, 475–481. DOI:10.1295/polymj.21.475
136. Filipchenko S, Demchenko O, Zheltonozhskaya T, Syromyatnikov V. Kinetics of polyacrylamide grafting onto ultra-fine silica particles surface. In *Polymers of Special Application*; Radom Univ. of Technol.: Radom, Poland, 2007; pp. 87–90.
137. Tan YY. The synthesis of polymers by template polymerization. *Prog. Polym. Sci.* **1994**, *19*, 561–588. DOI:10.1016/0079-6700(94)90028-0
138. Taga T, Ohara N, Iuagaki H. Graft Copolymerization of Vinyl Monomers onto Cellulose with Ceric Ion: The Reducing Endgroup of Cellulose as the Grafting Site. *Sen'i Gakkaishi* **1979**, *35*, T512–T519. DOI:10.2115/fiber.35.12_T512
139. Takanashi T, Nagata M, Hori Y, Sato I. New information on the ceric salt-initiated polymerization of acrylamide. *J. Polym. Sci. B Polym. Lett.* **1967**, *5*, 509–513. DOI:10.1002/pol.1967.110050615
140. Behari K, Pandey PK, Kumar R, Taunk K. Graft copolymerization of acrylamide onto xanthan gum. *Carbohydr. Polym.* **2001**, *46*, 185–189. DOI:10.1016/S0144-8617(00)00291-5
141. Kumar A, Kumar DR, Keshari AK, Srivastava R. The graft copolymerization of N-(hydroxymethyl) acrylamide onto xanthan gum and its anti-oxidative property. *Polym. Sci. Ser. B* **2019**, *61*, 817–826. DOI:10.1134/S1560090419070017
142. Cheng L, Yang G, Zhang S, Zhang Y, Gao C, Song N, et al. Preparation and action mechanism of temperature sensitive N-isopropylacrylamide/nanosilica hybrid as rheological modifier for water-based drilling fluid. *J. Pet. Sci. Eng.* **2022**, *219*, 111096. DOI:10.1016/j.petrol.2022.111096
143. Huang SY, Lipp DW, Farinato RS. Acrylamide Polymers. In *Encyclopedia of Polymer Science and Technology*; John Wiley & Sons: New York, NY, USA, 2001; Volume 1, pp. 304–342.
144. Permyakova N, Zheltonozhskaya T, Demchenko O, Momot L, Filipchenko S, Zagdanskava N, et al. Interactions, stabilizing the structure of intermolecular polycomplex between poly(vinyl alcohol) and polyacrylamide. *Polish J. Chem.* **2002**, *76*, 1347–1361. Available online: https://yadda.icm.edu.pl/baztech/element/bwmeta1.element.baztech-article-BUJ1-0023-0047 (accessed on 10 February 2026).
145. Pretsch E, Bühlmann P, Affolter C, Pretsch E, Bhuhlmann P, Affolter C. *Structure Determination of Organic Compounds*; *Tables of Spectral Data*; Springer: Berlin/Heidelberg, Germany, 2000.
146. Fedorchuk S, Zheltonozhskaya T, Gomza Y, Kunitskaya L, Demchenko O. Synthesis of silver nanoparticles in the matrices of block and graft copolymers and inorganic polymer substance in water solutions. *Macromol. Symp.* 2012, *317–318*, 103–116. DOI:10.1002/masy.201100098
147. Fedorchuk SV, Zheltonozhskaya TB, Shembel EM, Kunitskaya LR, Maksuta IM, Gomza YP. Structure and ionic conductivity of the PEO-containing triblock copolymers forming intramolecular polycomplexes. *Funct. Mater.* **2011**, *18*, 429. Available online: https://nasplib.isofts.kiev.ua/server/api/core/bitstreams/f9314568-49c0-4dd5-afbb-e9d28323350f/content (accessed on 10 February 2026).
148. Beaucage G, Hyeonlee J, Pratsinis SE, Vemury S. Fractal Analysis of Flame-Synthesized Nanostructured Silica and Titania Powders Using Small-Angle X-ray Scattering. *Langmuir* **1998**, *14*, 5751–5756. DOI:10.1021/la980308s
149. Zheltonozhskaya TB, Permyakova NM, Kondratiuk TO, Beregova TV, Klepko VV, Melnik BS. Hybrid-stabilized silver nanoparticles and their biological impact on hospital infections, healing wounds, and wheat cultivation. *French-Ukrainian J. Chem.* **2019**, *7*, 20–39. DOI:10.17721/fujcV7I2P20-39
150. Zheltonozhskaya TB, Permyakova NM, Klepko VV, Grishchenko LM, Klymchuk DO. Highly dispersed nanocomposites based on polymer-inorganic hybrids and nickel nanoparticles: The role of matrix structure in the *in situ* formation process. *Polymernyi Zhurn.* **2023**, *45*, 37–55. DOI:10.15407/polymerj.45.01.037
151. Mahapatra AP, Samal RK, Samal RN, Roy GS. Evaluation of Huggins' constant, Kraemer's constant and viscosity concentration coefficient of polymer dextran in urea, glycine and glucose. *Phys. Chem. Liquids* **2001**, *39*, 169–181. DOI:10.1080/00319100108030337
152. Zheltonozhskaya T, Akopova O, Dąbrowska I, Permyakova N, Klepko V, Klymchuk D. Hybrid nanocarriers with different densities of silver nanoparticles formation features and antimicrobial properties. *Sci. Rep.* **2025**, *15*, 6757. DOI:10.1038/s41598-025-89021-0
153. Romanov V, Siu CK, Verkerk UH, Aribi HE, Hopkinson AC, Siu KWM. Binding energies of the silver ion to alcohols and amides: A theoretical and experimental study. *J. Phys. Chem. A* **2008**, *112*, 10912–10920. DOI:10.1021/jp8055653

154. Sobczak-Kupiec A, Malina D, Wzorek Z, Zimowska M. Influence of silver nitrate concentration on the properties of silver nanoparticles. *Micro Nano Lett.* **2011**, *6*, 656–660. DOI:10.1049/mnl.2011.0152
155. Santos D, Sequeira C. Sodium borohydride as a fuel for the future. *Renew. Sustain. Energy Rev.* **2011**, *15*, 3980–4001. DOI:10.1016/j.rser.2011.07.018
156. Mohapatra S, Nguyen TA, Nguyen-Tri P. (Eds.). *Noble Metal-Metal Oxide Hybrid Nanoparticles: Fundamentals and Applications*; Elsevier, Woodhead Publishing: Oxford, UK, 2018.
157. Link S, El-Sayed MA. Spectral properties and relaxation dynamics of surface plasmon electronic oscillations in gold and silver nanodots and nanorods. *J. Phys. Chem. B* **1999**, *103*, 8410–8426. DOI:10.1021/jp9917648
158. Kelly KL, Coronado E, Zhao LL, Schatz GC. The optical properties of metal nanoparticles: The influence of size, shape, and dielectric environment. *J. Phys. Chem. B* **2003**, *107*, 668–677. DOI:10.1021/jp026731y
159. Evanoff DD, Jr., Chumanov G. Synthesis and optical properties of silver nanoparticles and arrays. *Chem. Phys. Chem.* **2005**, *6*, 1221–1231. DOI:10.1002/cphc.200500113
160. Liz-Marzan LM. Tailoring surface plasmons through the morphology and assembly of metal nanoparticles. *Langmuir* **2006**, *22*, 32–41. DOI:10.1021/la0513353
161. Zheltonozhskaya TB, Shevchenko LV, Permyakova NM, Dovbnia YY, Klepko VV, Klymchuk DO. Promising nanobiotechnology for poultry farming based on silver nanoparticles embedded in polymer-inorganic hybrid carriers. *Polymernyi Zhurn.* **2023**, *45*, 153–174. DOI:10.15407/polymerj.45.02.153
162. Amirjani A, Firouzi F, Haghshenas DF. Predicting the size of silver nanoparticles from their optical properties. *Plasmonics* **2020**, *15*, 1077–1082. DOI:10.1007/s11468-020-01121-x
163. Debnath D, Kim C, Kim SH, Geckeler KE. Solid-state synthesis of silver nanoparticles at room temperature: Poly(vinylpirrolidone) as a tool. *Macromol. Rapid Commun.* **2010**, *31*, 549–553. DOI:10.1002/marc.200900656
164. Li L, Zhu YJ. High chemical reactivity of silver nanoparticles toward hydrochloric acid. *J. Colloid Interface Sci.* **2006**, *303*, 415–418. DOI:10.1016/j.jcis.2006.07.059
165. Montes-Hernandez G, Di Girolamo M, Sarret G, Bureau S, Fernandez-Martinez A, Lelong C, et al. *In situ* formation of silver nanoparticles (Ag-NPs) onto textile fibers. *ACS Omega* **2021**, *6*, 1316–1327. DOI:10.1021/acsomega.0c04814
166. Chen H, Zhang G, Zhang W, Gao W. Silver nanoparticles deposited on a cotton fabric surface via an *in situ* method using reactive hyperbranched polymers and their antibacterial properties. *RSC Adv.* **2023**, *13*, 11450–11456. DOI:10.1039/D3RA00989K
167. Hemamalini T, Gokul PGK, Mahalakshmi RS, Rajesh R, Dev VRG. Silver nanoparticle-incorporated textile substrate for antimicrobial applications. In *Interaction of Nanomaterials with Living Cells*; Sheikh FA, Majeed S, Beigh MA, Eds.; Springer: Singapore, 2023; pp. 799–819.
168. Abazari M, Badeleh SM, Khaleghi F, Saeedi M, Haghi F. Fabrication of silver nanoparticles-deposited fabrics as a potential candidate for the development of reusable facemasks and evaluation of their performance. *Sci. Rep.* **2023**, *13*, 1593. DOI:10.1038/s41598-023-28858-9
169. Dumas L, de Souza MC, Bonafe EG, Martins AF, Monteiro JP. Optimized incorporation of silver nanoparticles onto cotton fabric using k-carrageenan coatings for enhanced antimicrobial properties. *ACS Appl. Bio Mater.* **2024**, *7*, 6908–6918. DOI:10.1021/acsabm.4c01002
170. Huang Y, Li X, Liao Z, Zhang G, Liu Q, Tang J, et al. A randomized comparative trial between Acticoat and SD-Ag in the treatment of residual burn wounds, including safety analysis. *Burns* **2007**, *33*, 161–166. DOI:10.1016/j.burns.2006.06.020
171. Chen J, Han CM, Lin XW, Tang ZJ, Su SJ. Effect of silver nanoparticle dressing on second degree burn wound. *Zhonghua Wai Ke Za Zhi* **2006**, *44*, 50–52. (In Chinese). Available online: https://europepmc.org/article/med/16620649 (accessed on 26 January 2026).
172. Gunasekaran T, Nigusse T, Dhanaraju MD. Silver nanoparticles as real topical bullets for wound healing. *J. Am. Coll. Clin. Wound Spec.* **2012**, *3*, 82–96. DOI:10.1016/j.jcws.2012.05.001
173. Nandhini J, Karthikeyan E, Elizabeth Rani E, Karthikha VS, Sakthi Sanjana D, Jeevitha H, et al. Advancing engineered approaches for sustainable wound regeneration and repair: Harnessing the potential of green synthesized silver nanoparticles. *Eng. Regen.* **2024**, *5*, 306–325. DOI:10.1016/j.engreg.2024.06.004
174. Kalantari K, Mostafavi E, Afifi AM, Izadiyan Z, Jahangirian H, Rafiee-Moghaddam R, et al. Wound dressings functionalized with silver nanoparticles: Promises and pitfalls. *Nanoscale* **2020**, *12*, 2268–2291. DOI:10.1039/C9NR08234D
175. Rybka M, Mazurek Ł, Konop M. Beneficial effect of wound dressings containing silver and silver nanoparticles in wound healing—From experimental studies to clinical practice. *Life* **2023**, *13*, 69. DOI:10.3390/life13010069
176. Paladini F, Pollini M. Antimicrobial silver nanoparticles for wound healing: Progress and future trends. *Materials* **2019**, *12*, 2540. DOI:10.3390/ma12162540

177. Han G, Ceilley R. Chronic wound healing: A review of current management and treatments. *Adv. Ther.* **2017**, *34*, 599–610. DOI:10.1007/s12325-017-0478-y
178. D'Amora U, Scialla S, Fasolino I, Ronca A, Soriente A, De Cesare N, et al. Eumelanin pigment release from photo-crosslinkable methacrylated gelatin-based cryogels: Exploring the physicochemical properties and antioxidant efficacy in wound healing. *Biomater. Adv.* **2025**, *170*, 214214. DOI:10.1016/j.bioadv.2025.214214
179. Demchenko OV, Zheltonozhskaya TB, Syromyatnikov VG, Strelchuk NV, Yashchuk VN, Kudrya VY. Polymer sensors with optical response based on thermal modified intramolecular polycomplexes PVA-PAAN. *Funct. Mater.* **2000**, *7*, 711–716. Available online: https://functmaterials.org.ua/contents/7-4-1/31.pdf (accessed on 16 February 2026).
180. Praveen PK, Debnath C, Shekhar S, Dalai N, Ganguly S. Incidence of *Aeromonas* spp. infection in fish and chicken meat and its related public health hazards: A review. *Vet. World* **2016**, *9*, 6–11. DOI:10.14202/vetworld.2016.6-11
181. Lopez JR, Lorenzo L, Marcelino-Pozuelo C, Marin-Arjona MC, Navas JIP. Pseudomonas baetica: Pathogenicity for marine fish and development of protocols for rapid diagnosis. *FEMS Microbiol. Lett.* 2017, *364*, fnw286. DOI:10.1093/femsle/fnw286
182. Wamala SP, Mugimba KK, Mutoloki S, Evensen Ø, Mdegela R, Byarugaba DK, et al. Occurrence and antibiotic susceptibility of fish bacteria isolated from *Oreochromis niloticus* (*Nile tilapia*) and *Clarias gariepinus* (*African catfish*) in Uganda. *Fish Aquat. Sci.* **2018**, *21*, 6. DOI:10.1186/s41240-017-0080-x
183. Shaalan MI, El-Mahdy MM, Theiner S, El-Matbouli M, Saleh M. *In vitro* assessment of the antimicrobial activity of silver and zinc oxide nanoparticles against fish pathogens. *Acta Vet. Scand.* **2017**, *59*, 49. DOI:10.1186/s13028-017-0317-9
184. Shaffiey SF, Shapoori M, Bozorgnia A, Ahmadi M. Synthesis and evaluation of bactericidal properties of CuO nanoparticles against *Aeromonas hydrophila*. *Nanomed. J.* **2014**, *1*, 198–204. Available online: https://www.sid.ir/en/VEWSSID/J_pdf/50001320140310.pdf (accessed on 14 March 2026).
185. Belanger SE, Rawlings JM, Carr GJ. Use of fish embryo toxicity tests for the prediction of acute fish toxicity to chemicals. *Environ. Toxicol. Chem.* **2013**, *32*, 1768–1783. DOI:10.1002/etc.2244
186. Braunbeck T, Kais B, Lammer E, Otte J, Schneider K, Stengel D, et al. The fish embryo test (FET): Origin, applications, and future. *Environ. Sci. Pollut. Res.* **2015**, *22*, 16247–16261. DOI:10.1007/s11356-014-3814-7
187. Kovalenko VF, Zlatskii IA, Goncharuk VV. Adaptive capabilities of hydrobionts to aqueous medium with different physicochemical parameters. *J. Water Chem. Technol.* **2016**, *38*, 56–61. DOI:10.3103/S1063455X16010100
188. Hussain B, Sultana T, Sultana S, Masoud MS, Ahmed Z, Mahboob S. Fish eco-genotoxicology: Comet and micronucleus assay in fish erythrocytes as *in situ* biomarker of freshwater pollution. *Saudi J. Biol. Sci.* **2018**, *25*, 393–398. DOI:10.1016/j.sjbs.2017.11.048
189. Pereira AC, Gomes T, Machado MRF, Rocha TL. The zebrafish embryotoxicity test (ZET) for nanotoxicity assessment: From morphological to molecular approach. *Environ. Pollut.* **2019**, *252*, 1841–1853. DOI:10.1016/j.envpol.2019.06.100
190. *ISO 6341:2012 (R2018)*; Water Quality—Determination of the Inhibition of the Mobility of *Daphnia magna* Straus (Cladocera, Crustacea). Acute Toxicity Test, 4th ed.; ISO: Geneva, Switzerland, 2012.
191. Pociecha E, Gorczyca A, Dziurka M, Matras E, Oćwieja M. Silver nanoparticles and silver ions differentially affect the phytohormone balance and yield in wheat. *Agriculture* **2021**, *11*, 729. DOI:10.3390/agriculture11080729
192. Feng L, Xu N, Qu Q, Zhang Z, Ke M, Lu T, et al. Synergetic toxicity of silver nanoparticle and glyphosate on wheat (*Triticum aestivum* L.). *Sci. Total Environ.* **2021**, *797*, 149200. DOI:10.1016/j.scitotenv.2021.149200
193. Lahuta LB, Szablińska-Piernik J, Głowacka K, Stałanowska K, Railean-Plugaru V, Horbowicz M, et al. The effect of bio-synthesized silver nanoparticles on germination, early seedling development, and metabolome of wheat (*Triticum aestivum* L.). *Molecules* **2022**, *27*, 2303. DOI:10.3390/molecules27072303
194. Khan S, Zahoor M, Khan RS, Ikram M, Islam NU. The impact of silver nanoparticles on the growth of plants: The agriculture applications. *Heliyon* **2023**, *9*, e16928. DOI:10.1016/j.heliyon.2023.e16928
195. Przemieniecki SO, Ruraż K, Kosewska O, Oćwieja M, Gorczyca A. The impact of various forms of silver nanoparticles on the rhizosphere of wheat (*Triticum aestivum* L.)—Shifts in microbiome structure and predicted microbial metabolic functions. *Sci. Total Environ.* **2024**, *914*, 169824. DOI:10.1016/j.scitotenv.2023.169824
196. Danish S, Hussain GS, Shah SH, Mehmood H, Fahad S, Alharbi SA, et al. Green synthesized silver nanoparticles alleviate lead toxicity in maize and wheat. *Pak. J. Bot.* **2024**, *56*, 2179–2187. DOI:10.30848/PJB2024-6(34)
197. Mishra AK, Singh D, Deepak S, Reddy S. Modulation of biochemical properties in wheat by silver nanoparticles under salt stress conditions. *NESciences* **2025**, *10*, 244–254. DOI:10.28978/nesciences.1643520
198. Minic D, Markovic K, Kesic A, Grujovic M, Markovic S, Torbica A, et al. The effects of silver nanoparticles synthesized with an aqueous extract of *Agrimonia eupatoria* L. on winter wheat and barley varieties. *J. Serb. Chem. Soc.* **2025**, *90*, 175–186. DOI:10.2298/JSC241105096M

199. Salama YA, Alghoraibi I, Zein R, Alsouse M. Silver nanoparticles seed priming for sustainable enhancement of durum wheat growth, yield, and nutrient enrichment. *IET Nanobiotechnol.* **2025**, *2025*, 7. DOI:10.1049/nbt2/6152486
200. Alfosea-Simón FJ, Burgos L, Alburquerque N. Silver nanoparticles help plants grow, alleviate stresses, and fight against pathogens. *Plants* **2025**, *14*, 428. DOI:10.3390/plants14030428
201. Ding S, Zheng L, Tao T, Li Q, Cai J, Zhou Q, et al. Silver nanoparticles priming for drought tolerance in wheat: Insights from antioxidant system activation and stress memory. *Chem. Biol. Technol. Agric.* **2025**, *12*, 57. DOI:10.1186/s40538-025-00778-y
202. Shevchenko LV, Dovbnia YY, Zheltonozhskaya TB, Permyakova NM, Vygovska LM, Ushkalov VO. Influence of nanosilver preparation in carriers based on polymer/inorganic hybrids on the quality and safety of chicken eggs. *Regul. Mech. Biosyst.* **2021**, *12*, 391–395. DOI:10.15421/022153
203. Shevchenko LV, Dovbnia YY, Permyakova NM, Zheltonozhskaya TB, Shulyak SV, Klymchuk DO. Influence of nanosilver stabilized in polymer/inorganic hybrids on morphological and biochemical parameters of the blood of laying hens. *Regul. Mech. Biosyst.* **2022**, *13*, 15–22. DOI:10.15421/022203
204. Bergin IL, Wilding LA, Morishita M, Walacavage K, Ault AP, Axson JL, et al. Effects of particle size and coating on toxicologic parameters, fecal elimination kinetics and tissue distribution of acutely ingested silver nanoparticles in a mouse model. *Nanotoxicology* **2016**, *10*, 352–360. DOI:10.3109/17435390.2015.1072588
205. Nabinejad AR, Noaman V, Khayyam Nekouiee M. Evaluation of silver residues accumulation in tissues of Broilers treated with nanosilver using MNSR (A Clinical Trial). *Arch. Razi Inst.* **2016**, *71*, 51–55. DOI:10.22034/ari.2016.105998
206. World Health Organization. *Guidelines for Drinking-Water Quality [Electronic Resource]: Incorporating 1st and 2nd Addenda, Volume 1, Recommendations*; 3rd ed.; World Health Organization: Geneva, Switzerland, 2008; p. 668.
207. Ghișe A. The pH of the digesta in the gastrointestinal tract, in laying hens. *Bull. UASVM Vet. Med.* **2009**, *66*, 491–492. Available online: https://www.cabidigitallibrary.org/doi/full/10.5555/20093355258 (accessed on 10 February 2026).
208. Ghișe A, Olariu L, Trif A, Zehan R, Cărpinisan L. The determination of the mean retention time (MRT) of the dry matter in the segments of the gastrointestinal tract in laying hens. *Bull. UASVM Vet. Med.* **2009**, *66*, 378–383. Available online: https://www.academia.edu/download/107651971/267070894.pdf (accessed on 15 March 2026).
209. Farrokhi S, Ahari H, Abedini MR. Comparative effects of colloidal silver nanoparticles used in packaging film and spray in inactivating bacteria experimentally added to chicken eggshells. *Int. J. Food Prop.* **2017**, *20*, 2314–2322. DOI:10.1080/10942912.2016.1236274
210. Batkowska J, Al-Shammari KIA, Gryzinska MM, Brodacki A, Wlazlo L, Nowakowicz-Debek B. Effect of using colloidal silver in the disinfection of hatching eggs on some microbial, hatchability and performance traits in Japanese quail (*Coturnix cot. japonica*). *Eur. Poult. Sci.* **2017**, *81*, 211. DOI:10.1399/eps.2017.211
211. Chmielowiec-Korzeniowska A, Tymczyna L, Dobrowolska M, Banach M, Nowakowicz-Dębek B, Bryl M, et al. Silver (Ag) in tissues and eggshells, biochemical parameters and oxidative stress in chickens. *Open Chem.* **2015**, *13*, 1269–1274. DOI:10.1515/chem-2015-0140
212. Akopova OV, Zheltonozhskaya T, Zahorodnia S, Klymchuk D, Korkach Y, Zavgorodniy M, et al. The anticancer properties of the nanocomposite of low-nanoscale Ag nanoparticles obtained in SiO_2-grafted polyacrylamide carrier. *BMC Pharmacol. Toxicol.* **2026**, *27*, 69. DOI:10.1186/s40360-026-01115-1